Swansea University
Prifysgol Abertawe

Hard Carbon and Sodium Rhodizonate Electrodes for Sodium-ion Batteries

Lorn Alexander M

Jackson

Submitted to Swansea University in fulfilment of the requirements for the Degree of Master of Philosphy

July 2023

DECLARATION

This work has not previously been accepted in substance for any degree and is not being concurrently submitted in candidature for any degree.

Signed: .....

Date: 7/7/23

STATEMENT 1

This thesis is the result of my own investigations, except where otherwise stated. Where correction services have been used, the extent and nature of the correction is clearly marked in a footnote(s). Other sources are acknowledged by footnotes giving explicit references. A bibliography is appended.

Signed: .....

Date: 7/7/23

STATEMENT 2

I hereby give consent for my thesis, if accepted, to be available for photocopying and for inter-library loan after expiry of a bar on access approved by the Swansea University, and for the title and summary to be made available to outside organizations.

Signed: .....

Date: 7/7/23

Abstract

Continued energy and climate concerns are increasing the need to develop new energy storage systems for the integration of intermittent renewable energy sources into the grid infrastructure. Sodium-ion batteries have gained significant interest recently as a viable potential solution. These offer an alternate solution to lithium-ion batteries that are at the forefront of consideration; sodium-ion batteries can potentially be cheaper, safer, and most importantly more sustainable than their lithium-ion counterparts.

The work described in this thesis focuses on the development and synthesis of electrodes for use in sodium-ion batteries. Both an anode and cathode were researched, synthesised, and then electrochemically analysed.

Acknowledgements

Over the years spent on this PhD many experiences were observed, both for better and for worse. Continued and unexpected events and situations were commonplace, but all-in-all the best outcomes were ultimately achieved.

Thus, foremost I would like to offer my thanks and support to both my supervisors, Professor Davide Deganello and Professor Serena Margadonna. Both of whom supported me from the first day, until the very last. The incredible support, patience, guidance, and motivation offered by them daily was imperative to my success.

The support from other key staff members including Nicola Henson and Sian Bengeyfield. Also, Chris Ravenhill from the University Students' Union; all three of which kept me planted and level-headed throughout.

If it were not for the support Dr Chris Phillips from the start, I would not have learnt and been able to significantly develop the skills required in the lab to undertake any of the research. When the research was not co-operating, Dr Phillips gave great advice and guidance to continue.

Research does not just involve gathering results and data, the processing is fundamental too. I would like to give thanks to my uncle, Dr John Lewis. Errors in the exported text files were commonplace, the PowerShell script was incredible!

My final acknowledgement goes to my family, my father and sister. Their support and belief in my abilities kept me motivated non-stop throughout.

To everyone I have not mentioned, I offer my utmost appreciation!

Contents

List of figures

List of Tables

List of Abbreviations page

CB	Carbon black
CMC	Carboxymethyl cellulose
CV	Cyclic voltammetry
DEGDME	Diethylene glycol dimethyl ether, or diglyme
EC	Ethylene carbonate
G2	Diethylene glycol dimethyl ether, or diglyme
G4	Tetraethylene glycol dimethyl ether, or tetraglyme
GC	Galvanostatic cycling
GO	Graphene oxide
HC	Hard carbon
NMP	N-Methyl-2-pyrrolidone
THF	Tetrahydrofuran
PVDF	Polyvinylidene fluoride
PTFE	Polytetrafluoroethylene
PC	Propylene carbonate
RGO	Reduced Graphene Oxide
TEDGME	Tetraethylene glycol dimethyl ether
NaPF6	Sodium hexafluorophosphate
NaClO4	Sodium perchlorate
H2O	Water
HCGO	Hard carbon graphene oxide
SEM	Scanning Electron Microscope

Part 1

Thesis Introduction and Current Literature Review

Introduction

Sodium-ion batteries are a type of rechargeable battery which have gained significant interest recently for large-scale storage systems . Sodium is one of the alkali metals in group 1 of the periodic table; these metals are highly reactive. Each metal within the group can lose their single outer valence electron, creating ionic bonds with other elements. All the group 1 metals are analogous to one another, thus the working mechanism for all are the same. (ABRAHAM, 1982)

Presently, the most successful group 1 rechargeable battery element is lithium, forming lithium-ion batteries which has become a crucial component for nearly all portable electronic devices. (Yabuuchi et al., 2014a) There has been continued research in refining the performance of lithium-ion batteries since the late 90s, each key component has been scrutinised thoroughly including the anodes (Blomgren, 2017) cathodes (Fergus, 2010; Karthikprabhu et al., 2018) and electrolytes (Karuppasamy et al., 2016; Karuppasamy, Kim, et al., 2017; Karuppasamy, Reddy, et al., 2017) within. Commercialisation of lithium-ion batteries by Sony happened in the 90s as a viable alternative to the then widely used, Ni-MH rechargeable battery. A key advantage being the increased energy density of lithium-ion compared to that of the Ni-MH batteries. Initially, this was 110 Wh kg-1 to 60-70 Wh kg-1 for lithium-ion and Ni-MH respectively. (Grey & Tarascon, 2017) Preliminarily, a key shortcoming of lithium-ion batteries was the cost; however, within the last decade the cost has significantly dropped by ~80% (now less than $200 kWh-1). This decrease in cost, has also seen significant performance increases with the energy density increasing to over 200 Wh kg-1. (Sutherland, 2019) Other benefits of lithium-ion batteries are long cycle life, an absence of any memory effects and low self-discharging; hence the vast interest for the use of lithium-ion within the EV and portable electronic industries. Although there are notable disadvantages. Safety being a crucial area, as lithium-ion batteries are notoriously flammable through the electrolytes used. This issue however has led to research into potential alternatives including aqueous and solid-state lithium-ion batteries. (H. Kim et al., 2014; J. G. Kim et al., 2015)Another widely predicted shortcoming is the availability of lithium itself; the use of lithium-ion is continuously increasing with increased demand. Supply chains could be crippled with the finite amount of lithium. (Grey & Tarascon, 2017) The total lithium reserve has been estimated to be ~14 million tons, with over 0.085 million tons already have been

extracted up to 2018. (Gil-Alana & Monge, 2019)This has then naturally led to other viable alternatives being put forwards as potential partial replacements to allow more effective uses of lithium-ion. For example, when space is less of a concern and the energy density requirements are less demanding, alternatives can be utilised including sodium-ion.

Both sodium and lithium-ion have vast similarities even as far as the atomic level. Thus, the advancements in lithium-ion research can potentially be exploited and transitioned into sodium-ion applications.

Sodium-ion batteries have many significant benefits over lithium-ion, one of the most significant is the abundance. Sodium itself elementally is the fourth most abundant on earth; extensively located throughout the planet. (De La Llave et al., 2016) Trona, from which the required sodium carbonate is produced from is significantly cheaper than the similarly required lithium carbonate; up to $165 per ton compared to $5000 per ton respectfully in 2010.

1.1 Aims and Objectives

The scope of this research to the develop an energy storage system that has a key advantage in terms of adopting only low-cost, widely available raw materials without any use of expensive rare metals. The specific aims of this research are:

1. To explore the development of a low-cost sodium-ion anode material
    - A simple carbohydrate raw material will be chosen using pyrolysis to produce hard carbon
    - Graphene oxide will be tested as an additive to control pyrolysis side effects
    - Controlled ramp rates will be developed to potentially remove the need for graphene oxide

2. The synthesis of sodium rhodizonate as a sodium-ion cathodic material
    - Exploration of the sodium rhodizonate particle size
    - Development of a reverse anti-solvent recrystallisation reaction
    - The inclusion of Reduced Graphene Oxide within the synthesis

3. Full-cell energy storage system
    - Development of a hard carbon/sodium rhodizonate full-cell
    - Electrochemical testing of the full-cell

1.2 Sodium-ion battery concept

The process in which lithium-ion and sodium-ion batteries work is nearly identical; the storage mechanism and battery components are essentially the same. The fundamental differences are around the ion carrier that allows the lithium and sodium ions from moving within the battery itself. These alterations are focused around the physical size difference between lithium and sodium ions; lithium ions are smaller (0.76 Å) than sodium ions (1.02 Å). Adaptations of the components used within lithium-ion batteries must be altered to be suitable to be used in sodium-ion batteries to accommodate the physical size differences. (Adelhelm et al., 2015) Furthermore, lithium is lighter than sodium (6.9 g mol^{-1} and 23 g mol^{-1} respectively). Another key difference is the standard electrode potential difference between the two, lithium has a lower standard electrode potential than sodium (-3.02V vs. SHE and -2.71 vs. SHE for lithium and sodium respectively). Thus, lithium will always have the upper hand against sodium with regards to energy densities. It is worth noting though, that these differences between the two are negligible overall weight wise when compared to the other components required. The host structures which allow the lithium/sodium ions to be stored take up most of the mass, as well as being directly responsible for the capacities for the batteries. So, the drawbacks previously mentioned with regards to sodium ion itself overall is a minor inconvenience. (Slater et al., 2013)

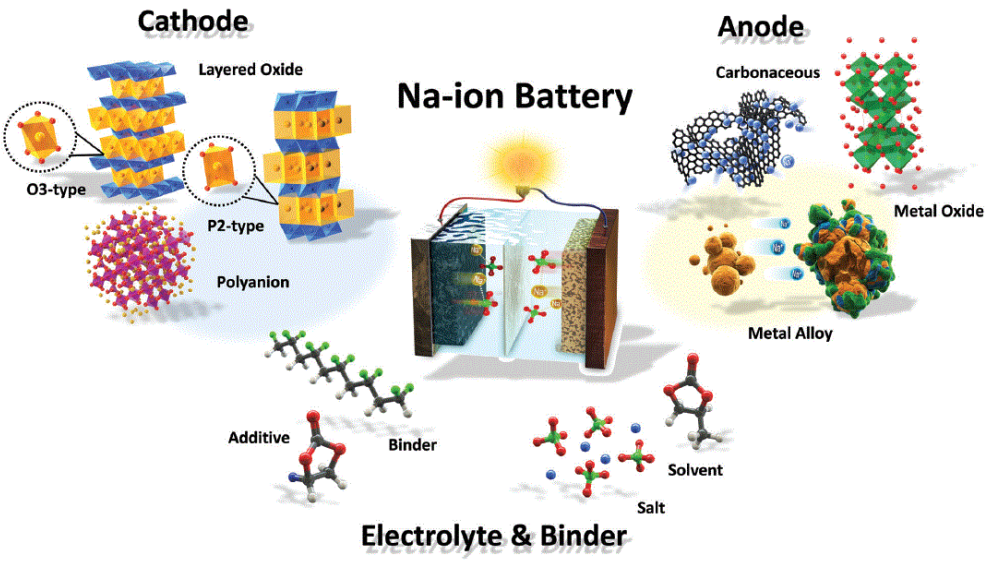

Figure 1.1: Overview of sodium-ion battery (J. Y. Hwang et al., 2017)

Figure 1.1 above shows an overview of a sodium-ion battery, as seen there are multiple components that are used within a sodium-ion battery. There are three significant components that make up a sodium-ion battery. Two of these are the electrodes with the other being the electrolyte.

1.3 Electrodes

There are two electrodes, these are the cathode and the anode. They store the sodium ions within a host-matrix structure which then allow the intercalation and de-intercalation (insertion/removal) of the sodium ions depending on the state of charge. (J. Y. Hwang et al., 2017)

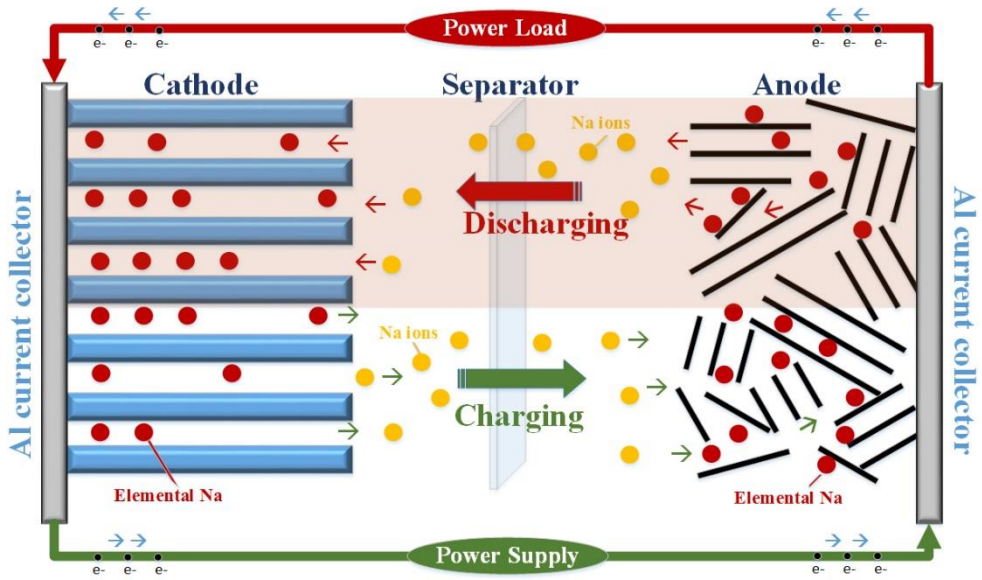

Figure 1.2: Schematic representation of sodium-ion cathodes and anodes (Tang et al., 2015)

Figure 1.2 above shows the process in which sodium-ions move within the battery. The sodium moves between the cathode and anode. (Tang et al., 2015)Numerous compounds have been seen to be effective cathodic materials, these include transition metals, metal fluorides and sulphides, polymers, Prussian blue analogues and oxyanionic compounds. (J. Y. Hwang et al., 2017) However, anodic materials have been significantly more challenging to find that offer. The most used anode for lithium-ion batteries is graphite however, sodium is unable to intercalate reliably into graphite due to the physical size of sodium. (Alcántara et al., 2001) Other carbon-based materials have however been shown to be viable anode candidates. These include carbon black and specific types of carbon fibres. (Stevens & Dahn, 2000) Hard carbons are another type of carbonaceous materials that have been put forward as potential anode pre-cursors which potentially have a great future with sodium-ion batteries, these of which will be explored in a later chapter. (Palomares et al., 2012; Xia & Dahn, 2012)

1.4 Electrolytes

There are two main type of electrolytes that are used in sodium-ion batteries, either liquid or solid-based. The liquid electrolytes that can be used are organic electrolytes, (Ji et al., 2014; J. Wang et al., 2018; Z.-L. Xu et al., 2019) aqueous electrolytes (W. Li et al., 2017; Markevich et al., 2017) and ionic liquids (ILs). (Chagas et al., 2019)There are two solid electrolyte types, these are solid polymer electrolytes and solid inorganic electrolytes. (C. Zhao et al., 2018)Out of the five groups listed above, organic electrolytes are the most frequently used. They offer very high ionic conductivity and excellent wettability with regards to the chosen porous separator in between the electrodes. (Lin et al., 2019) Electrolytes are fundamental in sodium-ion batteries as they act as the ionic charge carrier, which is required for electrochemical reactions. Organic electrolytes are comprised of a solute dissolved into a solvent/mixture of solvents. Commonly, sodium salts are dissolved into ester or ether-based solvents.

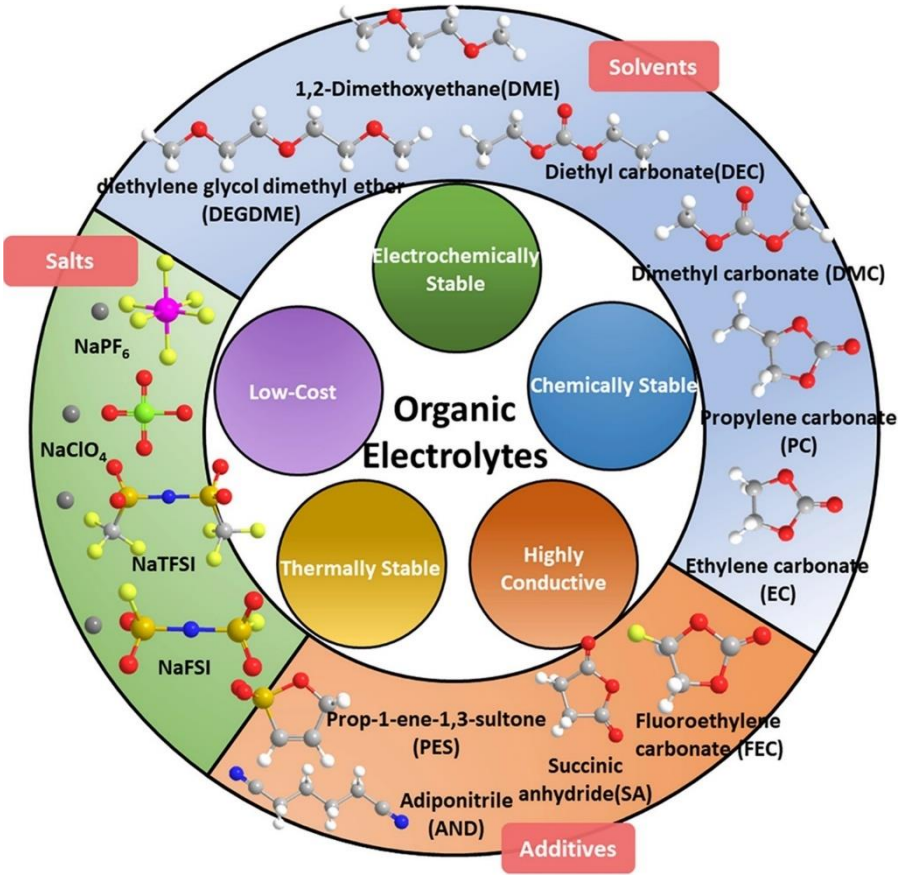

Figure 1.3: Components of organic electrolytes for sodium-ion batteries (Lin et al., 2019)

Above, in figure 1.3 is an overview of the commonly used components required to make suitable organic electrolytes for sodium-ion batteries. Ideally when choosing organic electrolytes, it is crucial to ensure that there is a high ionic conductivity, that the solvent is readily able to dissolve the salt which minimises the resistance of sodium ion movement. Also, that the electrolyte can remain stable throughout the chosen voltage range, electrolyte degradation can have detrimental effects including unwanted side reactions occurring thus hindering the cycling performances. Thermal stability is also necessary, organic solvents are highly flammable which can potentially lead to unwanted thermal runaway occurring. Simple preparation and low cost are also worth noting when using multiple solvents and additives. (Lin et al., 2019)

1.4.1 Electrolyte salts

Furthermore, figure 3 shows the four frequently used salts, these being Sodium hexafluorophosphate (NaPF6), Sodium perchlorate (NaClO4), Sodium bis(trifluoromethanesulfonyl)imide (NaTFSI) and sodium bis(fluorosulfonyl)imide (NaFSI). These salts are dissolved into a solvent or solvent mixture potentially with additional additives. Palacin et al. determined that potentially two of best sodium salt/solvent combinations was either sodium perchlorate (NaClO4) or sodium hexafluorophosphate (NaPF6) within an ethylene carbonate/propylene carbonate (EC:PC) solvent mixture. (Ponrouch et al., 2012) However, it is worth noting that the solvents shown in figure 3 are not the only compatible solvents that can be used with sodium-ion batteries. Tetraethylene glycol dimethyl ether (TEGDME) is another. (J.-Y. Hwang et al., 2017)

1.4.2 Additives

Additives can be but are not always included in the organic electrolyte composition. They are added into the salt/solvent mixture to enhance the electrolyte further; only very small amounts are used (usually less than 10% total). (Lin et al., 2019) There are 3 common enrichments that additives can have; these include bulking properties, prevent unwanted overcharging and film-forming. FEC one of the additives in figure 3 is one of the most promising film-forming additives which has had significant research. Film-forming additives work by modifying the interfacial chemistry; by doing so this offers stability within the sodium-ion battery and performance enhancements including the cycling of the battery. (Lin et al., 2019)

1.4.3 Binders

Another key area that has seen considerable development is the choice of binders used, as seen in figure 4. Binders are used within the electrodes, essentially holding all the components together. They can also stabilise the surface of the electrodes. The most widely used binder is polyvinylidene fluoride (PVDF) which is a plastic-based binder. It offers some of the best electrochemical performance and is chemically stable when using a vast range of materials. Besides PVDF another promising plastic-based binder is Polytetrafluoroethylene (PTFE). (Yabuuchi et al., 2014b) Unfortunately, there are some drawbacks using these binders. Very polar, volatile solvents need to be used in the development and synthesis of the electrodes which have negative unwanted toxic properties, the production cost is relatively high compared to other binder alternatives. (Cai et al., 2009; Lux et al., 2010) Thus, potential non-plastic substitutions have been researched thoroughly. Water-based alternatives have recently become promising due to their solubility in water which is essentially a non-toxic and non-volatile solvent. These include poly(acrylic) acid (PAA), sodium alginate (Na-Alg) and sodium carboxymethyl cellulose (Na-CMC). (Ming et al., 2015; C. Wang et al., 2013) These offer performance benefits such for cycling due to offering stability during sodiation/de-sodiation processes which involve large volume changes of the electrode structure to occur. Na-CMC is derived from cellulose, is inexpensive and environmentally friendly. It has also been observed to have positive effects with regards to solid electrolyte interface (SEI) layers. (Ming et al., 2015) It has been reported by Dahbi et al. that Na-CMC potentially offers superior performance to that of PDVF through higher cycling efficiency and capacity retention; these advantages have been associated through an even dispersion/coverage throughout the electrode. (Zhang et al., 2016) Both Na-Alg and Na-CMC have been shown to have superior cycling compared to that of PVDF after 100 cycles. (F. Zhao et al., 2016) Thus, the more traditionally used plastic-based binders which have shown great chemical stability throughout sodium-ion battery research may soon be replaced by water-based binders.

1.4.4 SEI layer

Every type of alkali metal-ion battery including lithium and sodium-ion batteries will develop a solid electrolyte interface (SEI) layer on the surface of the anode when using liquid electrolytes. (Bommier & Ji, 2018) The formation of the SEI layer is caused by the decomposition of the electrolyte during the first couple of cycles. (Martinez de la Hoz et al., 2015)

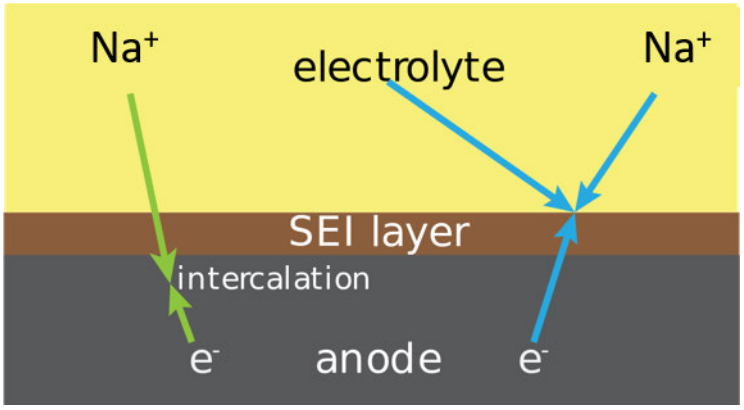

Figure 1.4: SEI layer diagram showing formation on sodium-ion anode

Figure 1.4 above shows a schematic representation of the SEI layer for a sodium-ion battery. The top yellow section of the schematic represents the liquid electrolyte, with the SEI layer forming in between the liquid electrolyte and anode. It can still be seen that intercalation can still occur through the SEI layer into the anode; this is shown with the green arrows. The SEI layer plays a crucial role in sodium-ion batteries however it has both benefits and disadvantages. It offers protection to the anode by preventing the transfer of electrons from the anode to the cathode yet continues to allow the intercalation/de-intercalation of the sodium-ion batteries from the electrolyte into/out of the anode. Thus, the SEI layer is both an electrical insulator as well as an ionic conductor. (Martinez de la Hoz et al., 2015) Although, once the SEI layer has formed it results in a permeant loss of capacity. Thus, optimisation of the SEI layer is always needed to ensure the benefits outweigh the negatives. (Bommier & Ji, 2018) There is potential promise however, with sodium-ion batteries the formation of the SEI layer can be tuned. Pre-cycling the anode allows a stable SEI layer to form uniformly across the anodes surface optimising the performance. (Mogensen et al.,

2016; Peled & Menkin, 2017) Further negative effects of the SEI layer have been seen in high capacity sodium-ion anodes where the initial SEI layer can rupture during cycling. This then re-exposes the anodes surface allowing another SEI layer to form. By doing so it reduces onto the anodes surface and degrades the liquid electrolyte further reducing the cycling performance and increases cell degradation contributing to failure of the battery. (Mogensen et al., 2016) Thus, the SEI layer is a critical part of a sodium-ion battery that requires continuous refinement to gain the benefits that it offers to the battery.

1.5 Carbon-based Anodes

One of the most promising anode materials the has become key for the future of sodium-ion batteries is Hard carbon (HC). Initial research into hard carbon was investigated alongside graphite during the development of lithium-ion batteries. (Liu et al., 1996) Preliminary results suggested that hard carbon offered a higher capacity and electrolyte compatibility to that of graphite; solvent intercalation caused exfoliation of the graphite. (Xing et al., 1996a) However, the breakthrough for graphite occurred during the synthesis of ethylene carbonate-based electrolytes. These then perfected the SEI layer formation on the graphite without the issues of exfoliation. This led to incredible performance enhancements through long cycling stability, a wide voltage window and a high capacity. This then resulted in superior capabilities to that of hard carbon. (Aurbach et al., 1996) Consequently, with the development of sodium-ion batteries attention has turned back to hard carbon through greater understanding of electrolyte interactions, SEI formation and other potential offerings. (Hou et al., 2017; Wahid et al., 2018)

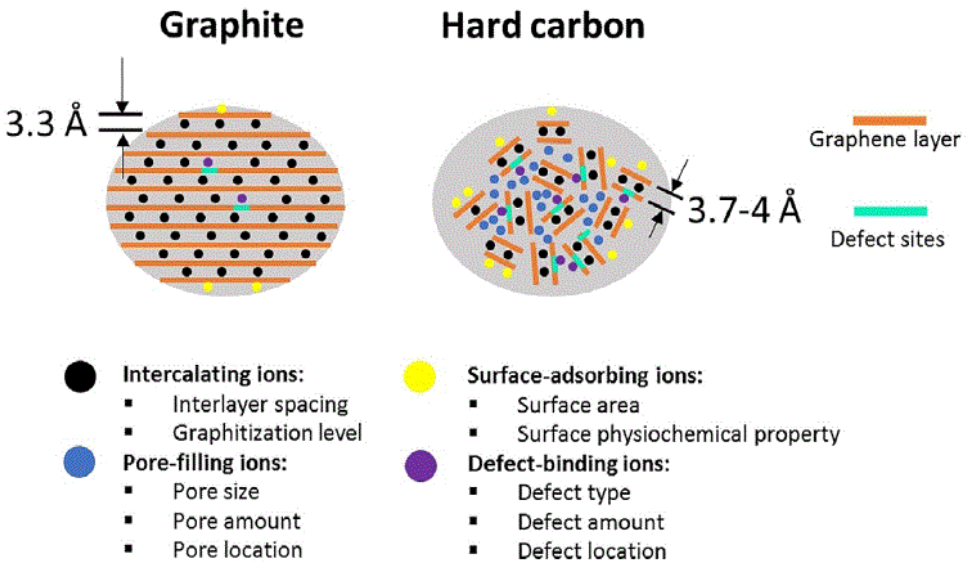

Figure 1.5: A comparison between the structures of graphite and hard carbon (Xiao et al., 2019)

As discussed previously, significant differences between the structures of graphite and hard carbon are represented in figure 1.5 above. On the left, graphite has the ordered structure as previously mentioned with a consistent interlayer spacing between the graphene sheets. The intercalating ions are consistently maintained within the uniform structure; a few defect sites can be seen represented by the light green lines however these are negligible. On the right however is the hard carbon, the structure is extremely disordered, considerable variation in the interlayer spacing (3.7-4A) and a considerable number of defect sites. Also, there are multiple types of ions interacting with the graphene layers unlike that observed with the graphite. Nearly all the ions involved with the graphite structure are intercalating ions; these can be seen within the hard carbon however they are not the sole type. Besides the intercalating ions, there are pore-filling, surface-adsorbing, and defect-binding ions, all of which are of roughly the same quantity. (Xiao et al., 2019)

Lithium as discussed, readily intercalates into graphite however this is not the same for sodium. After intercalation, lithium forms a stoichiometry of LiC6 in the graphite. Unfortunately, there are no stable Na-C compounds, this severely hinders graphite as an anode material for sodium-ion batteries. Sodium can plate onto the carbon surface

of graphite thus a very small capacity can be achieved. (GE, 1988; Metrot et al., 1980) Density functional theory (DFT) was undertaken by Grande et al. to calculate the binding energies for group 1 metals (lithium, sodium, and potassium) and graphene sheets; they determined that the only unfavourable intercalation compound energetically was NaC_6. (Z. Wang et al., 2014) Further studies have also suggested that the physical size of the sodium atoms hinders the intercalation also. (Dahbi et al., 2014; Wen et al., 2014) A potential way to compensate for the limitations of sodium with graphite was the development of expanded graphite. Wang et al. utilised a multi-step oxidation-reduction method expanding the interlayer spacing between the sheets whilst maintaining the long-ordered structure. This then successfully accommodated the sodium atoms larger size through showing an increased interlayer spacing of 0.43 nm. [78] Electrochemical testing of their EG showed a promising highly reversible capacity of 284 mAh g^{-1} using a current density of 20 mA g^{-1}; 184 mAh g^{-1} at 100 mA g^{-1} after cycling 2000 times a capacity retention of 73.92% was achieved (Wen et al., 2014) There has been significant interest in the impact of different electrolytes being used with EG regarding performance increases and the SEI layer formation. Hu et al. showed this through using both ester and ether-based electrolytes. Using a nitrogen doping expansion method to synthesize the EG the ester-based electrolyte achieved a capacity of 125 mAh g^{-1}; with the ether-based being 110 mAh g^{-1} at 30 mA g^{-1}. The differences were attributed to the SEI layers being formed. (Wen et al., 2014)Thus, expanded graphite has been seen to be a promising anodic material; however significant variations have been observed depending on synthesis methods and electrolytes used.

1.5.1 Hard Carbon – introduction

Hard carbon is a general classification for carbonaceous materials that do not transform into graphite at temperatures exceeding 3000 °C, synonymously ‘non-graphitizable carbon’ is used. (Stevens & Dahn, 2001) However, it needs to be considered that carbons that have high mechanical hardness can be graphitizable, and non-graphitizable carbons can also be soft. An example being aluminium cells use an extremely hard, yet graphitizable carbon electrode. (Stevens & Dahn, 2000)

In literature there as several alternative terms that can be used to describe both ‘non-graphitizable/hard’ carbons. Multiple terminology has been used depending on which research field is of interest, mismatching definitions. Common examples of this includes ‘amorphous- ‘, ‘disordered-’ and ‘non-graphitic’ carbon’. This has resulted in inaccurate definitions regarding specific carbon structures. A well-known example is even though non-graphitizable carbons do not offer an ordered long-range disordered structure, the term ‘amorphous’ is an incompatible definition, amorphous carbons can only compromise of localized π-electrons as described by Philip Warren Anderson, Nobel laureate. (Buiel & Dahn, 1999)Diamond-like carbons are good examples of amorphous carbons, which are also commonly known as hard amorphous carbons. Furthermore, a distinction between ‘non-graphitic’ and ‘non-graphitizable’ must be made clear as graphitizable carbons are fundamentally non-graphitic before they are graphitized.

1.5.2 Carbonization

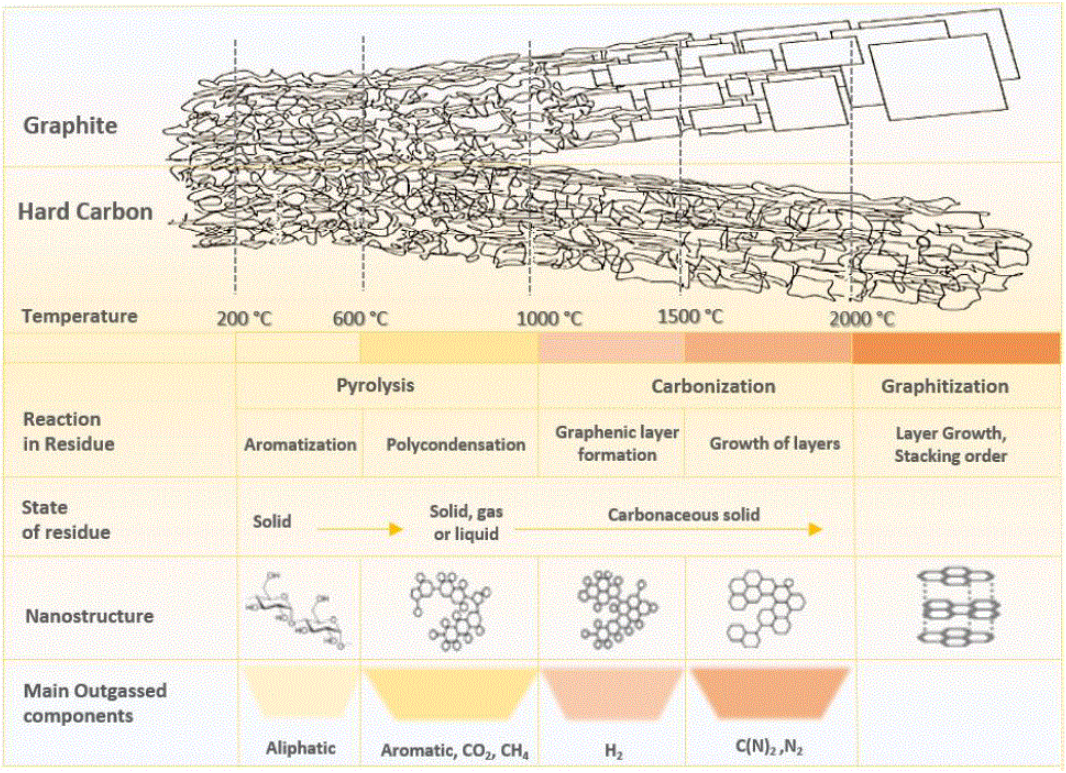

Figure 1.6: Hard carbon carbonization relative to temperature (Marsh, 2006)

For the use in sodium-ion batteries; hard carbons are usually synthesized by chemical or thermal processes (Marsh, 2006) There are multiple potential precursors including natural and synthetic polymeric structures, all of which decompose with increased

temperatures. This decomposition process is known as carbonization; it results in an increased carbon content within the material. As the precursors begin to carbonize small molecules including CO_2, N_2 and H_2O are released (Marsh, 2006) as shown in figure 7 above. This process leads to materials having high porosities (up to 1000 m^2 g^{-1}) (Marsh, 2006), lower densities, both true and bulk (including/excluding the open and closed pores respectively of 2.0 g cm^{-3} (Z. Li et al., 2017) and 1.5 g cm^{-3} respectively. It is worth noting that the pores created during carbonization are not necessarily always open; particularly at temperatures exceeding 1200 °C which has reportedly let to decreased surface areas of less than 50 m^2 g^{-1}. (Buiel & Dahn, 1999) Multiple concurrent reactions occur during the carbonization process including hydrogen transfer, condensation, and dehydrogenation. The precursors of the non-graphitizable carbons retain their structures throughout the carbonization process not converting into a fluid phase which is the case with their graphitizable counterparts. (Marsh, 2006) Thus, the structure of the synthesised hard carbon has nearly an identical morphology to its precursors, albeit with a lower density. (Wahid et al., 2017)

During the final solid-phase stage of the carbonization process, this ultimately determines the hard carbon when the heat treatment is finished. Generally, greater stability within internal structures is formed progressively at increased heat treatment temperatures (HTT). Each HTT is associated with a specific structure of carbon, that has essentially been "frozen" at that unique HTT. (Marsh, 2006) Consequently, multiple carbon materials and structures can be achieved through one precursor. This then allows exploration of the carbonization conditions to refine and optimise carbon materials to obtain enhanced structural and morphological properties. (Y. Li et al., 2016)

During carbonization, some carbon atoms enable atomic reorganization due to a degree of mobility through the decomposition of the precursor. The atomic reorganization increases greater stability through the formation of the optimal six-membered carbon ring system within the microstructure. This atomic reorganisation involves heteroatoms including oxygen and hydrogen adding to the redefined carbon-based structure. As every precursor decomposes uniquely, however carbon migration, co-bonding formations and vacancy formation allow greater stability of the structures. The structural changes create atomic dimensions which influence the porosity of the new microstructure. The dimensions of the pores are commonly used to describe the

porosity. Micropores and mesopores are the frequently observed type, <2.0 nm and <50 nm respectfully. Nano-porosity is becoming popular within ion-based batteries research that has a pore side of <1.0 nm. (Marsh, 2006) As previously stated, non-graphitizable carbons are synthesised through solid-state carbonization. However, graphitizable carbons are usually synthesised through liquid or gas phase carbonization. The majority are produced by polymers and aromatic compounds of which are non-porous. This lack of porosity explains why graphite has a significantly higher density to that of the non-graphitised ones. (Marsh, 2006)

1.5.3 Hard Carbon Structures

As previously discussed, hard carbons have an ability to maintain their precursor morphology up to very high temperatures. (Marsh, 2006) Strong cross-linking within the structures is primarily responsible for this, preventing graphitization from occurring. The pyrolysis stage determines the degree of crosslinking dependent on the aggregation that occurs during the stage. The graphenic layers form and stack upon one another after the carbonization stage as shown in figure 7; once formed these sheets cannot be altered further to aid stacking. (Z. Li et al., 2017) Dahn et al. labelled these regions as being aromatic fragments which had multiple layers parallel to one another, with lateral dimensions of 40 Å. (Stevens & Dahn, 2000)Lui et al. however suggested 3 to 5 layers stacked randomly R. Franklin in 1951 stated the layers vary between 2 and 4 sheets which rises up to 11 at increased pyrolysis temperatures over 3000 °C, characterised by the already formed interlayer cross-linking which were created below 1000 °C. (Franklin, 1951) The exact nature in how the cross-linking has not been determined yet in detail, it is widely agreed that the C-O-C covalent bonds play a crucial role throughout, including the hardness and preventing graphitization. (Marsh, 1989)

The structure of hard carbon can be macroscopically described through distinct fragments of graphenic sheets; these include curved, bent, twisted, rumpled, buckled and non-planar sheets. (Z. Li et al., 2017) On average, the graphene sheets roughly have a radius of curvature of 16 Å. (Stratford et al., 2016) Van de Waals forces allow the sheets to be partially stacked; (Harris, 2005) however they are unable to be

flattened or unfolded. [94] Even with the partial stacking, the orientation of the layers is relatively turbostratic and rather randomic, both of which lead to pores and voids forming with a wide breadth of shapes and sizes (Marsh, 1989) Alternative attempts have attempted to determine the structure of hard carbons suggesting that they could be fullerene-like, (Harris, 2013) which include sp^2-hybridized carbon[92] contained within a network of multiple shapes including hexagons, disruptive pentagons and heptagons as well as defects. (Harris, 2005) Furthermore, there could potentially be a significant number of sp^3-hybridized carbons also within the inter-layers, however this is still being debated. (Harris, 2013) There could potentially be other types of defects present, including Stone-Thrower-Wales defects with adatoms (Robinson et al., 2017; X. Wang et al., 2014) , empty sites, (Morita et al., 2016) and heteroatoms (X. Wang et al., 2014) all of which destroy the consistency of the graphenic sheets. Additionally, there is also the potential for the graphenic layers to be linked through Wigner defects (interlayer double vacancies) that form 'bridges' and chains between them; (Robinson et al., 2017) these can then add to non-graphitizable effects. (Marsh, 1989)

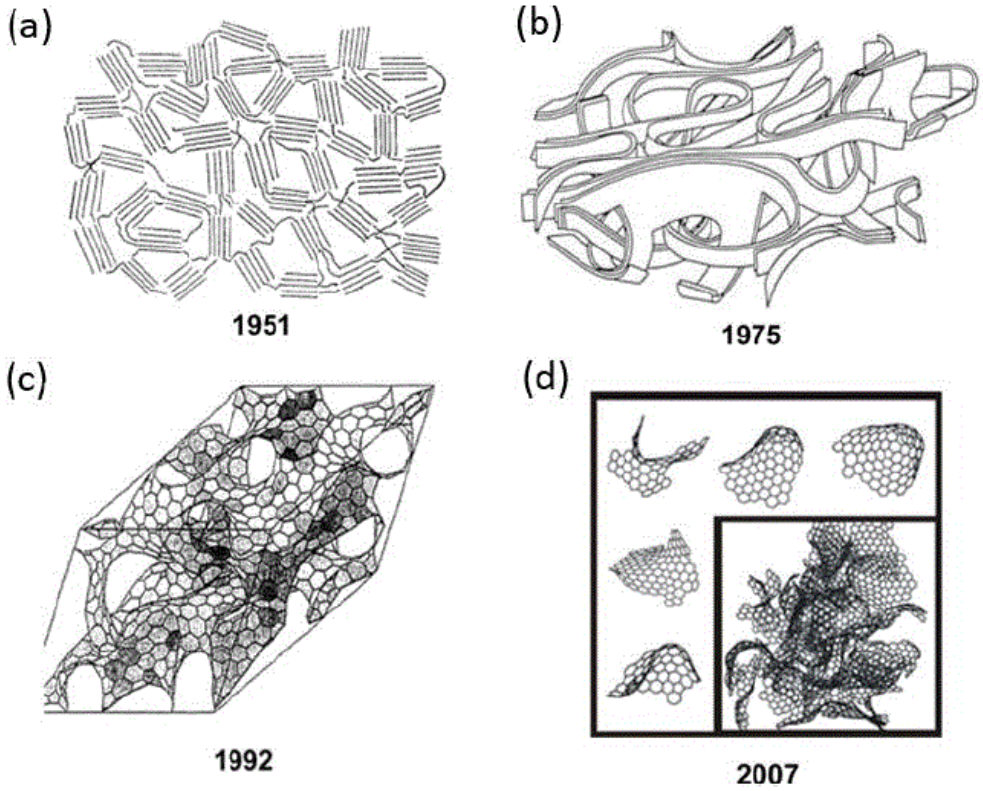

Figure 1.7: Various models/illustrations of the structure of hard carbon inc. year (a) (Franklin, 1951) *(b)* (Ban et al., 1975) *(c)* (Townsend et al., 1992) *and (d)* (Terzyk et al., 2007)

As seen in figure 1.7 above since 1951 initially by R. Franklin, there has been multiple attempts to visualise the structural features of hard carbon. ("Crystallite Growth in Graphitizing and Non-Graphitizing Carbons," 1951) The 2-D structure put forward by R. Franklin was replaced for 3-D models to visualise the graphenic structures more effectively. (Ban et al., 1975; Townsend et al., 1992) One key structural property of hard carbon that is still under discussion is the porosity; however, the intricate nature of porosity makes it difficult to visualise. The most accepted model currently is the "house of cards" model which has been put forward by Dahn et al. shown below in figure 9. (Dahn et al., 1997a) This model is used to describe the storage mechanisms into hard carbon for both lithium and sodium. It is based upon two parts; with the first focusing on a model to describe the structure of hard carbon. (Dahn et al., 1997b) The second focusses on the intercalation of lithium/sodium whilst being used as an electrode. Regarding the first part of the model, suggest that there is a blend of graphite-like crystallites (including sp^2-hybridized parallel graphene layers) as well as amorphous regions (sp^3-hybridized, defects within the layers).

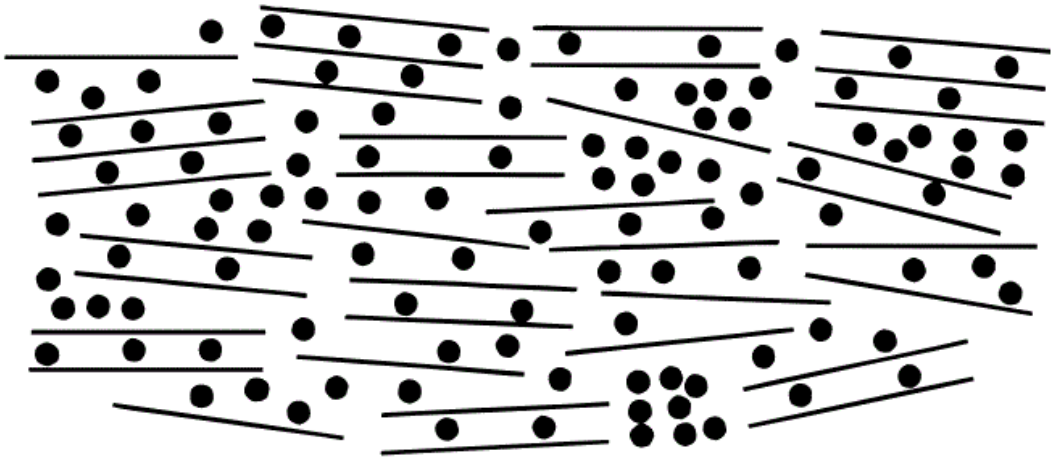

Figure 1.8: "House of cards" model suggested by Dahn et al. (Dahn et al., 1995)

The name was coined due to the resemblance of the relatively random orientation of the layers where 2 or 3 layers are parallel to one another; this ordering has been said to be like that of a "house of cards". (Zheng et al., 1996)The lithium/sodium is represented by the black dots.

Recently, uncertainty have been raised regarding the graphitic crystallites within the structure. Other descriptions suggest graphitic crystallite domains are in fact stacked randomly for porosity, as put forward by D. Ruthven. (Helfferich, 1985) Then again, H. Marsh emphasised that even though Dahn et al. model does show an association between structure and porosity, the suppositions do need to be reassessed. (Marsh, 2006) He theorised that the existence of the graphitic crystallites is more suited in describing graphitic carbons including carbon black, instead of hard carbons (non-graphitizable).

1.5.4 Hard Carbon Sodiation pathways

Anodes for lithium/sodium-ion batteries need to offer a high specific capacity as discussed, however they crucially need a low voltage potential to achieve this. Thus, it is necessary to comprehend the intercalation and transfer pathways involved. A characteristic discharge curve of hard card in a half-cell with sodium can be seen in figure 10 below. The discharge curve can be separated into two distinct sections, the first part being a sloping section followed by a plateau section. Within literature, there has been constant debate of how the intercalation process occurs during these two distinct regions with regards to the mechanisms involved.

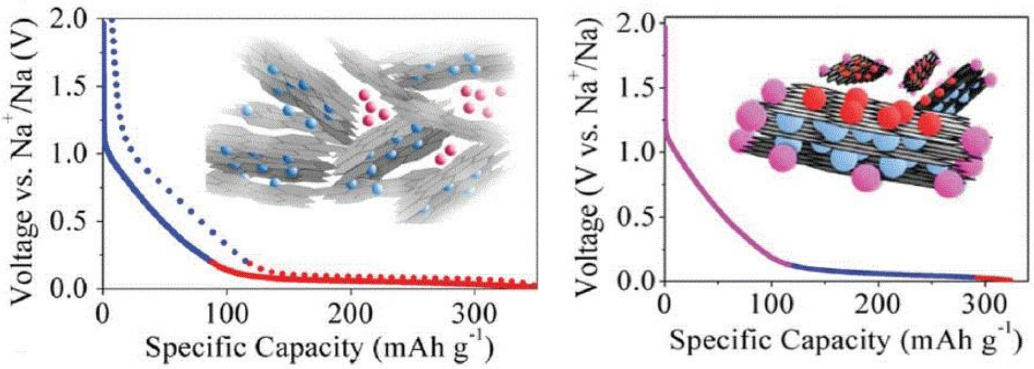

Figure 1.9: Traditional intercalation model suggested by Dahn et al. (left), and an alternate model suggested by numerous recent articles (right). (Saurel et al., 2018)

In figure 1.9 above, two distinct different intercalation mechanism schematics as previously discussed can be seen. On the left, Dahn et al. suggest that first region represented by the blue line/spheres is where the sodium ions intercalate in-between the graphitic layers. As the voltage further decreases the second region represented by the red line/spheres, this is where the sodium-ions 'fill' the nano porosity in-between the randomly orientated graphitic layers. (Stevens & Dahn, 2000, 2001) The sloping of the lines relates to the increased intercalation of the sodium ions, as the voltage decreases the ions can alter the width of the graphitic layers allowing for further intercalation. This proposal has been backed in literature, Komaba et al. supports this through using ex situ XRD, an interlayer expansion between the graphitic layers was observed during sodium-ion intercalation when hard carbon was discharged down to

0.1 V. (Komaba et al., 2011) Small-angle X-ray scattering (SAXS) allowed analysis of the hard carbon below 0.2 V and indicated that there was a reversible decrease in density occurring implying sodium-ion intercalation into nanopores within the hard carbon. (Komaba et al., 2011)

The alternate model includes an additional region. Ding et al. determined that the plateau capacity which is observed at the low voltages was not positively proportionate to the porosity of the hard carbon. Additionally, between 0.1-0.2 V there was further interlayer expansion between the graphitic layers (Ding et al., 2013) which proposes additional intercalation occurring (indicated by the red line/spheres) and not the suggested pore filling than the Dahn model suggests. Thus, amendments to the Dahn model may be required.

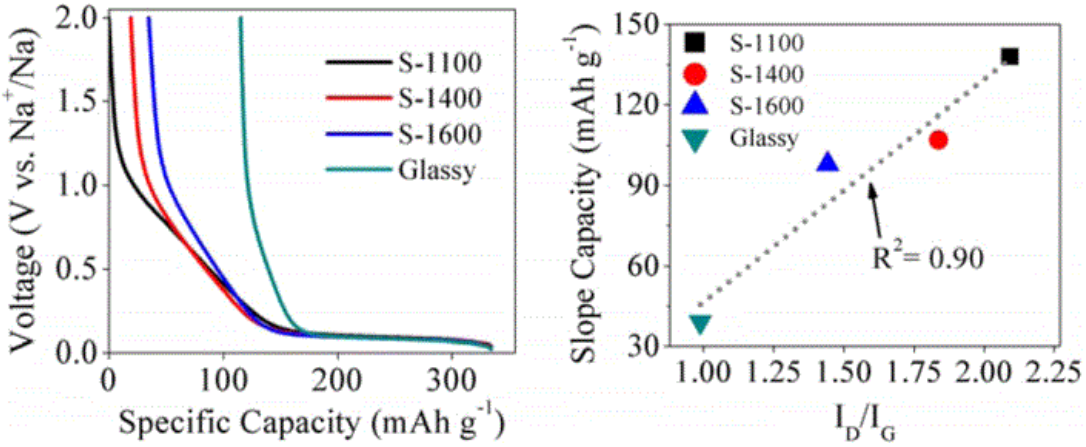

Figure 1.10: (a) sodiation profiles for various carbons, (b) sloping capacity vs ID/IG ratio plot (Bommier et al., 2015)

Furthermore, Bommier et al. showed that with increasing pyrolysis temperature, there was an increase in the size of the turbostratic nanodomains as well as a decrease in the interlayer spacing. [119] As shown in figure 11, it was observed that the sloping region had a decreased capacity, where the plateau region had an increased capacity with a growth of turbostratic nanodomains. Intercalation of sodium ions is unmistakeably more favourable with larger turbostratic domains; this shows that sodium-ion intercalation is associated with the plateau region rather than the sloping region.(Bommier et al., 2015) Additionally, it has been speculated that the sloping region is probably related to the defects within the hard carbon. This is the complete opposite to the ideas put forward by the pore filling model put forward by Dahn et al.

Thus, there is ambiguity into the intercalation process regarding the sodiation pathways.

1.5.5 Hard Carbon Synthesis conditions

As previously discussed, hard carbon is not one material, but a group of non-graphitizable carbons that have undergone high temperature pyrolysis. Thus, the synthesis conditions can vary quite significantly. Common precursors include simple carbohydrates including sucrose and glucose; peels from a wide variety fruits including banana peels. Natural polymers are widely used due to their abundance, such as lignin and cellulose. Natural biomasses potentially offer good precursors also. (El Moctar et al., 2018)

The synthesises often have multiple stages with various ramp rates and temperatures being used. Dahn et al. were one of the first to optimise the pyrolysis of sugar to make hard carbon for lithium-ion batteries in 1996. A pyrolysis range of 600-1600 °C was chosen, it was determined that 1050 °C was the optimum pyrolysis temperature. They concluded that it is vital to have a slow heating rate with a high argon flow for when the gases from the pyrolysis are released. (Xing et al., 1996b) Dahn et al. then applied their pyrolysis conditions to sodium-ion batteries. They chose pyrolysis temperatures of 1000 and 1150 °C with a dehydration step in air at 180 °C beforehand.

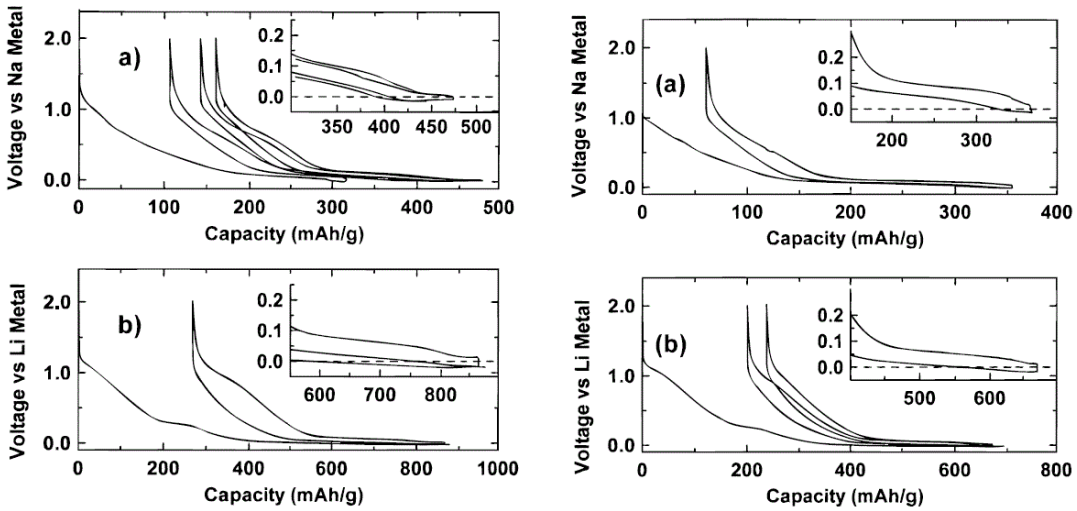

Figure 1.11: left (a) sodium profile at 1000 °C, left (b) lithium profile at 1000°, right (a) sodium profile at 1150 °C, right (b) lithium profile at 1150 °C (Stevens & Dahn, 2000)

As seen in figure 1.11 above, Dahn et al successfully refined their initial pyrolysis technique with lithium-ion to work effectively with sodium-ion batteries. (Stevens & Dahn, 2000)This then allowed substantial research into hard carbons suitable for the use with sodium-ion batteries.

Simone et al. through inspiration of Dahn et al. work researched multiple pyrolysis temperatures using cellulose. Multiple temperatures were chosen between 700-1600 °C closely following the conditions used by Dahn et al, specifically for the use with sodium-ion batteries. It was concluded that the best electrochemical performance through using cellulose as a precursor for the hard carbon was 1600 °C. Sun et al. conducted a similar study using biomass-derived hard carbons and concluded that the best pyrolysis temperature was 1200 °C. (Sun et al., 2015) Thus, there is no specific optimum pyrolysis temperature for hard carbons due to the wide number of precursors that can be used.

1.5.6 Hard Carbon Structural modifications

As with expanded graphite, structural modifications can be used to increase the interlayer spacing between the graphene layers of hard carbon to improve the intercalation prospects. The most common ways to do this include influencing by elemental doping and influencing the pyrolysis conditions during synthesis. Yang el al. for example successfully were able to s-doped, n-rich nanosheets using both polyaniline and cellulose microspheres which allowed Faradic reactions to thrive between the sodium ions. (Yang et al., 2017) These outstanding results verified the increased ability for intercalation through doping which enabled positive structural enhancements. The doping emphasises the influence of the hard carbon that help the growth of defects; decreasing the diffusion batter limitations and then boasts enhanced conductivity. (D. Xu et al., 2016) A significant potential modification is the influence of surface area; larger surface areas offer for increased abundance of intercalation pathways. However, this is a trade-off as it then accelerates unwanted side reactions between the electrolyte and hard carbon electrode causing a significant first cycle capacity loss. Kun-lei Hong et al. showed reported this through the pyrolysis of pre-activated pomelo peel achieving an incredible 1272 $m^2 g^{-1}$, however only achieved a first cycle efficiency of 21%. (Hong et al., 2014)Thus, structural modifications to hard carbon can successfully offer the potential for improved performance, although significant optimisation is required for this.

1.5.7 Hard Carbon Graphene Oxide

Previously, it was discussed that a larger surface area improves sodiation pathways, however the larger surface areas have a detrimental impact from the first cycle, causing a significant first cycle capacity loss. (Hong et al., 2014) Thus, there has been research into using low surface areas to see if there are any performance benefits and to potentially reduce the first cycle capacity issues. Luo et al. successfully doped graphene oxide into a sucrose precursor which significantly lowered the surface area of the hard carbon. (W. Luo et al., 2015c) They reported a surface area of 5.3 $m^2 g^{-1}$ through the doping of sucrose; whilst their undoped hard carbon had a surface area of 137.2 $m^2 g^{-1}$. However, introducing graphene oxide has been reported to significantly increase the surface area of composites through single layer graphene having a theoretical surface area of 2630 $m^2 g^{-1}$. (Zhu et al., 2010) To fully comprehend why the inclusion of graphene oxide lowers the surface area analysis of the synthesis steps need to be understood in more detail.

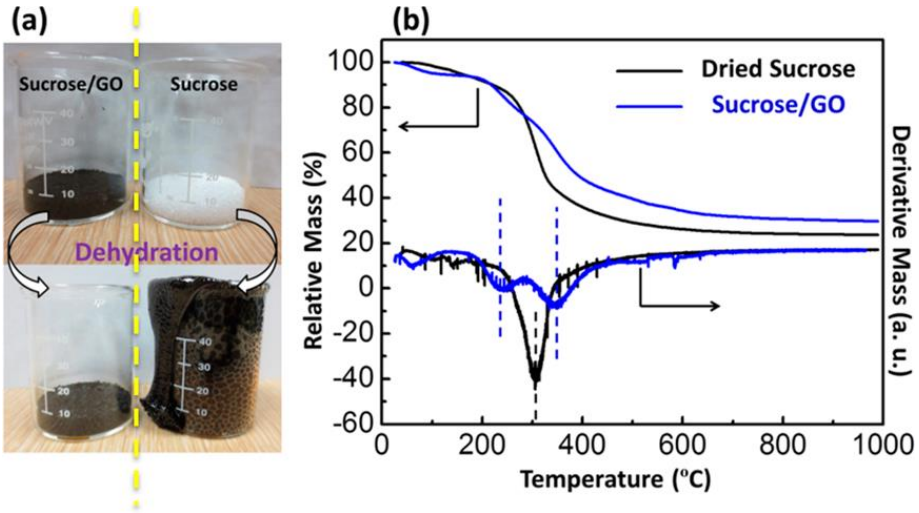

Figure 1.12: (a) the dehydration of both sucrose/GO and sucrose, (b) TGA comparison (W. Luo et al., 2015c)

Luo et al. showed that the dehydration step of sucrose before pyrolysis plays a critical role in the synthesis of the hard carbon. During the dehydration step, caramelisation begins where sucrose undergoes significant volume expansion through foaming as seen in figure 13a. The inclusion of GO hinders this foaming. Through TGA analysis

they determined that GO helps widen the temperature range of the burn-off of the sucrose during pyrolysis which then facilitates the decrease in surface area.

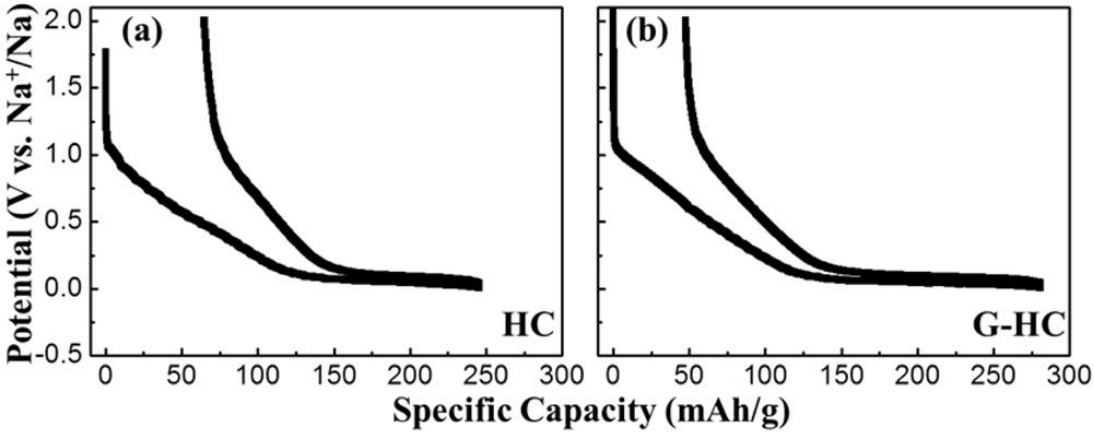

Figure 1.13: Comparison of first cycles between hard carbon (a), and GO doped hard carbon (b) (W. Luo et al., 2015c)

It was seen that the GO doped hard carbon achieved a first cycle coulombic efficiency of 83%, compared to 74% for the undoped hard carbon. Achieving 83% is one of the highest ever for carbon-based anodes used with sodium-ion batteries. (Y. Li et al., 2015) Luo et al. theorised that doping of GO allows volatile molecules that are created during the dehydration and pyrolysis stages to relocate along the GO nanosheets whilst not creating pores preventing an unwanted increase in surface area. (W. Luo et al., 2015c)

Therefore, GO has the potential to enhance the performance of hard carbon-based anodes through influencing the surface area by preventing unwanted side effects; even though the process in by which this is achieved has only be hypothesised. Yet, the performance benefits speak for themselves and including GO into hard carbon has an important future with sodium-ion batteries.

1.6 Cathodes

Cathodes play a fundamental role within the development of batteries, including sodium-ion batteries. They play a crucial role in ensuring high specific energy, capacities and cycling life. They hold great potential to improve the voltage windows used for sodium-ion batteries. (Kundu et al., 2015) There are multiple compounds that can be used as effective cathodic materials as shown below in figure 1.14.

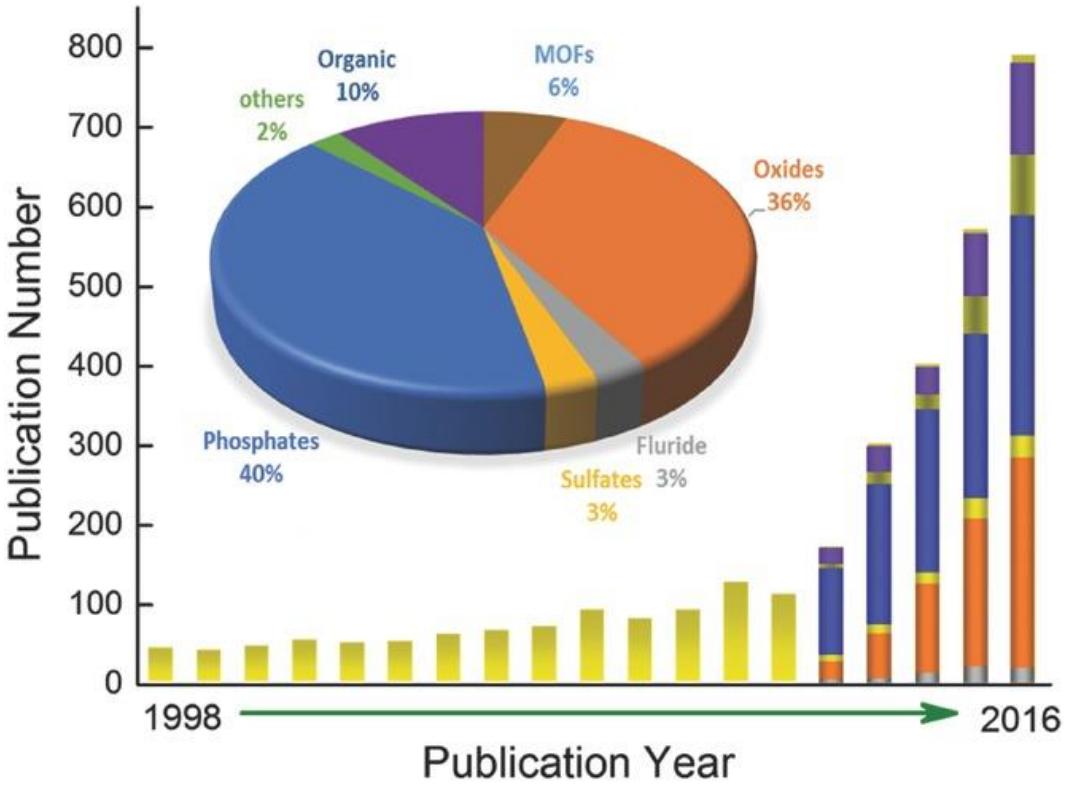

Figure 1.14: An overview showing the number of publications for different types of cathodes for sodium-ion batteries (Dai et al., 2017)

As shown above in figure 1.14 there are variety of compounds that are compatible for use as a cathode for sodium-ion batteries. These can be separated into organic, MOFs, oxides, fluorides, sulphates, phosphates, and a few others.

One of the most researched cathodes are metal oxide-based compounds. These include metal oxides which offer good conductivity and ease of synthesis. The most researched

metal oxides include vanadium, manganese, and molybdenum. These offer acceptable electrochemical properties with high cycling stability and specific capacities. (Dai et al., 2017)Out of the three, vanadium has for over a long period of time remained an encouraging potential cathode through vanadium oxide through promising structural flexibility and high abundance and offers a theoretical capacity of 323 mAh g^{-1}. (Ali et al., 2016) Manganese dioxide has been suggested to be a direct competitor to vanadium oxide by offering comparable interstitial sites for sodium ion transport and storage. Initial capacities of 350 mAh g^{-1} have been achieved. (Leong et al., 2016)

Phosphates have also been evaluated for use with sodium-ion batteries. $LiFePO_4$ is widely used with lithium-ion batteries. The sodium analogue equivalent $NaFePO_4$ has been widely researched; a theoretical capacity of 154 mAh g^{-1} has been calculated. (Dai et al., 2017) Another key phosphate-based cathode is $Na_3V_2(PO_4)_3$, which utilises an open 3D structure enabling a theoretical capacity of 117.6 mAh g^{-1} (Saravanan et al., 2013), however refinements to this cathode have been proposed to further enhance and stabilise the cyclability and reversibility and increase capacity potentially through the inclusion of carbon coating and embedding techniques. (Saravanan et al., 2013)Pyrophosphates and fluorophosphates are additional phosphate-based cathodes which potentially offer greater properties. Pyrophosphates are based upon $Na_2MP_2O_7$ (M = Fe, Mn, Co) and offer greater thermodynamic stability and can easily be synthesised by thermal decomposition of phosphates through oxygen evolution. (Dai et al., 2017) The strong inductive effect of fluorine in fluorophosphates allows for a higher operating potential of up to 4.2 V compared to 3.8 V for phosphates with $Na_4V_2(PO_4)_2F_3$ offering a theoretical capacity of 256 mAh g^{-1}. (Matts et al., 2015)

Organic compounds are another widely researched potential group of compounds that have successfully been seen to work well as cathodes for sodium-ion batteries. Of which can be split into 3 major subgroups: metal-organics, organics, and organic polymers.

Metal-organics are based upon Metal hexacyanometalates, the general chemical formula is $AxMM'(CN)_6$ (A = Na, K; M and M′ = Fe, Co, Mn, Ni, In). These compounds offer a cubic structure which has metal ions located at the corners and having cyanide groups bridging the cubes edges. Each metal ion is co-ordinated octahedrally by either the carbon or nitrogen end of each cyanide group. (Dai et al.,

2017) This unique metal hexacyanometalate structure offers intercalation/de-intercalation of alkali metal ions including lithium and sodium as favourable interstitial sites are available. The most well-known metal-organic compound for use with sodium-ion batteries are Prussian blue analogues. These were first researched by Goodenough et al. who synthesised and analysed a variety of metal-doped frameworks including $KMFe(CN)_6$ compounds (M = Mn, Fe, Co, Ni, and Zn); KFe(II)Fe(III)(CN)6 successfully showed a reversible capacity of 100 mAh g^{-1}. [144]

A variety of organic cathode precursors have been analysed as potential candidates for use in sodium-ion batteries. A common organic group that has been extensively studied are quinone-based derivatives; they use C=O redox centres which are metal-free which have the potential to offer high capacities. (W. Luo et al., 2014) However, one of the most renowned organic compound precursors is sodium rhodizonate. The following sub-chapter goes into this compound in greater detail.

1.6.1 Sodium Rhodizonate

Sodium rhodizonate as stated previously is another example of an organic cathodic precursor. It is a carbonyl-based salt with the chemical formula $Na_2C_6O_6$; this offers a layered structure that is perfect for sodiation/de-sodiation, as shown below in figure 16.

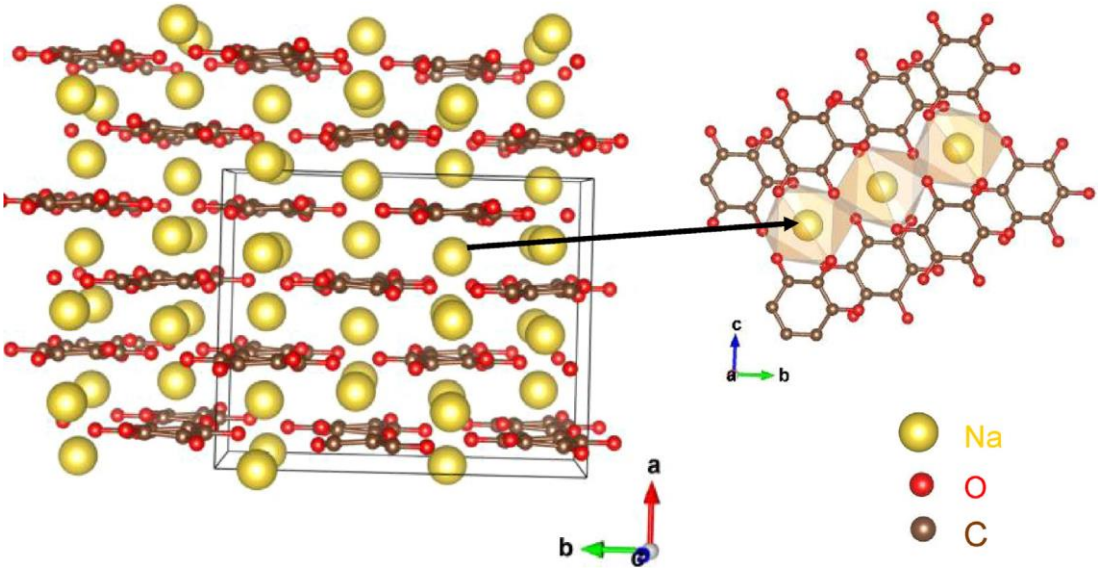

Figure 1.15: Three-dimensional lattice structure of sodium rhodizonate (Chihara et al., 2013)

As seen in figure 1.15, there are alternating layers of Na+ cations packed hexagonally and rhodizonate dianions C_6O_2). The cations lie a/4 above these anions (*Fddd* spacing). [146] The structure is comprised of Na+ ions individually coordinating with 8 oxygen atoms using four different rhodizonate dianions, this then connects adjacent layers together. Each sodium-oxygen bond is ionically bonded and very stable in the common organic solvents which is crucial preventing the dissolution of the sodium rhodizonate with ether and carbonate-based solvents. (Lee et al., 2017)Therefore, sodium rhodizonate is expected to be capable of storing four sodium ions per layer, with a theoretical capacity of 501 mAh g^{-1}. (Dinnebier et al., 2005)

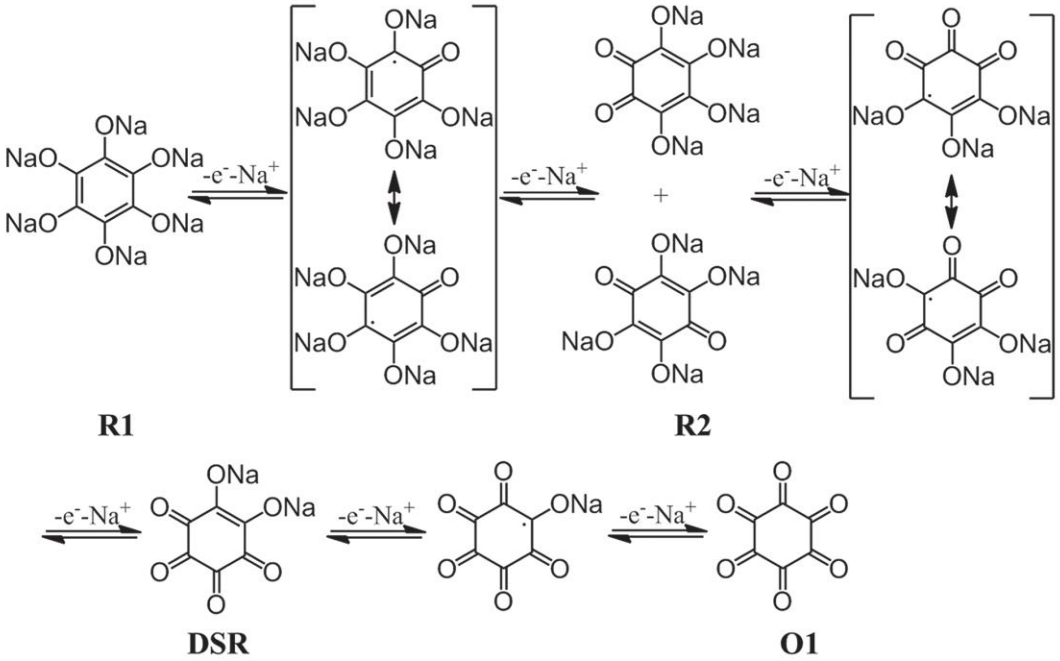

Figure 1.16: Schematic diagram of sodium rhodizonate (DSR) with its discharged states (R1 and R2) and its potential charge state (O1) (C. Wang et al., 2016)

Above, in figure 17 it shown the two discharged states of sodium rhodizonate R1 and R2, DSR which is the rhodizonate salt. O1 is a potential charged state; however, this requires a six-electron transfer from R1. During the sodiation/de-sodiation the redox reaction shuttles the electrons between the DSR state and the discharged R1 state. This is the standard expected transfer of electrons; R2 and O1 are achievable however as shown above in figure 17, however not used due to potential damage and degradation of the sodium rhodizonate. (Qiu et al., 2017)

The particle size of Sodium rhodizonate can easily be manipulated through a Reverse Anti-solvent Crystallization Process which involves dissolving the rhodizonate salt into water and using ethanol to decrease the particle size. The common particle size of bulk sodium rhodizonate is ~20 um with 'nano' rhodizonate decreasing to ~200 nm and below. It has been suggested than smaller particle sizes offer significantly improved kinetics for electrochemical reactions (C. Luo et al., 2014)this has partially been a driving force into the research of nanoparticles for sodium-ion electrodes.

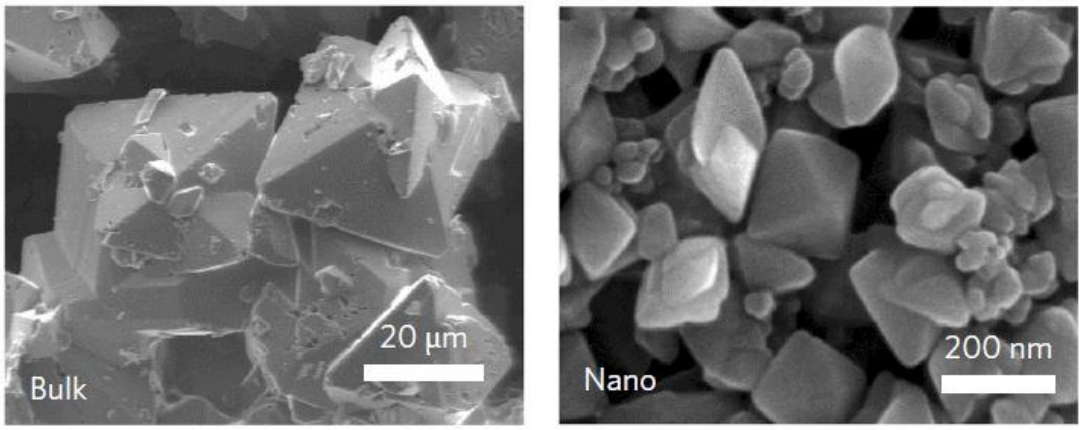

Figure 1.17: SEM images of both bulk and nano preparations of sodium rhodizonate (Lee et al., 2017)

As seen above in figure 1.17, the differences between the bulk and nano are clear with a significant difference in particle size. The size and morphology of the nanoparticles can be influenced further. There are key driving forces for crystallisation that can be controlled, by having a specified concentration/saturation of sodium rhodizonate, a specific volume of ethanol and a specified flowrate of ethanol as the antisolvent. Out of the three variables, the ethanol is the most influential regarding the growth of the crystals, the concentration of the dissolved sodium rhodizonate for the diameter. (C. Wang et al., 2016)

1.7 Reduced Graphene Oxide

Reduced graphene oxide commonly referred to as rGO is a carbon-based material. There are multiple forms of carbon that are studied for use with sodium-ion batteries. These include graphene, graphene oxide and reduced graphene oxide. Figure 1.18 below shows the chemical structures of each.

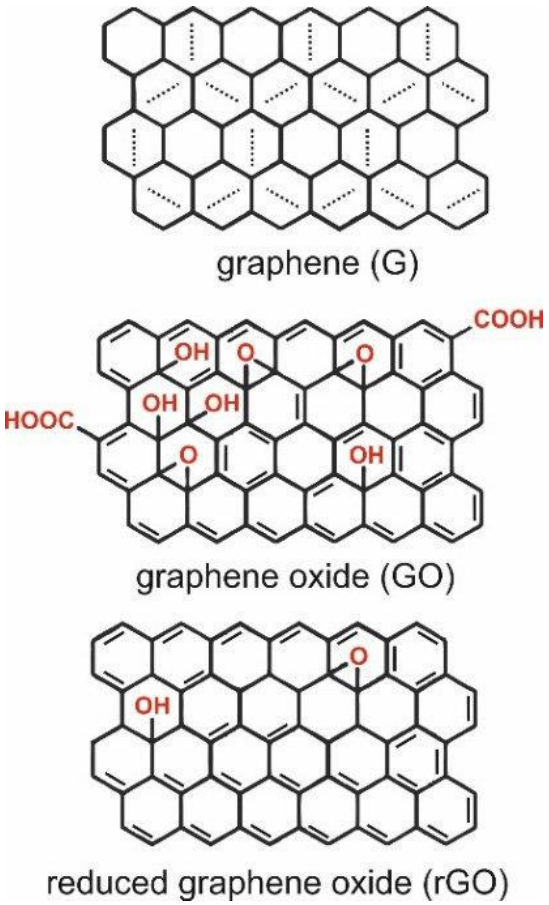

Figure 1.18: A structural comparison between graphene (G), graphene oxide (GO) and reduced graphene oxide (rGO) (Carneiro et al., 2019)

As figure 1.18 above shows, graphene can be defined as hexagonally arranged of sp2-bonded carbon atoms, a sheet a single layer thick. The lateral dimensions of the sheets can vary in size vastly from being several nanometres up to the macroscale. Graphene oxide is a chemically modified type of graphene that is synthesised through oxidation, which in turn causes exfoliation and alters the basal plane. Similarly, to graphene, it has a monolayer structure although it also has a high oxygen content. A C/O atomic

ratio is typically used to characterise with most ratios being below 3.0 and generally just above 2.0. Reduced graphene oxide is graphene oxide as previously mentioned except it has been through a reduction process to reduce the oxygen content. Various reduction methods can be used with thermal and chemical reduction the most widely chosen; the purity of rGO higher through thermal reduction due to no influence by external chemicals. (Bianco et al., 2013)The structure of rGO can vary significantly depending on what reduction process was chosen; defects will always be present due to the nature of the reduction reaction. These defects can include large numbers of defects, edges, and functional groups. (Xiong et al., 2017)

Graphene-based materials have always drawn an interest for the use in lithium-ion batteries; with a considerable research for use with supercapacitors. Although, there are only a limited number of studies looking into the potential use with sodium-ion batteries. One of the forefront graphene-based materials is rGO, which has been verified within multiple studies partially to having a more disordered structure. However, optimisation of the rGO reduction process could offer high sodium intercalation if the defects are carefully utilised. Thus, rGO has the potential to offer a great storage solution for sodium-ion batteries.

Part 2

Experimental Methods

2 Experimental Methods

This chapter focuses on the development of the electrodes throughout. This includes the material characterisation techniques of the raw material. The synthesis of the electrodes, the coin cell preparation and the electrochemical analysis techniques used.

2.1 Materials Characterisation

After the synthesis of the raw materials has been completed, characterisation was undertaken to allow comparisons of the synthesised materials and the results in literature, these included XRD, XPS and SEM analysis.

2.1.1 X-Ray Diffraction (XRD)

X-ray diffraction (XRD) is an empirical technique applied in crystallography and materials science for the comprehensive elucidation of the atomic and molecular structures within crystalline materials. The fundamental principles underpinning this method incorporate both the wave and particle characteristics of electromagnetic radiation, governed by the principle of wave-particle duality.

The procedure commences with an X-ray tube, which generates X-rays by accelerating electrons towards a metallic target, commonly copper or molybdenum, using a high voltage. This interaction induces an electronic transition within the atoms of the target, wherein the inner-shell electrons are displaced. Subsequently, when outer-shell electrons occupy the vacancies left by the inner-shell electrons, they emit energy in the form of X-rays due to the energy level disparity between the shells. The resulting spectrum of X-ray energy is employed in the ensuing diffraction experiment.

The generated X-rays are directed towards the crystalline specimen. Upon penetration, the X-rays interact with the electron clouds of the atomic structures, instigating the

scattering of X-rays in numerous directions — a phenomenon designated as diffraction.

The correlation between the angle of diffraction, the X-ray wavelength, and the interplanar atomic distances within the crystal lattice is encapsulated by Bragg's law. This mathematical expression is written as $n\lambda = 2d \sin \theta$, where n signifies the order of the reflection, λ denotes the X-ray wavelength, d represents the distance between the atomic planes within the crystal lattice, and θ is the angle between the incident X-ray beam and the lattice planes. Constructive interference of the scattered X-rays, resulting in signal amplification and diffraction peak formation, occurs when the conditions of Bragg's law are met. Conversely, when these conditions are not met, destructive interference transpires, leading to signal nullification. The diffracted X-rays are detected, and a diffraction pattern is formulated. This pattern displays a series of peaks at varying angles (2θ), each peak corresponding to a distinct lattice plane group within the crystal. The intensity of each peak is indicative of the type and configuration of atoms within those planes. The resultant diffraction pattern is subjected to detailed analysis involving mathematical and computational approaches. The position, intensity, and width of the diffraction peaks deliver invaluable information concerning the specimen's structure. Peak positions inform about interatomic distances, peak intensities are associated with atomic type and arrangement, and peak widths can reveal information about the crystallite size and lattice strain. The XRD machine used in this work is the Bruker D8 Advance.

2.1.2 X-ray Photoelectron Spectroscopy (XPS)

X-ray Photoelectron Spectroscopy (XPS), also known as Electron Spectroscopy for Chemical Analysis (ESCA), is a non-destructive, quantitative spectroscopic to provide detailed information about the elemental composition, chemical and electronic state of materials. The fundamental principles of XPS are rooted in the photoelectric effect. XPS involves the irradiation of a material with a beam of X-rays and the subsequent measurement and analysis of the kinetic energy and number of electrons that escape from the top 1-10 nm of the material being analysed. In an XPS experiment, monochromatic X-ray beams are directed towards the sample surface. Commonly,

aluminium Kα or magnesium Kα radiation sources are employed due to their suitable photon energies. The incident X-rays interact with the atoms in the material and cause inner shell electrons to be ejected. This process is governed by the photoelectric effect, which states that when an electron absorbs a quantum of energy (photon), it is excited and subsequently ejected from the atom if the photon energy exceeds the electron's binding energy. The ejected photoelectrons are then analysed using an electron energy analyser. The number and kinetic energy of the photoelectrons are precisely measured. The kinetic energy of the photoelectrons, which is related to the energy of the incident X-rays and the binding energy of the electrons, allows for the identification of the atom from which the electron originated. XPS spectra are obtained by plotting the number of electrons detected (intensity) as a function of their binding energies. The peaks in an XPS spectrum represent the photoelectron signal from atoms in the sample. The positions, areas, and shapes of these peaks provide information on the elemental composition (qualitative analysis), the quantity of each element (quantitative analysis), the chemical state of the elements, and the electronic state of the elements present in the sample. XPS has the advantage of providing surface-sensitive characterization because only the photoelectrons near the surface of a material can escape without losing energy through inelastic collisions with other atoms. This makes XPS an extremely valuable tool in the study of surface chemistry, which is of critical importance in many industrial and technological applications. For the data presented in this thesis a Kratos Axis Supra (Kratos Analytical, Manchester, UK) using a monochromated Al Kα source (225W power). All spectra were recorded without using a charge neutraliser. Survey scans were recorded at a pass energy of 160 eV and the high resolution data at 40 eV with energy steps of 0.1 eV.

2.1.3 Scanning Electron Microscopy (SEM)

Scanning electron microscopy (SEM) is a non-destructive microscopy technique used to analyse the surface topography of a material. SEM as a method has benefits over typical optical microscopes such as the ability to take images up to 100,000X magnification at high resolution compared to the maximum 1,000X magnification seen in an optical microscope. SEM offers a larger depth of field at high

magnifications compared to an optical microscope owing to the nature of its detection mechanism, thus it produces higher quality images with most of the sample surface in focus regardless of the surface roughness, while the optical microscope relies on the sample being smooth at high magnification for the image to be in focus. Two analytical machines were chosen, one for lower magnifications and the other for higher. A Zeiss EVO SEM with an accelerating voltage of 20 keV, a working distance of 8.5 mm using secondary electron detector was used for the lower magnifications. The other was a JEOL 7800F FEG-SEM with an accelerating voltage of 5 keV, working distance of 5 mm and a secondary electron detector which was used for the higher magnifications.

2.2 Battery Fabrication

After the materials characterisation, the powders were then used to create electrodes for electrochemical characterisation. This process involves taking the powders, adding a binder and solvent to create a slurry (ink paste) which is then doctor bladed onto aluminium foil and then cut to size for electrode assembly in coin cells.

2.2.1 Synthesising hard carbon and sodium rhodizonate active materials

The synthesis conditions to make the hard carbon is explained below. There are two in total

There are three stages to the creating the hard carbon active materials – drying, dehydration and pyrolysation.

1. 1 g of sucrose (Sigma Aldrich) is dried at 80 °C for 24 hours using a Carbolite convection oven
2. After 24 hours, the temperature is increased to 180 °C for another 24 hours to dehydrate
3. Pyrolysation of the dehydrated material at chosen ramp rates (discussed in hard carbon chapter) up to 1100 °C using a Carbolite tube furnace, with an Argon flow rate of 1 litre/min through the tube furnace.

4. After pyrolysis is completed the resultant hard carbon is allowed to cool to 20 degrees.

The synthesis conditions for making the hard carbon graphene oxide is explained below:

Additional steps are required compared to the previous hard carbons

1. 10 ml of graphene oxide solution (Graphenea Graphene Oxide water dispersion 0.4 wt% concentration) is sonicated in 40 ml of de-ionised water for 4 hours
2. 3.2 g of sucrose is dissolved into the graphene oxide solution with an additional 50 ml of de-ionised water and sonication is continued for another 4 hours`.
3. The solution is dried at 80 °C for 24 hours using a Carbolite convection oven
4. After 24 hours, the temperature is increased to 180 °C for another 24 hours to dehydrate
5. Pyrolysation of the dehydrated material at chosen ramp rates (discussed in hard carbon chapter) up to 1100 °C using a Carbolite tube furnace, with an Argon flow rate of 1 litre/min through the tube furnace.
6. After pyrolysis is completed the resultant hard carbon is allowed to cool to 20 degrees.

The synthesis of sodium rhodizonates are shown below. There are three in total

The macro (MR) rhodizonate does not undergo any synthesis before slurry preparation.

The nano (NR) rhodizonate synthesis conditions are:

1. 50 mg (2 mg/ml) or 100 mg (4 mg/ml) of sodium rhodizonate (Sigma Aldrich) is dissolved in 25ml of deionized water in a conical flask and heated in a silicon oil bath until the solution reaches 80 °C
2. Once the solution is at 80 °C 250 ml of ethanol absolut. (Sigma Aldrich) is poured into the conical flask

3. The resulting solution is cooled to room temperature, centrifuged for an hour (3 x 20 minutes, with the resultant solution removed and replaced after each 20 minute stage)
4. Once centrifuged the remaining solution is removed and the resulting powder is placed in a vacuum oven (Pi-Kem) for 24 hours at 60 °C

The nano with rGO (NRR) rhodizonate synthesis conditions are:

1. 25mg of rGO is placed in 25 ml of deionised water and an ultrasonicator probe (Bandelin Sonopuls Ultrasonic Probe) applies 50kJ energy for 1 hour (40% power, 2 seconds on/2 seconds off)
2. 50 mg (2 mg/ml) or 100 mg (4 mg/ml) sodium rhodizonate (Sigma Aldrich) is dissolved into 25 ml of deionized water in a conical flask and heated in a silicon oil bath until the solution reaches 80 °C
3. Once the solution is at 80 °C 250 ml of ethanol absolut. (Signma Aldrich) is poured into the conical flask
4. The resulting solution is cooled to room temperature and passed through a membrane filter (MF-Millipore Membrane filter 8 µm pore) placed inside a Büchner funnel using vacuum filtration
5. The membrane is placed in a vacuum oven (Pi-Kem) for 24 hours at 60 °C

All the resultant powders are then used in slurry preparation as discussed below.

2.2.2 Slurry Preparation

A similar preparation route was used for all electrodes. The electrodes were prepared from a slurry (ink paste) which included the active material, a binder to hold the material together with a conductive carbon material and then finally a suitable dispersal solvent. The casted slurries followed a ratio of either 8:1:1 or 7:2:1. The first binder that was used was sodium carboxymethyl cellulose (CMC) (Sigma Aldrich), a mixture deionised water and ethanol in 1:1 in volume was used as solvent. The other binder used was Polytetrafluoroethylene (PTFE) (Sigma Aldrich) and N-Methyl-2-pyrrolidone (NMP) (anhydrous 99.5%, Sigma Aldrich) as the solvent. The conductive carbon additive used was Carbon black Super P (Imerys, Timcal Ltd.) To mix the materials together to make the slurry a Fritsch Pulveristte 23 mini ball-miller was chosen. Figure 2.1 below shows the Pulveristte used.

Figure 2.1: Pulverisette mini ball mill

The hard carbons followed the 8:1:1 ratio as discussed for the synthesis of the slurries to be casted.

For both hard carbon (HC) and the hard carbon graphene oxide (HCGO) followed:

8:1:1 ratio

100 mg of HC/HCGO material,

12.5 mg Carbon black Super P (Imerys, Timcal Ltd.),

12.5 mg CMC (Sigma Aldrich) with 0.8 ml deionized water and 0.2ml ethanol absolut. (Sigma Aldrich)

This solution was then placed in the Pulverisette ball mill as shown above in figure 2.1 for 20 minutes at 30 Hz and then cast as discussed below.

For the rhodizonates a 7:2:1 ratio as discussed above was used.

7:2:1

100 mg MR/NR/NRR material

28.57 mg PTFE powder (Sigma Aldrich)

14.28 mg Carbon black Super P (Imerys, Timcal Ltd.),

With 1 ml of NMP (Sigma Aldrich)

The solutions were then placed in the Pulverisette ball mill as shown above in figure 2.1 for 20 minutes at 50 Hz and then cast as discussed below.

2.2.3 Electrode Preparation

The resultant slurry was then cast onto aluminium foil (15 m thickness, MTI) using a doctor blade technique at a thickness of 200 µm. The resultant cast was dried in a vacuum oven (MTI) at 60 °C. The cast was cut to discs of 12.5 mm diameter and placed under a Schlenk line overnight before being transferred into an Argon-filled glovebox (MBraun) (H_2O < 1 ppm, O_2< 1 ppm) for coin cell assembly.

Figure 2.2: Casting of slurry onto Al foil using doctor blade at thickness of 200 µm

2.2.4 Electrolyte Preparation

Multiple electrolytes can be used in battery cycling, the choice of electrolyte is chosen dependant on the active material and binder used during slurry preparation. Initially, a variety of electrolytes and solvents were tested, sodium hexafluorophosphate ($NaPF_6$) (FluoroChem) and sodium perchlorate ($NaClO_4$) (anhydrous, Alfa Aesar). Multiple solvents were used with these salts which were ethylene carbonate (EC) (99%, anhydrous, Sigma Aldrich), propylene carbonate (PC) (Sigma Aldrich), tetraglyme (TEG) (Sigma Aldrich) and diglyme (G2) (Acros Organic). The final chosen electrolyte/solvent combination was $NaPF_6$/G2 due to the compatibility of the electrolyte/solvent with both hard carbon and rhodizonate to enable full-cells to be assembled. All electrolytes used were at a concentration of 1 mol/L with 100 µL used per coin cell.

2.2.5 Coin cell assembly

Commonly assembled coin cells used for electrochemical analysis are half-cells, these refer to a configuration where a reference and counter electrode is sodium metal; this then offers a surplus of sodium allowing the study of the properties of the working electrode. Most coin cells assembled for this work are half-cells. However, one of the chapters in this work explores the assembly of a full-cell, this is a configuration where both an anode and cathode are assembled with one of the electrodes being pre-sodiated beforehand. In this work the anode was assembled as a half-cell cycled multiple times and with cycling ending with the anode being in a sodiated state, sodium ions within the structure to be the source of sodium for the full-cell.

The coin cells used for assembly were CR2032 (20 mm diameter and 3.2 mm thickness), these were then used for the electrochemical testing of the electrodes. For the assembly of the coin cells, two circular metal cases (SS304) that contain two circular electrodes, two spacers and a spring were crimped together. For the half-cells one of the two circular electrodes was a disc of sodium metal (Sigma Aldrich). To separate the sodium disc and electrode a separate was chosen being Celgard trilayer 2325 (PP/PE/PP, thickness 25 mm). The supplier of the coin cell parts above, was Pi-kem Ltd.

2.3 Electrochemical Analysis

Battery materials are fundamentally based on a variety of parameters, these include chare/discharge capacities, number of cycles and the average voltage. Energy and power levels can then be calculated from these parameters. Further tests then allow to storage mechanisms to be scrutinised including the intercalation reactions throughout the cycling life.

There are two commonly used techniques to analyse the electrochemical performance of cells, these are galvanostatic cycling (GC) and cyclic voltammetry (CV). Galvanostatic cycling allows the storage capacity and voltage profiles to be recorded

which then allows the storage mechanisms to be indicated. Cyclic voltammetry analyses these storage mechanisms with their working potentials.

2.3.1 Galvanostatic Cycling (GC)

Galvanostatic cycling allows the calculation of the input/output capacities within a specified voltage window, using a chosen number of cycles. GC involves applying a fixed current that is positive during charging and negative when discharging, the change in voltage is then recorded. An upper and lower voltage is chosen as voltage cut-offs which is a chosen voltage window. This then allows multiple cells to be analysed within the same voltage range. A time limit can also be applied if the upper or lower voltages are not met. The current applied is expressed as mA/g, by calculating the theoretical capacity of the electrode material, a C-rate can then be calculated. The C-rate is used to describe the full discharge time, 1C for example, it a complete discharge which takes 1 hour, C/10 is a full discharge over 10 hours and 10C is completed in 6 minutes. The electrochemical reactions of the intercalation/de-intercalation of the ions can be detected through the voltage plateaus that occur during testing. The GC testing was analysed on a BatSMALL 8 channels galvanostat (Astrol Electronic AG, Switzerland)

Preliminary testing used various current density mA g^{-1} cycling rates for both the hard carbons and rhodizonate half-cells, the final current densities chosen were run at a C rate of C/2 which is 150 mA g^{-1} for the hard carbons and 100 mA g^{-1} for the rhodizonate half-cells. This faster C rate was chosen to allow more cycles to be completed in a shorter time frame to ensure every half-cell completed a minimum 100 cycles for a comparison between every half-cell. Furthermore, various voltage ranges were used for hard carbon and rhodizonate respectively, but they were then chosen to be 2-0.01 V for hard carbon and 3.1-1.0 V for the rhodizonate half-cells; this again allowed for a more consistent approach and allow a comparison to be made between all half-cells.

2.3.2 Cyclic Voltammetry (CV)

Cyclic Voltammetry is an effective technique that allows the mechanism during the charge/discharge cycles to be investigated, over several cycles a level of potential is given, and this is then monitored throughout to see any shifts in the potential occurs. CV tests linearly increase/decrease the voltage within a set voltage window and the change in current is recorded. If required, current vs voltage graphs can be displayed for multiple cycles.

The first step usually involves a forward scan from the starting potential rising to the high potential with a positive anodic current being detected which is an indication of oxidation, this directly corresponds to a charging step observed during galvanostatic cycling test. For the reverse scan which starts from the high potential down to the set lower potential a negative cathodic current is observed. This is an indication of reduction, similarly this directly corresponds to a discharge step during galvanostatic cycling. Thus, the observed peaks seen in CV scans correspond to the voltage plateaus that are seen during galvanostatic cycling tests. CV tests are undertaken using half cells vs sodium, the working electrode is the positive electrode, and the reference electrode is the negative electrode. All the CV measurements were obtained using a VMP3 potentiostat (Bio-logic Science Instruments, France). All CV scans were run at 10 mV/s across the voltage ranges discussed in the previous subchapter 2.3.1.

Part 3

The Doping of Graphene Oxide into Hard Carbon

3.1 Introduction

This chapter explores hard carbon as an electrode for sodium-ion batteries. The focus will be on the synthesis of the hard carbon; specifically looking into the manipulation of the pyrolysis conditions during the synthesis, targeting a temperature range where there is a rapid change in mass to evaluate whether slowing the heating at this point affects the outcome. A promising additive reported in the synthesis of hard carbon is graphene oxide, which limits the inherent foaming of the sucrose during heating and provides a slower change in mass over the 200 to 400°C range, this appears to have positive implications for the capacity of the material. Therefore, the use of graphene oxide will be investigated in terms of any potential effect on the hard carbon material as well as the interplay with the pyrolysis conditions

Hard carbon is synthesised using a carbohydrate precursor, the chosen carbohydrate in this investigation is sucrose. The sucrose is firstly dried, dehydrated and then pyrolysed with the resultant product being hard carbon. The graphene oxide will be included from the first step. Specific information regarding the steps involved have been previously discussed in Chapter 2 and are discussed further in this chapter.

The dehydration stage is key to the synthesis of hard carbon as reported by *Luo et al.* during this stage the sucrose precursor expands rapidly with foaming occurring. The graphene oxide hinders this foaming; it also helps expand the burn-off of the sucrose to a wider temperature range during the pyrolysis.

Thus, due to the foaming of sucrose and the potential benefits including graphene oxide throughout, multiple variations of hard carbon and hard carbon w/ graphene oxide will be synthesised. These will focus on the pyrolysis conditions, including the heating ramp rates and holding temperatures. Both a hard carbon (HC) and a hard carbon w/ graphene oxide (HCGO) equivalent will be synthesised, characterised, and then cast as an electrode to be assembled into half-cells for electrochemical characterisation. In total, there will be three variants of each HC and HCGO, the first will use an unspecified ramp rate during pyrolysis, with the second and third having different controlled ramp rates. The resultant materials after pyrolysation will be characterised through XRD, XPS and SEM for comparison between each variant.

Electrochemical characterisation will use GC (galvanostatic cycling) supplemented by CV (cyclic voltammetry).

3.2 Synthesis of hard carbon and hard carbon w/ graphene oxide

Three variants of hard carbon (HC) with the hard carbon w/ graphene oxide equivalent were synthesised. The charts below show the synthesis methods that were used. Drying and dehydration methods were common to all HC syntheses, but the pyrolysis rates were varied. Hard carbon with graphene oxide (HCGO) required additional pre-pyrolysis stages, common to all syntheses, but used the same pyrolysis rates as the HC cells, with the equipment and methods used are further detailed in Chapter 2.

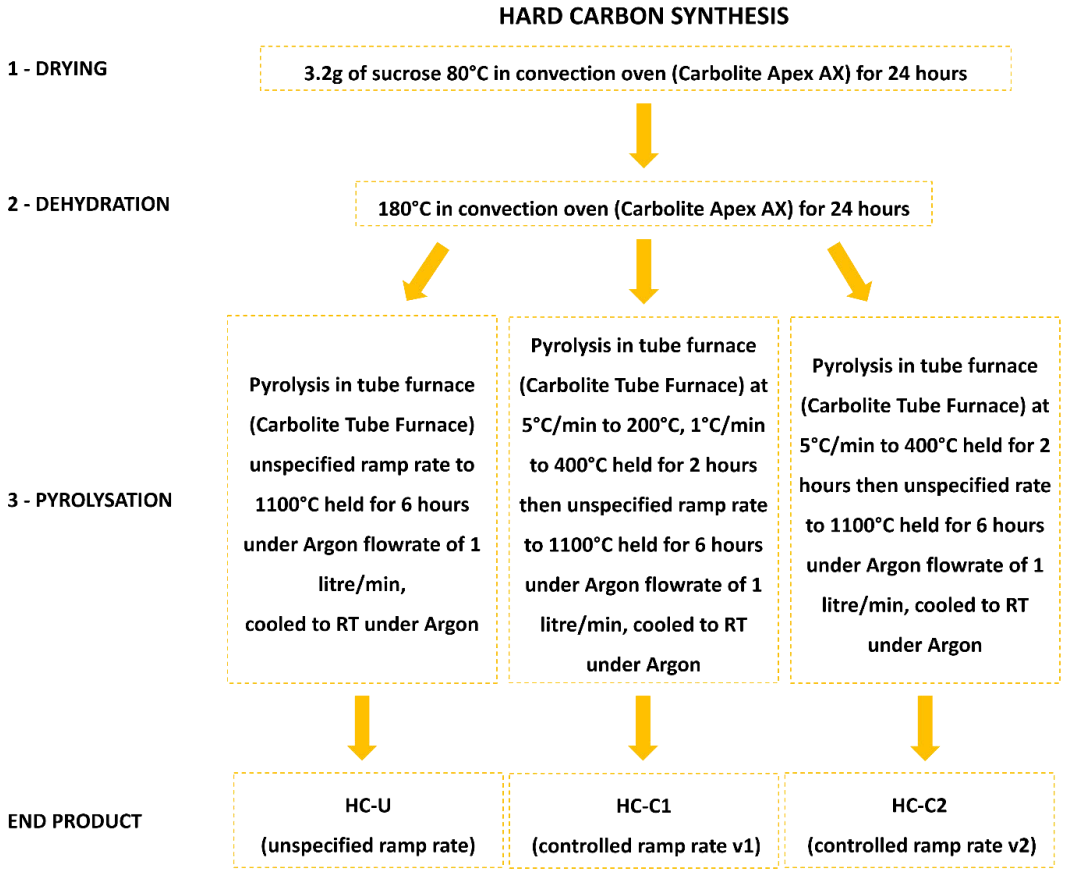

Figure 3.1: Flowchart showing the synthesis of the three HC variants

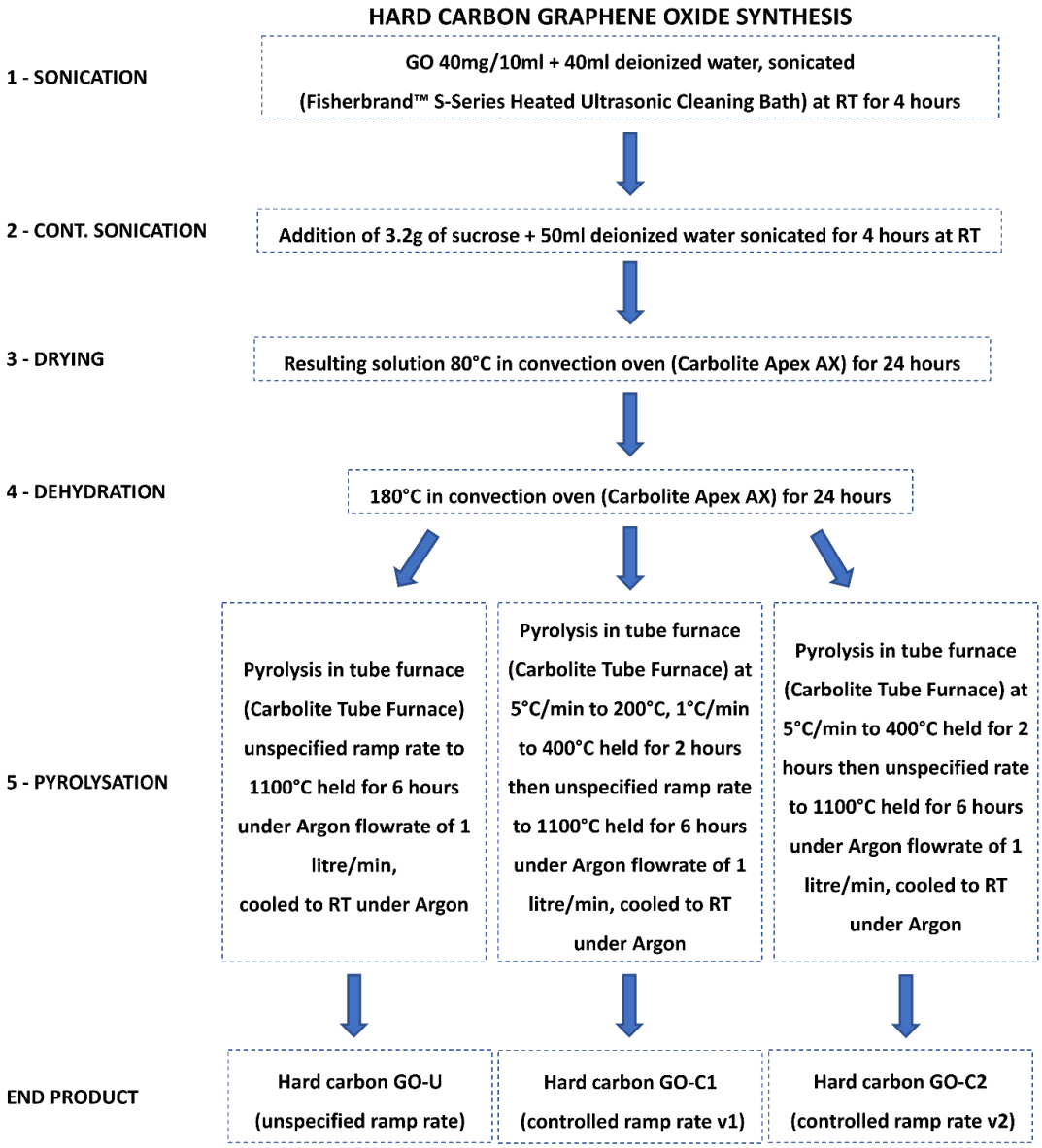

Figure 3.2: Flowchart showing the synthesis of the three HCGO variants

Both figures 3.1 and 3.2 above show the synthesis methods for the HC and HCGO respectively. As previously raised, three variants are synthesised. For a given material (HC or HCGO) the pyrolysis step was altered, focusing on the ramp rates and holding temperatures/times. Each variant has a specific name dependent on the temperature ramping protocol, being -U, -C1, -C2 (HC-U is hard carbon that uses an unspecified

ramp rate and HCGO-C1 is hard carbon w/ graphene oxide that follows the first controlled pyrolysis method for example).

The key differences focus on the lower temperature ranges of the pyrolysis step. For comparison, with the unspecified -U variants, it was timed that it takes ~ 8 minutes to reach 200°C, ~14 minutes to 400°C and ~70 minutes to reach 1100°C. This then allows the pyrolysis rates to be compared. The other key difference between the two types of hard carbon; is that for the HCGO variants, there is sonication step before drying. This is to accommodate the inclusion of the GO; through the dispersal of the GO in water with the sucrose being dissolved part way through. The HC variants use sucrose powder without a sonication stage in water.

3.3 Characterisation of HC and HCGO powders

All variants of the HC and HCGO powders underwent various characterisation methods. These were XRD, XPS and SEM. XRD was chosen to determine the crystal structure of the powders. XPS to give an elemental analysis of the surface chemistry, and SEM to show the morphology and topography of the powders. Note that equipment details and operating parameters can be found in Chapter 2

3.3.1 XRD analysis

XRD analysis was undertaken on all variant powders after synthesisation. As previously stated, XRD allows the analysis and comparison of the crystal structures of the powders allowing for comparison between them. Three graphs will be shown below showing the results. Figure 3.3 showing HC-U, -C1 and -C2. Figure 3.4 HCGO-U, -C1 and -C2. Figure 3.5 HC-U, HCGO-U, and comparison to literature

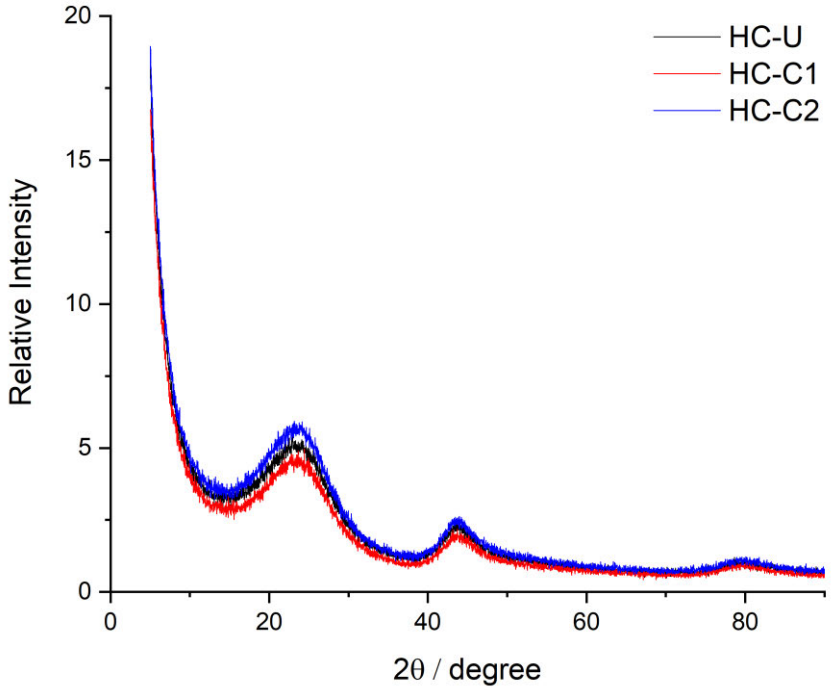

Figure 3.3: XRD overlay of HC-U, HC-C1 and HC-C2

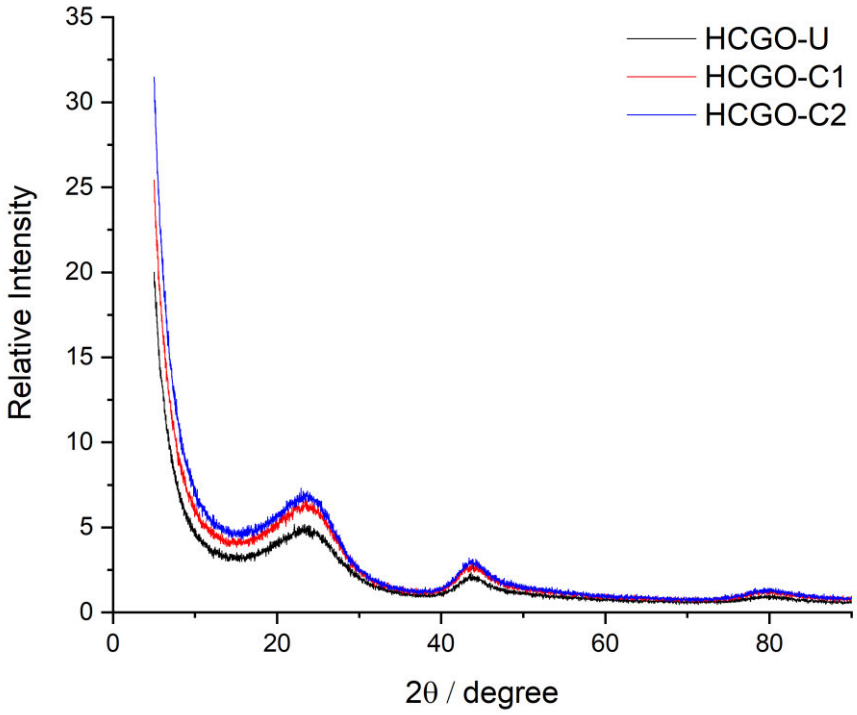

Figure 3.4: XRD overlay of HCGO-U, HCGO-C1 and HCGO-C2

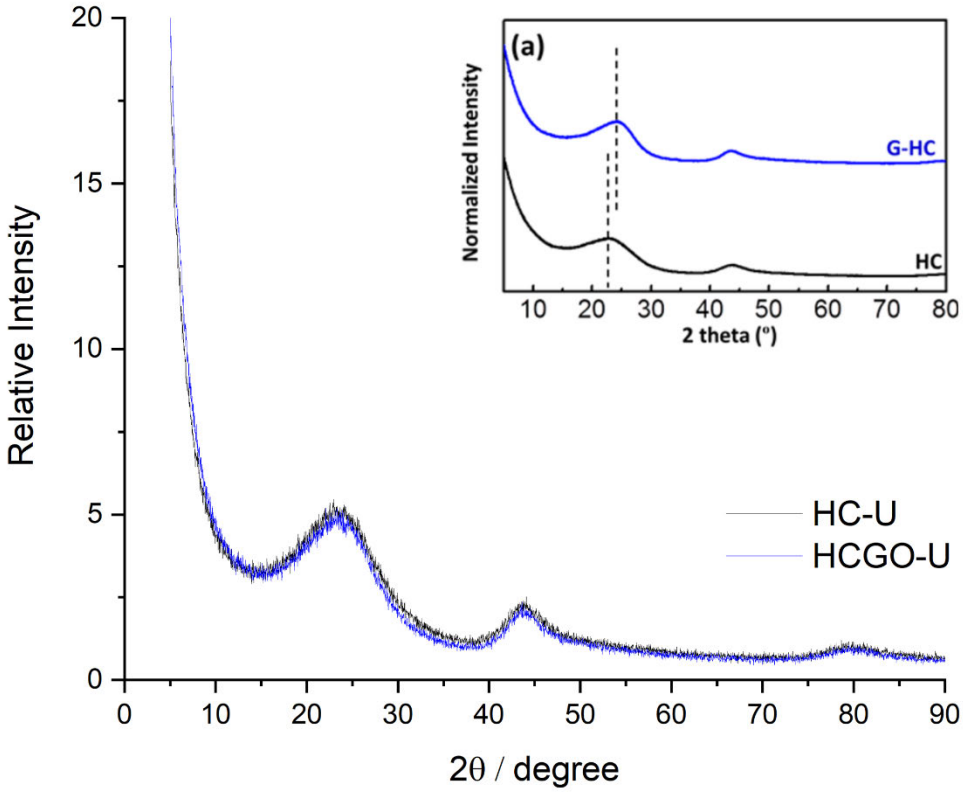

Figure 3.5: XRD overlay of HC-U and HCGO-U (W. Luo et al., 2015)

As previously discussed in Chapter 1, hard carbons commonly have a disordered structure; with randomly orientated and loosely stacked nanosheets. These are embedded into amorphous regions with disordered pores and defects. As shown, the amorphous carbon structures can be similarly observed in all variants of HC and HCGO. These as shown by the three amorphous halos at 2θ ~23°, 2θ ~ 44° and 2θ at ~80°. These show the (002), (100) and (110) planes/stacking axis of the carbons respectively. These planes can be seen throughout, with both (002) and (100) also being observed in the XRD analysis by *Luo et al.* which is included in figure 3.5 and ubiquitous in the literature. When comparing each HC and HCGO variant against one other and the influence of changing the ramp rate conditions during pyrolysis, no differences can be seen between them.

It is worth noting that with the disordered structure of hard carbons, this can lead to complications when characterising through XRD analysis as raised by *Mittal et al.*.

The atomic structures of carbons have dimensions of coherently scattered domains that are usually <20 Å, which results in limitations of Bragg scattering and broad reflections then occur. However, if high quality data is collected and becomes distinguishable from the background, the reflections can then sometimes be used to determine the stacking axis and d spacings as shown above.

3.3.2 XPS analysis

XPS analysis was carried out on all variants. Whilst XRD analysis focuses on the crystallinity of a sample; XPS examines the elemental composition of the surface; by showing the elements on the surface it can help validate the pyrolysis step with the removal of oxygen and hydrogen during the pyrolysis. XPS focuses on counts per second (CPS) vs. the binding energy (eV), essentially the number of electrons that are detected at a specific binding energy from an elemental bond. All HC and HCGO variants were analysed using XPS, as shown in figures 3.6 and 3.7 below.

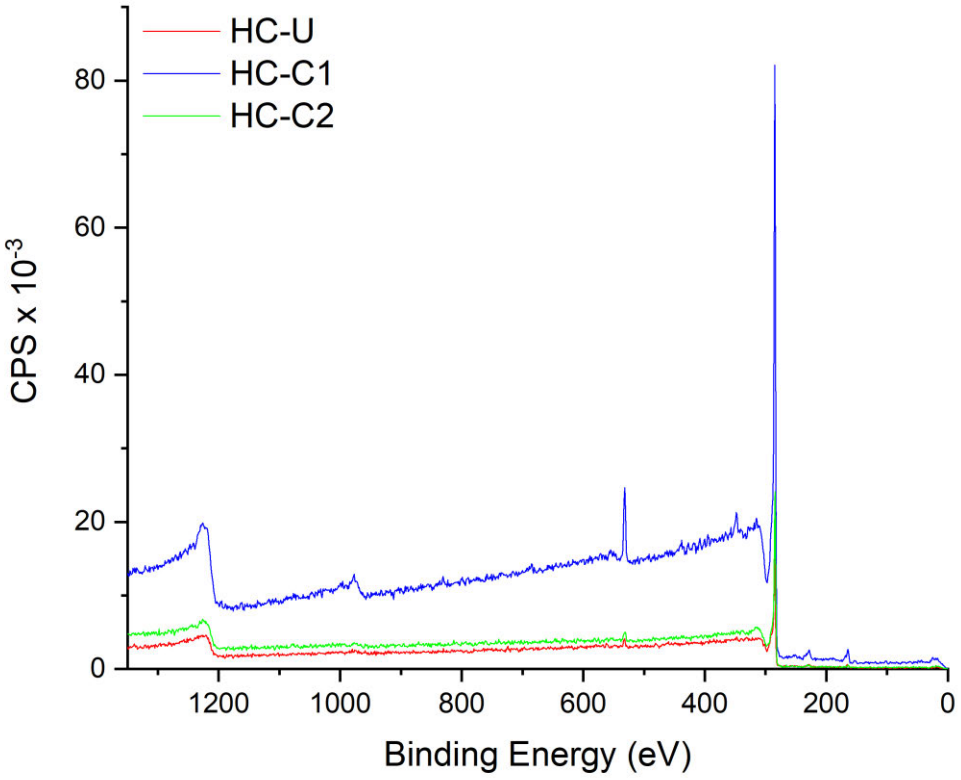

Figure 3.6: Overlay of XPS analysis on HC-U, -C1 and -C2

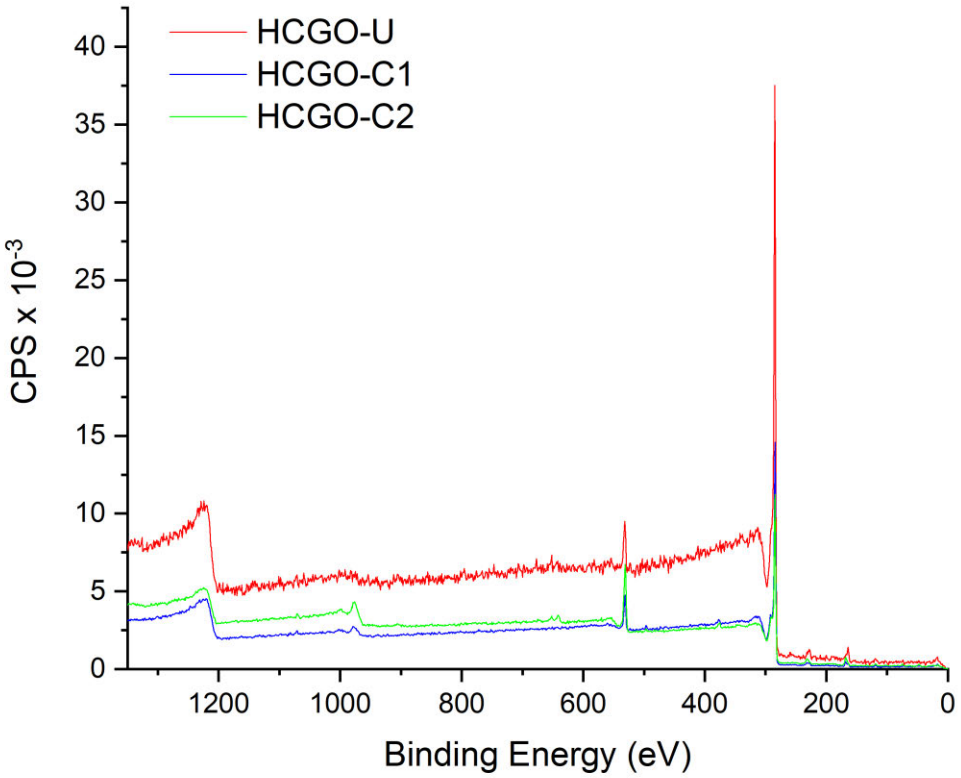

Figure 3.7: Overlay of XPS analysis on HCGO-U, -C1, -C2

Both sets of graphs above show similar data in terms of the characteristic binding energies. Each peak corresponds to a specific bond that helps determine what is present on the surface of the material. The biggest peak intensity as seen throughout is at ~284.8 eV, this is a C 1s peak denoted to carbon, specifically a C-C bond and at ~284.5 eV a C=C bond. Other peaks are also observed, ~531 eV an O 1s oxygen peak and at ~1224 eV a C KLL carbon peak. With all variants having these specific peaks they are essentially chemically the same on the surface. These peaks validate that during the pyrolysis stage that the vast majority of all the other elements within the sucrose precursor has been removed leaving a predominantly carbon structure with C-C and C=C bonds. It is not unusual to see an O 1s oxygen peak on the surface of the sample as it has been exposed to air after the pyrolysation had been completed.

3.3.3 SEM analysis

The third characterisation technique used was SEM analysis. This was used to look at the pyrolyzed powder morphology and to see if there were any differences that could be observed between the different pyrolysis methods in figure 3.8-11 below.

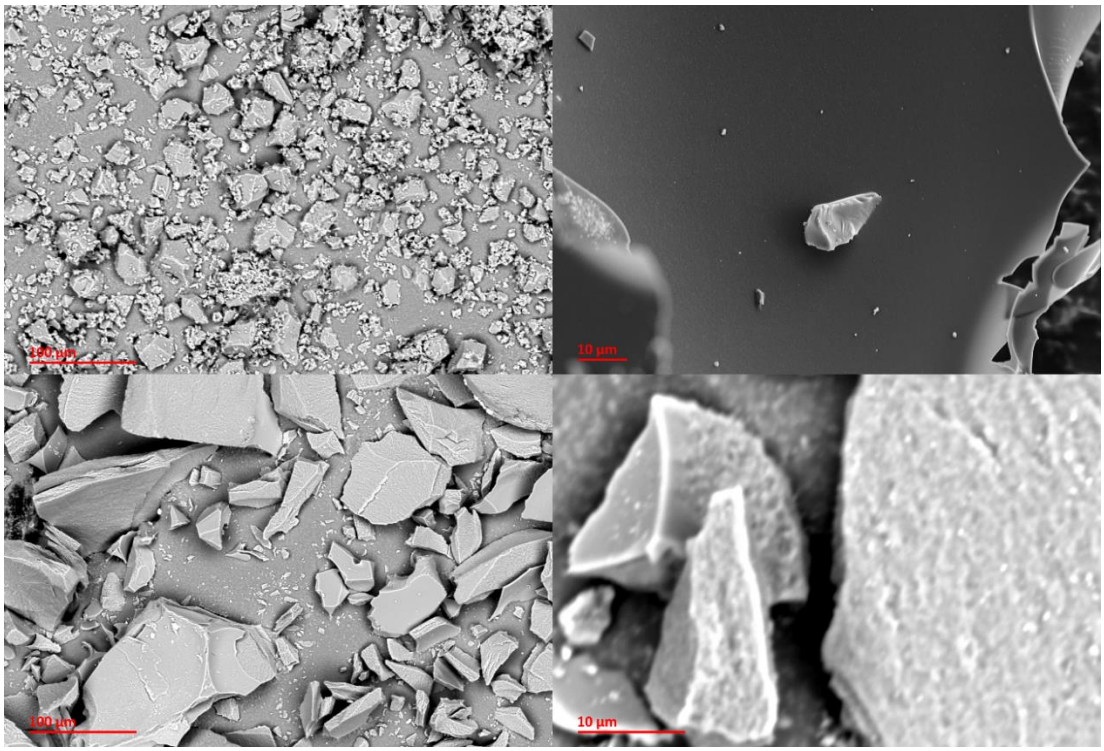

Figure 3.8: SEM images of hard HC-U (top left, top right) and HCGO-U (bottom left, bottom right)

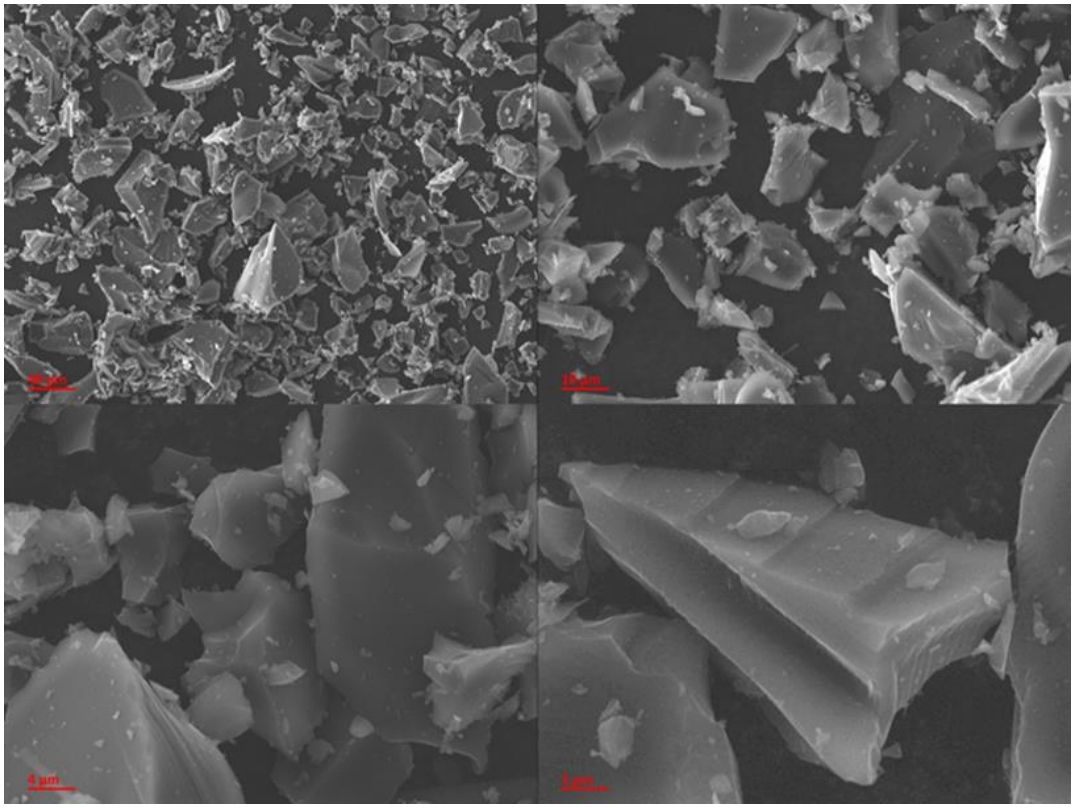

Figure 3.9: SEM analysis of HC-C2 at a range of magnifications

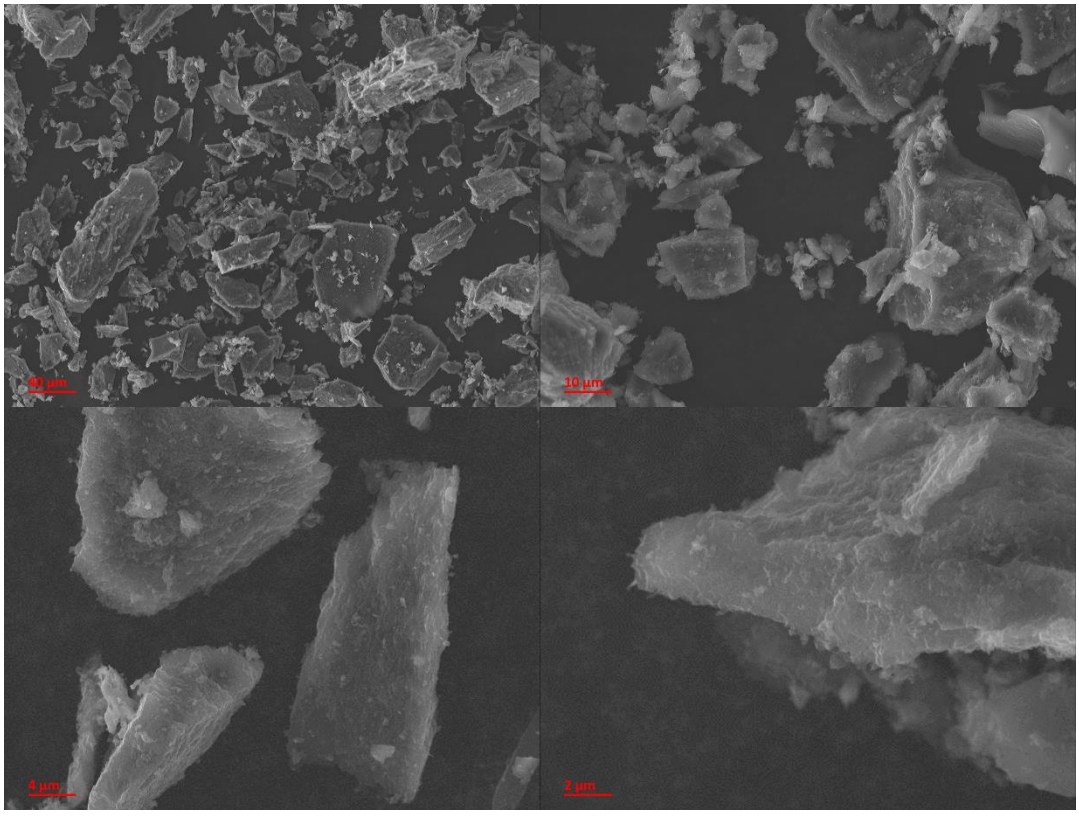

Figure 3.10: SEM images of HCGO-C2 at a range of magnifications

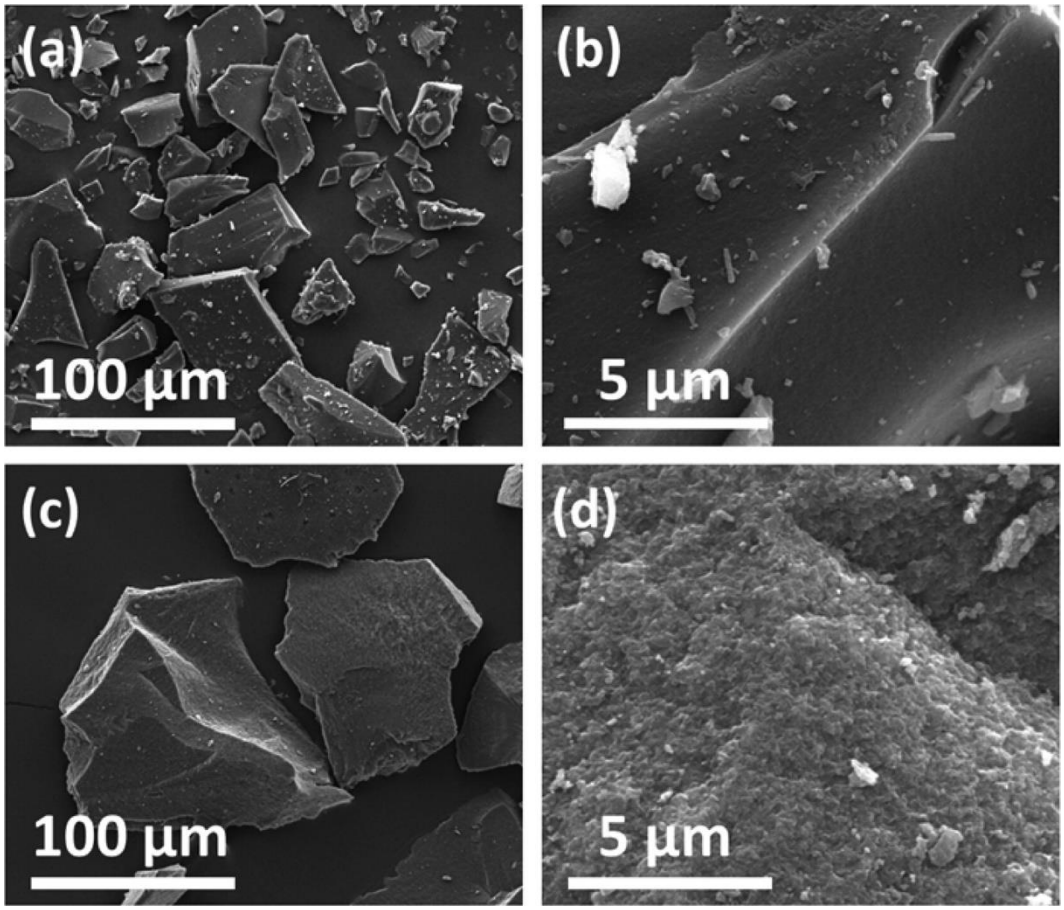

Figure 3:11: Literature SEM images of HC (a,b) and HCGO (c,d) (W. Luo et al., 2015)

SEM analysis was undertaken on HC-U and HCGO-U as seen in figure 3.8, HC-C2 in figure 3.9, HCGO-C2 in figure 3.10 and reference to literature SEM HC and HCGO (unknown ramp rate as no information given) by *Luo et al.*.

For the -U variants as shown in figure 3.8, differences can be seen between the HC-U and HCGO-U, the HC-U has particles that are generally similar in shape and size, with the majority having a length of less than 50 µm with smaller particles less than 10 µm apart too. All the particles have smooth surfaces. The HCGO-U, however, has much larger particles with the majority having a length of over 100 µm, similarly to HC-U there are smaller particles too. These have a similar length to the smaller particles observed with the HC-U which have lengths of ~10 µm. The surfaces of HCGO-U are unlike those of HC-U, having an uneven and rougher surface.

Figures 3.9 and 3.10 show the images for HC-C2 and HCGO-C2 respectively. The results are like what was observed in figure 3.8 with both -Us. Similarly, to the HC-U

results, the HC-C2 images show smooth surfaces and again particle sizes of less than 50 µm. These are then covered with smaller particles less than 10 µm. The same can be seen with both the HCGO-U and HCGO-C2 respectively, as both have larger particles greater than 100 µm with the surface of both being uneven and more rugged.

When comparing to the literature images in figure 3.11, *Luo et al.* show similar observations as seen throughout, in figures 3.8-10. The HC has a smoother surfaces with the larger set of particles being smaller than the larger set of HCGO ones (less than 100 µm vs. greater than 100 µm). The HC has a smaller range of particle sizes of the two sets of sizes observed in all. The results from the SEM analysis are the same as the literature images from *Luo et al.* for both HCs and HCGOs. It is evident from both sets of data that GO has an impact on the morphology and the particle size. Whilst there are clear differences in gross morphology, there are no apparent differences that can be seen with XRD and XPS.

3.4 Electrode Development and Binder/Electrolyte Optimisation

Electrochemical analysis was also undertaken on the hard carbon and hard carbon w/ graphene oxide using sodium metal half-cells. For this, the hard carbon powders were made into a slurry and cast onto aluminium foil. Once cut to size half-cells were made allowing the electrochemical characterisation to begin. Details on the steps involved, chemicals and equipment used are shown in detail in Chapter 2. The data presented in this chapter used common binder and electrolyte systems for all cells but there were multiple preliminary tests that were undertaken to test, refine and optimise the development of and the end results for the hard carbons. Multiple combinations of binders/solvents/electrolytes were explored. The first key component that was explored was the choice of binder and solvents to use. This is added during the fabrication of the slurry. Multiple binders were explored, including two types of PVDF. These were PVDF-HFP and 'Kynar', a key difference between these two is the morphology of the PVDF with the Kynar being a powder compared to the PVDF-HFP that was pellet based. A third binder was chosen, CMC (Carboxymethyl cellulose). All three options were explored. Each binder also then required a solvent to dissolve the binder. For the 2 PVDF binders, NMP was the solvent chosen. As CMC is water soluble, water was used as the solvent. This combination has additional benefits that are worth noting, specifically environmental benefits. NMP is a polar solvent it has many functional benefits as it offers a very high solvency for several important and long-established binders used in electrodes with a high boiling and low freezing point. However, it is classed as a hazardous material to the environment and to humans. It is a combustible liquid, causes skin and eye irritation and a potential carcinogen. Thus, it has multiple hazardous COSHH labels associated with it. This is partially why alternative binder/solvent combinations were chosen and with CMC being water soluble it was explored as a potential option and as previously stated ultimately chosen.

The other key component that was explored was the choice of electrolyte/solvent

combination used during the half-cell assembly. $NaPF_6$ / ethylene carbonate/propylene carbonate (EC/PC) (will be referred to as PF6:ECPC from this point) was the first. The second being $NaPF_6$ / tetra ethylene glycol dimethyl ether (TEGDME) (referred to as PF6:TEG from this point). The third was $NaClO_4$ / ECPC and the final being $NaPF_6$ / diglycol methyl ether (diglyme/G2) (referred to as PF6:G2 from this point). It should be noted that the quality of the results obtained was variable in this preliminary analysis. Several cells did not complete a sufficient number of cycles, and some demonstrated atypical cycling behaviour. This made a comparison of the effect of graphene oxide and pyrolysis conditions unreliable and necessitated the repetition of all the cells in a more systematic fashion. Despite these issues, the investigation was able to identify CMC:Water binder/solvent and PF6:G2 salt/solvent electrolyte as a viable combination to use in systematically studying the half-cells.

3.5 Electrode Overview

This section reports the half-cells used in the study. Half-cells were made for each combination of pyrolysis regime and inclusion or not of graphene oxide. All cells used the same electrolyte and binder (PF6:G2 salt/solvent and CMC/Water binder/solvent) to allows a systematic comparison of the results. Overall, 12 half-cells were assembled, 2 of each variant as shown below in table 3.1. It is also worth mentioning that the current density for galvanostatic cycling of all cells was fixed at 150 mA g^{-1}; this was partly chosen to allow more cycles to be completed and to demonstrate the stability and performance of the cells at a high cycling rate.

Cell Name	HC/HCGO	Pyrolysis conditions	Electrolyte	Binder	Solvent	Current Density (mA g^{-1})
LJ101	HC	Unspecified	PF6:G2	CMC	Water/Ethanol	150
LJ102	HC	Unspecified	PF6:G2	CMC	Water/Ethanol	150
LJ103	HC	Control 2	PF6:G2	CMC	Water/Ethanol	150
LJ104	HC	Control 2	PF6:G2	CMC	Water/Ethanol	150
LJ105	HCGO	Unspecified	PF6:G2	CMC	Water/Ethanol	150
LJ106	HCGO	Unspecified	PF6:G2	CMC	Water/Ethanol	150
LJ107	HCGO	Control 1	PF6:G2	CMC	Water/Ethanol	150
LJ108	HCGO	Control 1	PF6:G2	CMC	Water/Ethanol	150
LJ109	HC	Control 1	PF6:G2	CMC	Water/Ethanol	150
LJ110	HC	Control 1	PF6:G2	CMC	Water/Ethanol	150
LJ111	HCGO	Control 2	PF6:G2	CMC	Water/Ethanol	150
LJ112	HCGO	Control 2	PF6:G2	CMC	Water/Ethanol	150

Table 3.1: An overview of the hard carbon electrodes

After the half-cells had been assembled they underwent electrochemical analysis, the two methods as shown in the remaining sections are galvanostatic cycling (GC) and cyclic voltammetry (CV) the details of how these techniques operate are discussed in the previous methods chapter.

3.6 Galvanostatic Cycling analysis (GC)

The half-cells underwent galvanostatic cycling (GC). For each half-cell two graphs are given. The first is a specific capacity vs. cycle number. This graph shows the sodiation and desodiation capacities and the coulombic efficiencies for each cycle throughout the 100 cycles. The second graph shows a voltage vs. specific capacity which focuses on the sodiation and sodiation profiles as the voltage changes, this graph is important for the first cycle as it is the initial first sodiation into the matrix structure. It also allows comparison of the voltage profiles throughout the cycling life of the half-cells and the natural degradation of the cells throughout the cycling. Over time, it is expected to see the capacity of each half-cell slowly decrease in capacity however it is important to see how the coulombic efficiency changes also. The decrease in capacity over time may not cause a decrease in the coulombic efficiency. All the half-cells follow the same qualitative behaviour, they are all electrochemically similar and differ primarily or only in the magnitude of capacity. It is worth noting that the cells are shown only up to 100 cycles, this is to allow a visual comparison to be drawn, however many cycled for considerably longer.

3.6.1 HC and HCGO - undefined ramp rates (HC-U and HCGO-U)

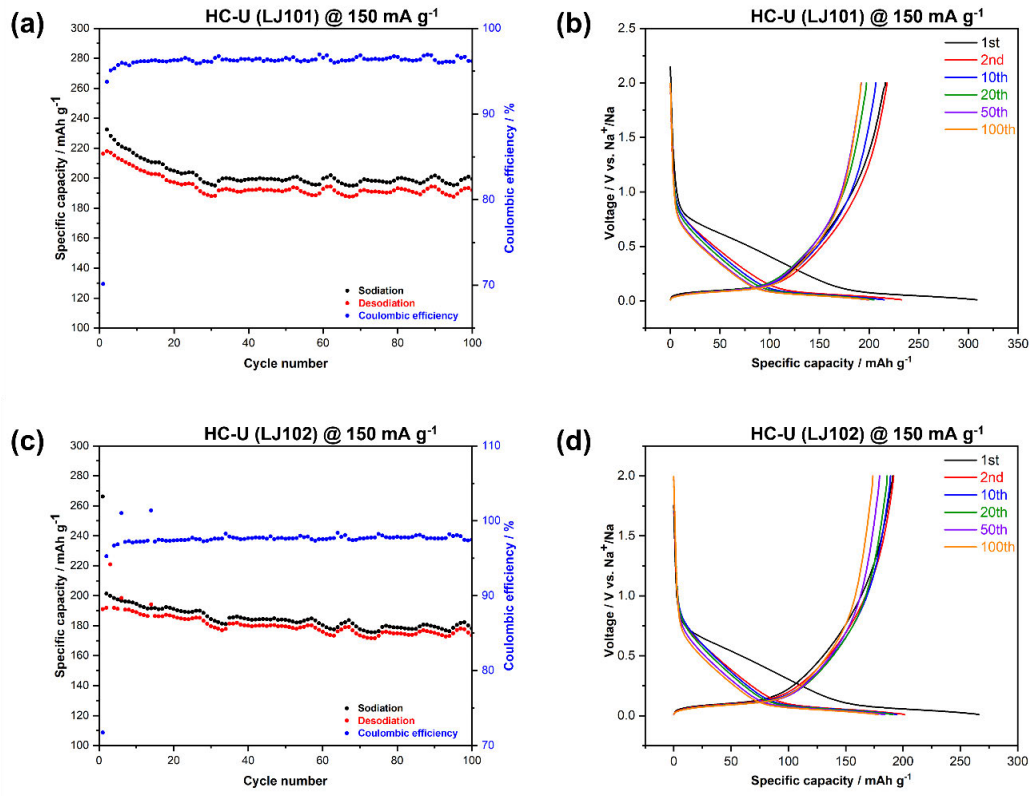

Figure 3.12: HC-U cycling data, undefined ramp rate (LJ101 a+b, LJ102 c+d)

Figure 3.12 above shows the hard carbon cycling data for the hard carbon unspecified ramp rate (HC-U). As shown in the the results table above, both cells have a first cycle capacity of 308 and 266 mAh g^{-1} respectfully. A first cycle loss of 30 and 28% is also seen in both figures b and d. Furthermore, both maintain good long cycling data with capacities of 192 and 174 mAh g^{-1} at the 100^{th} cycle and still both maintaining high coulombic efficiencies of 96 and 97% for LJ101 and LJ102 respectively as shown in graphs a and c.

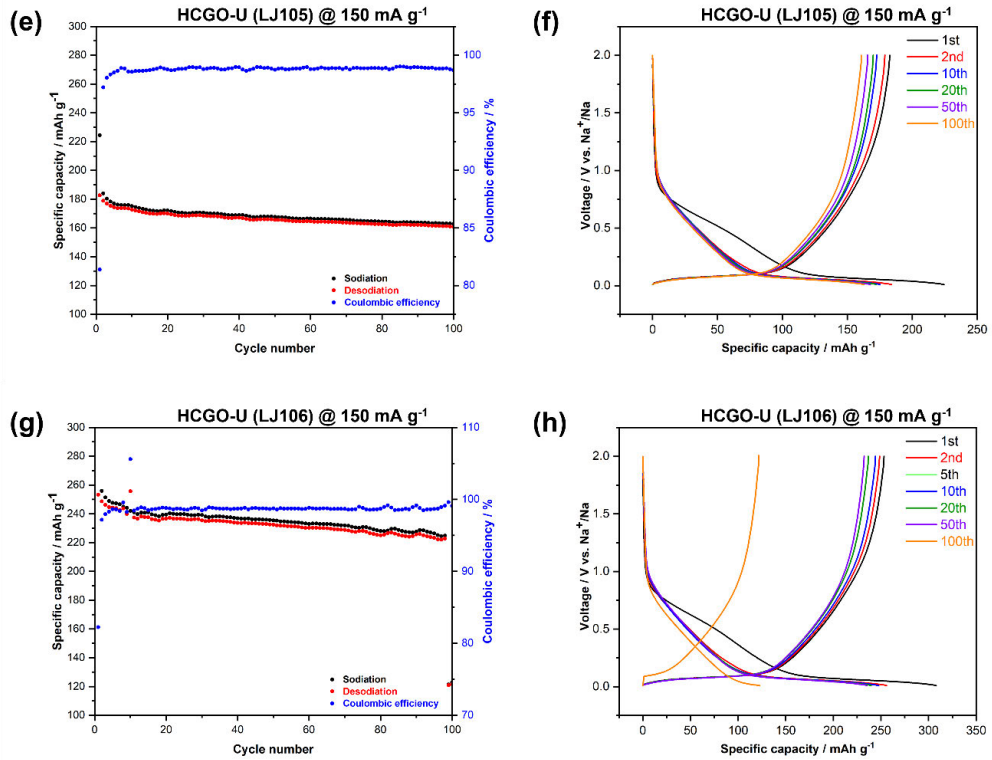

Figure 3.13: HCGO-U cycling data, undefined ramp rate (LJ105 e+f, LJ106 g+h)

Figure 3.13 above shows the hard carbon cycling data for the hard carbon graphene oxide unspecified ramp rate (HCGO-U). As shown in the the results table above, both cells have a first cycle capacity of 224 and 308 mAh g^{-1} respectfully. A first cycle loss of 19 and 18% is also seen in both figures b and d. Furthermore, both maintain good long cycling data with capacities of 160 and 121 mAh g^{-1} at the 100th cycle and still both maintaining high coulombic efficiencies of 99% for both LJ105 and LJ106 respectfully as shown in graphs e and g.

In comparison between the HC-Us and HCGO-Us, both HC-Us have higher capacities at the 100th cycle. However, the HCGO-Us both have lower 1st cycle capacity losses and maintain a slighter higher coulombic efficiency at the 100th cycle. It can also be seen in the specific capacity vs cycle number graphs a and c for the HC-Us and e and g for the HCGO-Us that the HCGO-Us have a more consistent capacity throughout the 100 cycles with minimal fluctuation/less variation in the capacity per each cycle.

The voltage vs specific capacity graphs for both sets of half-cells are both smooth and consistent with visible drop in capacities over time as indicated by the 100th cycle line. Furthermore, as seen in the first discharge cycle for all 4 half-cells, the 1st cycle sodiation line is substantially different from the other cycles. This slower lowering in voltage along with the highest capacity is to be expected as previously discussed; this is the first sodiation into the hard carbon structure which allows the formation of the SEI layer.

3.6.2 HC and HCGO – Controlled ramp rate 1 (HC-C1 and HCGO-C1)

The following graphs show the cycling performance data for HC-C1 and HCGO-C1 cells, both which follow the first controlled ramp rate (C1). In total there are 4 half-cells each having a capacity/cycle number graph and a voltage/capacity graph.

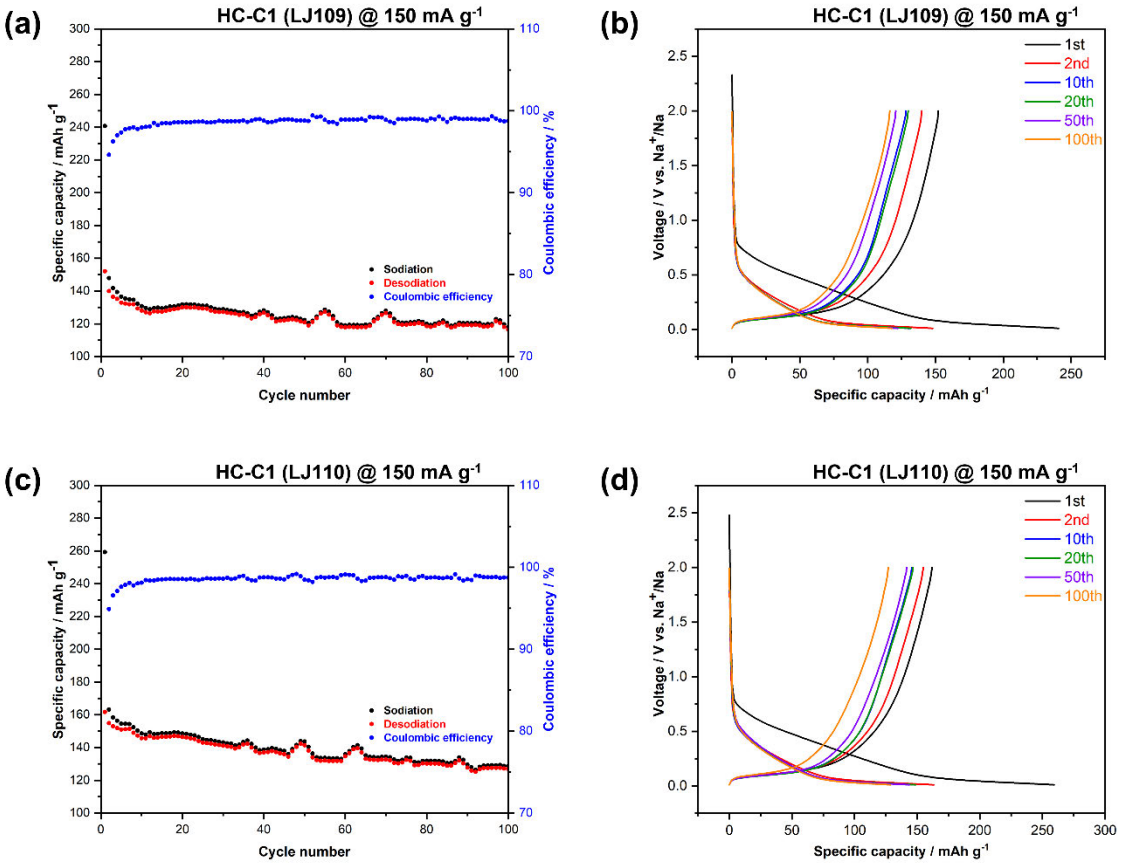

Figure 3.14: HC-C1 cycling, controlled ramp rate 1 LJ109 a+b, LJ110 c+d)

Figure 3.14 above shows the hard carbon cycling data for the hard carbon control ramp rate 1 (HC-C1). As shown in the results table above, both cells have a first cycle capacity of 240 and 259 mAh g^{-1} respectfully. A first cycle loss of 37 and 38% is also seen in both figures b and d. Furthermore, both maintain good long cycling data with capacities of 116 and 127 mAh g^{-1} at the 100th cycle and still both maintaining high coulombic efficiencies of 99 and 99% for LJ101 and LJ102 respectfully as shown in graphs a and c.

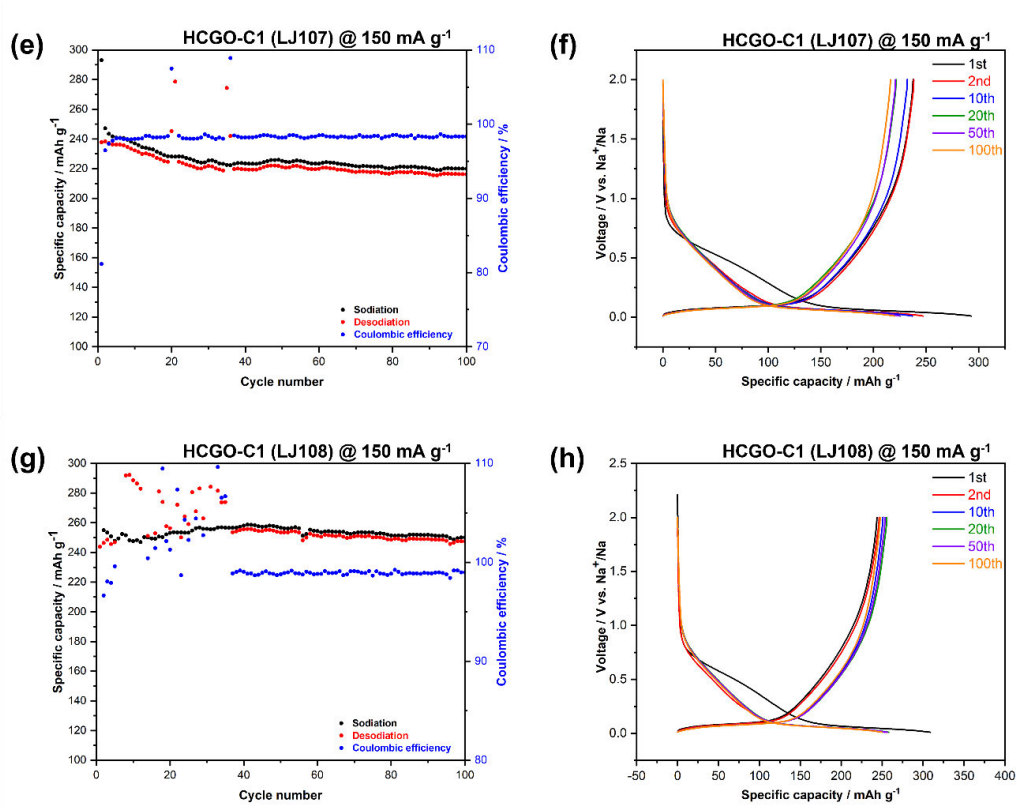

Figure 3.15: HCGO-C1 cycling, controlled ramp rate 1 (LJ107 e+f, LJ108 g+h)

Figure 3.15 above shows the hard carbon cycling data for the hard carbon graphene oxide controlled ramp rate 1 (HCGO-C1). As shown in the the results table above, both cells have a first cycle capacity of 293 and 309 mAh g^{-1} respectfully. A first cycle loss of 19 and 21% is also seen in both figures b and d. Furthermore, both maintain good long cycling data with capacities of 216 and 248 mAh g^{-1} at the 100th cycle and still both maintaining high coulombic efficiencies of 98% and 99% for LJ107 and LJ108 respectfully as shown in graphs a and c.

In comparison between the HC-Us and HCGO-Us, both HC-C1s have lower 1st cycle capacities and 100th cycle capacities with a higher 1st cycle capacity loss compared to the HCGO-C1s. However, both sets of half-cells have nearly identical 100th cycle coulombic efficiencies which shows both sets have good long term cycling. Similarly, to that of the previous HC-U half cells in figure 3.12 the cycling of the HC-C1s is less consistent with the capacities varying more throughout the 100 cycles. One key observation to be raised however, is the half-cell in figure g (HCGO-C1/LJ108) as shown in the specific capacity vs cycle number graph. LJ108 the cell in question is very unstable for the first 36 cycles; it does then stabilise and maintain a high coloumbic efficiency. It is not known why this has occurred. As seen previously in both HC-U and HCGO-U half cells, once again the first cycle intercalation and SEI formation occurs as expected.

3.6.3 HC and HCGO – Controlled ramp rate 2 (HC-C2 and HCGO-C2)

The cycling performance data for HC-C2 and HCGO-C2 cells, both which follow the second controlled ramp rate (C2). In total there are 4 half-cells each having a capacity/cycle number graph and a voltage/capacity graph, shown in figures 3.16 and 3.17

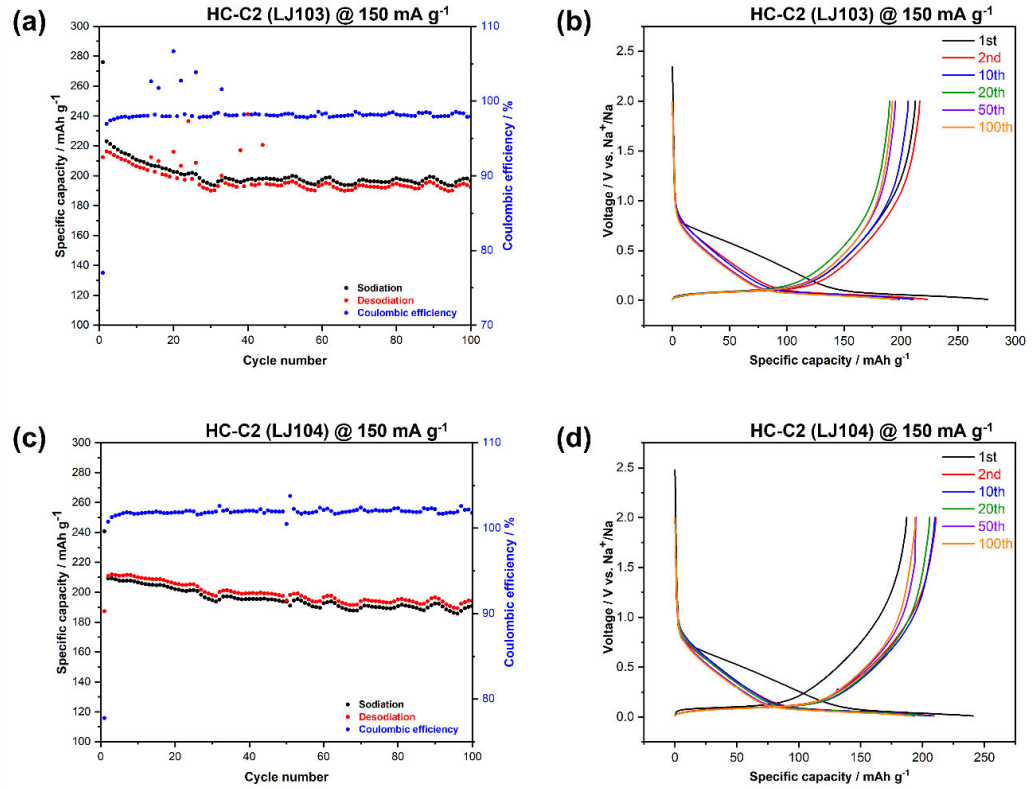

Figure 3.16: HC-C2 cycling, controlled ramp rate 2 (LJ103 a+b, LJ104 c+d)

Figure 3.16 above shows the hard carbon cycling data for the hard carbon control ramp rate 1 (HC-C2). As shown in the results table above, both cells have a first cycle capacity of 276 and 240 mAh g^{-1} respectfully. A first cycle loss of 23 and 22% is also seen in both figures b and d. Furthermore, both maintain good long cycling data with capacities of 193 and 194 mAh g^{-1} at the 100th cycle and still both maintaining high coulombic efficiencies of 98 and 101% for LJ103 and LJ104 respectfully as shown in graphs a and c. LJ104 retains an average coulombic efficiency of 101% throughout the 100 cycles; it is unknown why the efficiency is in excess of 100% but it may be linked to the first cycle and the SEI formation during the first cycle.

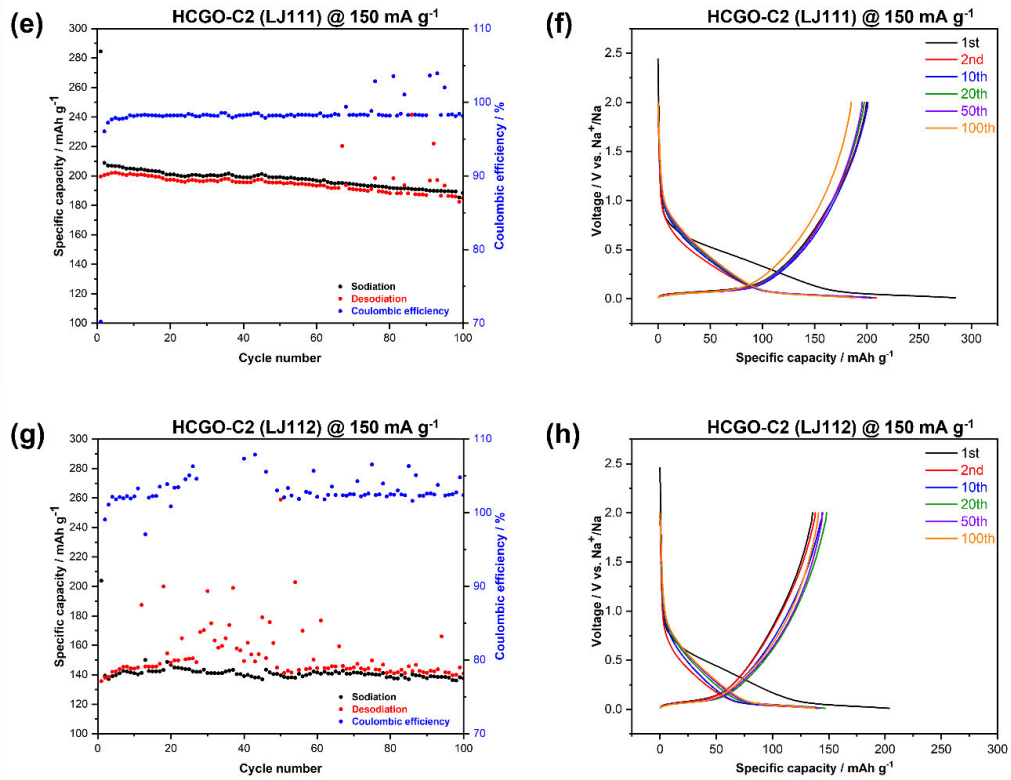

Figure 3.17: HCGO-C2 cycling, controlled ramp rate 2 (LJ111 e+f, LJ112 g+h)

Figure 3.17 above shows the hard carbon cycling data for the hard carbon graphene oxide controlled ramp rate 2 (HCGO-C2). As shown in the the results table above, both cells have a first cycle capacity of 185 and 141 mAh g^{-1} respectfully. A first cycle loss of 30 and 33% is also seen in both figures e and g. Furthermore, both maintain good long cycling data with capacities of 185 and 141 mAh g^{-1} at the 100th cycle and still both maintaining high coulombic efficiencies of 98% and 102% for LJ111 and LJ112 respectfully as shown in graphs e and g. As with the previous half-cells the first cycle shows the initial sodation and SEI formation due to the longer discharging profile.

3.6.4 Galvanostatic cycling discussion

Table 3.2 below shows the cycling results of all the half-cells.

Cell Name	HC/HCGO	Pyrolysis conditions	1st cycle capacity (mAh g-1)	1st cycle capacity loss (%)	100th cycle capacity (mAh g-1)	Capacity retention at 100th cycle (%)	Number of Cycles
LJ101	HC	Unspecified	308	30	192	89	116
LJ102	HC	Unspecified	266	28	174	91	126
LJ105	HCGO	Unspecified	224	19	160	88	403
LJ106	HCGO	Unspecified	308	18	121	48	350
LJ109	HC	Control 1	240	37	116	76	189
LJ110	HC	Control 1	259	38	127	78	176
LJ107	HCGO	Control 1	293	19	216	91	403
LJ108	HCGO	Control 1	309	21	248	102	353
LJ103	HC	Control 2	276	23	193	91	115
LJ104	HC	Control 2	240	22	194	104	117
LJ111	HCGO	Control 2	284	30	185	93	119
LJ112	HCGO	Control 2	204	33	141	104	160

Table 3.2: Overview of HC/HCGO cycling results

To allow a better overall comparison, cells were compared in terms of the mean capacity between 50 and 100 cycles as well as the standard deviation. This standard deviation can be used to evaluate the degree of cycle to cycle variability in the cell.

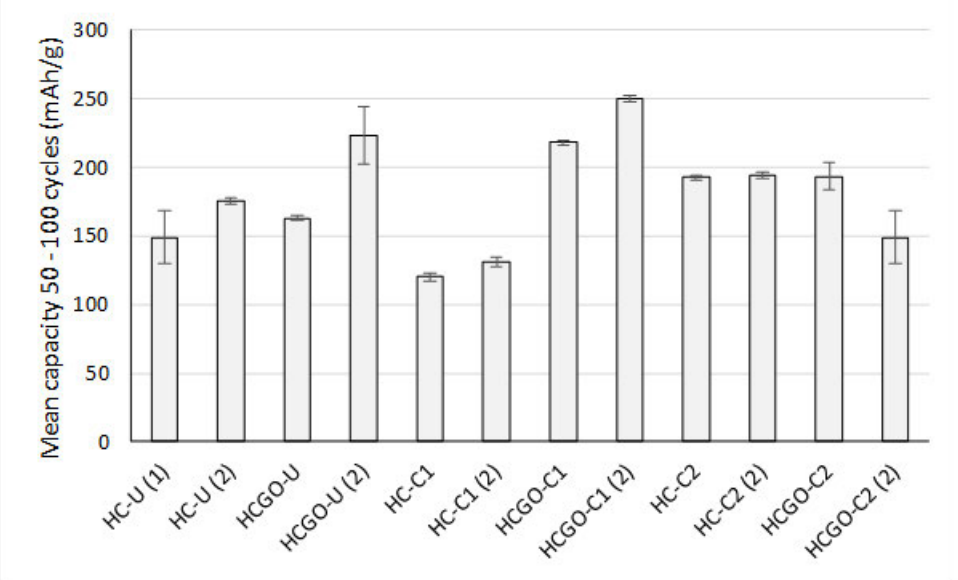

Figure 3.18: Standard deviation of cycles 50-100

Figure 3.18 above, shows the standard deviation of all hard carbon half-cells. The range of capacities observed is between 120-250 mAh g^{-1}. In general, there is minimal variation between most of the half-cells as evidenced by the flat sodiation capacities as shown in figure 3.18. Although HC-U (1), HCGO-U (2), and both HCGO-C2 are exceptions.

Most of the half-cells have minimal variation in capacity, this shows that both HC and HCGO overall have good long term cyclability. The average capacities across all the HC and HCGO half-cells were 160 mAh g^{-1} and 200 mAh g^{-1}. This suggests a 25% higher capacity when GO is used, the results should be treated with caution given the variability between the cells.

The pyrolysis regimes were selected to extend the time over which much of the mass change occurs in the sucrose precursor. This could be considered as being analogous to the widening of the temperature window that the mass change occurs in due to GO. For cells produced without GO, this hypothesis was not proven as there was not a clear association between ramp time and capacity, with the slowest ramping in the 200-400°C range giving the worst capacity. When GO was used, there were differences in the observed capacities but there was also inherent cell to cell variability between the cells. It was hypothesised that the mass loss transition may be integral to the mechanisms responsible for increased capacity, and that these could be enhanced by slowing down pyrolysis, but again this was not proven.

Additional further observations can be drawn from the data, when pyrolyzing using the unspecified and control 1, both HCGO C1 and C2 half-cells had a lower first cycle capacity loss compared to their HC counterparts; this was not the case with HCGO-C2.

Direct comparison to literature is made difficult by the range of anode compositions, electrolytes and cycling regimes utilised. However, work by *Luo et al.* does compare hard carbon half-cells with and without the use of GO. This work utilises a relatively high cycling rate and there is clear evidence of the effect of cycling rate on the capacity, with faster charge/discharge cycles resulting in lower cell capacities. Low cycling rates are often used as they give high headline capacity results though the comparison of cell precursors is valid so long as the data is compared at the same rate.

The cycling rate used in this study was 150 mA g^{-1}, this fits between the cycling rates of 100 and 200 mA g^{-1} shown by *Luo et al.* shown in figure 3.18.

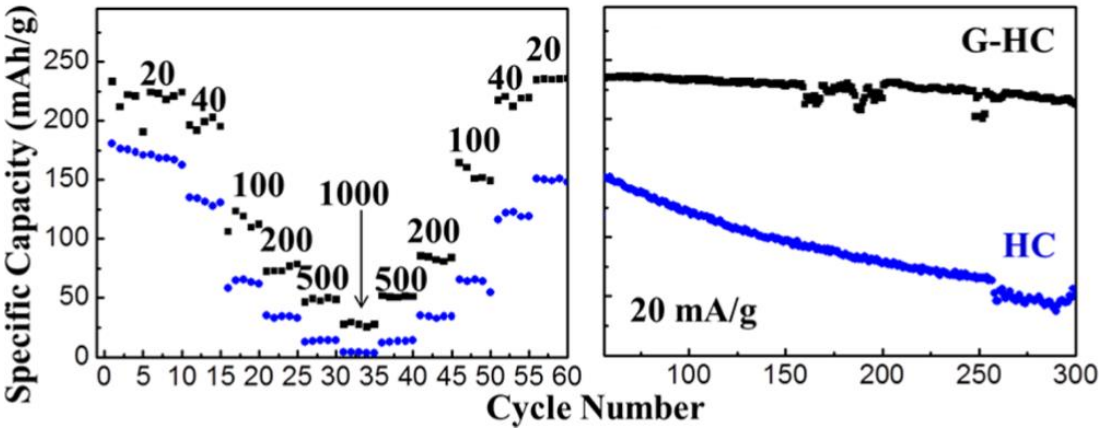

Figure 3.19: HC and HCGO cycling data by (W. Luo et al., 2015)

As seen above in figure 3.19, *Luo et al*. apply a variety of current densities (left graph) and long term cycling at 20 mA g^{-1} for both HC and HCGO (right graph). When cycling at 20 mA g^{-1} on the right graph, both HC and HCGO (G-HC on the graph) the HCGO achieves a capacity of ~220 mAh g^{-1} at 100 cycles, the HC initially has a capacity of ~170 mAh g^{-1} which slowly decreases to ~125 mAh g^{-1}. When comparing to the results above in this chapter, the HCGO half cells all have a lower 100th cycle capacity except for one of the HCGO-C1 half-cells which has a capacity of 248 mAh g^{-1}; the lowest being one of the HCGO-U half-cells with a capacity of 121 mAh g^{-1}. Regarding the HC data after 100 cycles only one of the half-cells, HC-C1 has a lower capacity than seen in figure 3.18 above, with a capacity of 116 mAh g^{-1}. However, the average capacities for the HCGO and HC half-cells in the results above is 179 mAh g^{-1} and 166 mAh g^{-1} respectfully. The cells that use GO showed a greater capacity than those with only HC. This difference seems to apply for all C rates but is magnified at a lower C rate where the differences are more apparent. Overall, GO in this study does offer a 25% increase between the cells compared with those without GO. This seems approximately in line with *Luo et al.*, so this could potentially/cautiously be a benefit with results from this study; however once again caution should be taken with the variability between the half-cells.

So, in conclusion the galvanostatic cycling shows promising results with the inclusion of GO approximately in line with *Luo et al.* but caution should be taken when

comparing. Furthermore, it is shown that even at a high current density rate of 150 mA g^{-1} the half-cells show promising results for long term cyclability.

3.7 Cyclic Voltammetry

This section focuses of CV analysis of HC and HCGO, both of which used the second controlled pyrolysis methods, HC-C2 and HCGO-C2. This was a supplementary analysis technique to determine if any differences could be observed between the -C2 half-cells. New half-cells were assembled for this CV analysis.

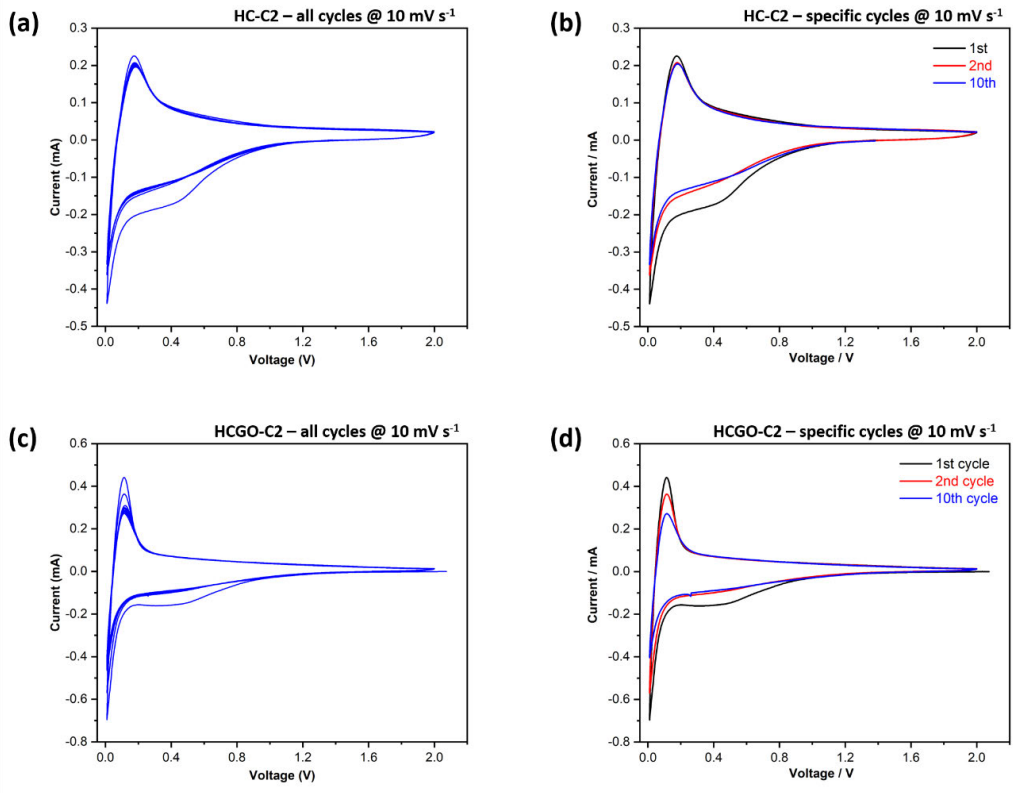

Figure 3.20: CV analysis of HC-C2 (a+b), HCGO-C2 (c+d), (a+c show all cycles, b+d show cycles 1,2 and 10)

As previously discussed in the methods chapter, CV analysis shows the voltages at which Na^+ ions intercalate and de-intercalate. Figure 3.20 shows this data. A constant

voltage, in this case is 10 mV s^{-1} (+/-) is applied between a fixed voltage window (0.01-2 V for HC/HCGO) and the current is measured as the voltage is increased/decreased, this current value changes during intercalation and de-intercalation voltages. The voltage window is the same range as used for the galvanostatic cycling.

Differences can be observed be observed in figure 3.20 above. Specifically, with the current values required for the transition of the Na+ ions into/out of the lattice structures. . From the data, the specific current required for the intercalation/de-intercalation into the HCGO is significantly higher than that required for the HC. The HC required a current of +0.2/-0.4 mA, whilst the HCGO required +0.4/-0.6 mA. Furthermore, the breadth of the current peaks is wider for the HC. This could potentially be related to why a lower specific capacity is required; the intercalation/de-intercalation of the Na^+ ions occur over a broader voltage range. This could possibly be associated with a more flexible lattice structure, which may be more expandable decreasing the physical resistance needed to 'push'/'pull' the ions in and out. Whereas with the HCGO the breadth of the intercalation/deintercalation voltage peaks are thinner, hence the increase in required current. The differences between the two is likely to be attributed to the inclusion of graphene oxide in the matrix structure. The first cycle of both is different to the remaining cycles, an additional increase in specific current at a higher voltage can be seen in graphs b and d. The HC has an increased specific current in the range of 0.2-0.8 V and similarly for the HCGO. This is mostly likely to be associated with the first structural change for each of the framework structures; after the structures have both undergone this first volume expansion the future cycles are considerably more efficient. The initial de-intercalation afterwards also shows an increased specific current most probably related to the first structural volume shrinkage and the initial increased internal resistance to remove the Na^+ ions. To summarise, the CV analysis shows that there are differences between the HC and HCGO and this is likely to be attributed to the inclusion of GO due to matrix structure differences, however this cannot be completely certain.

3.8 Closure

This chapter set out to explore the synthesis of hard carbon; specifically looking into the manipulation of the ramp rates used during pyrolysation stage in the synthesis of hard carbon. The focus targeted a key temperature range in which there is a rapid change in mass to determine if slowing the ramp rate through this temperature window has any impact on the outcome. Graphene oxide proved to be a promising additive that has been studied in literature that when included in the synthesis of hard carbon.

Overall, 3 ramp rates were chosen, an undefined and two controlled ramp rates, synthesised for both HC and HCGO. The resultant materials were then characterised through XRD, XPS and SEM analysis. No differences were seen in XRD but this does not mean the materials are identical as XRD analysis can be difficult depending on conditions with carbons, however the SEM doe shows a difference in morphology, mainly the topography of the powders with HC having a considerably smoother surface compared to the HCGOs.. XPS results showed minimal differences between the synthesised powders, with carbon and oxygen being the two main elements present on the surfaces. SEM however did show slight differences in the HCs and HCGOs. Electrochemical characterisation was undertaken through half-cells to analyse the cycling performances of the powders through both galvanostatic cycling and cyclic voltammetry. The GC shows that using GO during the pyrolysis showed a greater capacity than the powders without the addition of GO; a 25% increase which was roughly in line with literature. Between the HC and HCGO the first -C1 ramp rate had the largest difference in capacity between the two. However, caution must be taken due to the given variability between the cells. CV analysis showed differences again between HC and HCGO with a significantly higher current needing to be applied to allow sodiation/de-sodiation; so, there are some underlying differences in the materials that may account for the differences; but the mechanisms responsible are not clear.

From a manufacturing perspective, the extra process step of incorporating GO offers a potentially valuable benefit to capacity, but slowing down the ramp rate of the pyrolysis process does not show evidence of enhancing capacity and cannot justify the extra processing time that would be required

To close, the manipulation of the ramp rate does have an impact on the cycling ability of hard carbon, although the evidence is mixed. The inclusion of GO also has positive benefits with regards to the increase in capacity. The first controlled ramp rate -C1 showed the largest differences between the HC and HCGO specifically..

The next chapter will explore the influence of rGO on sodium rhodizonate; through using a reverse recrystallization technique to change the particle size of the rhodizonate and then if the inclusion of rGO can enhance the recrystallisation process further.

Part 4

Sodium Rhodizonate

4.1 Introduction

The previous chapter showed the successful development of hard carbon anodes with the addition of graphene oxide and that manipulating the pyrolysis conditions including ramp rates and holding temperatures impacts the cycling capacities. Likewise, this chapter follows a similar process to develop a compatible cathode.

A relatively new starting material has recently been researched in literature that offers promising cathodic properties for ion-based batteries: rhodizonic acid-based compounds. These compounds have been used in multiple forms throughout lithium-ion based batteries, including lithium rhodizonate and copper-based rhodizonate. These rhodizonic acid compounds also offer a great opportunity to develop sodium-ion based electrodes using through sodium rhodizonate.

Sodium rhodizonate is an organic salt that can be obtained from natural biomass sources, these offer a potential precursor that could lead to the successful development of cathodes for sodium-ion batteries. Biomass sources offer benefits including great abundance, low-cost and are very sustainable compounds. Potentially, sodium rhodizonate can offer high energy densities and long-term cycling stability. [1,2,3]

The key benefits from using the rhodizonate is obtained through its organic structure; it offers an extremely flexible structure and easy functionalisation. These then make it ideal to accommodate the continued insertion and removal of sodium ions; a problem that has previously limited SIB development due to the large increase in size compared to lithium ions in which most SIB developments originate from. [4-8]

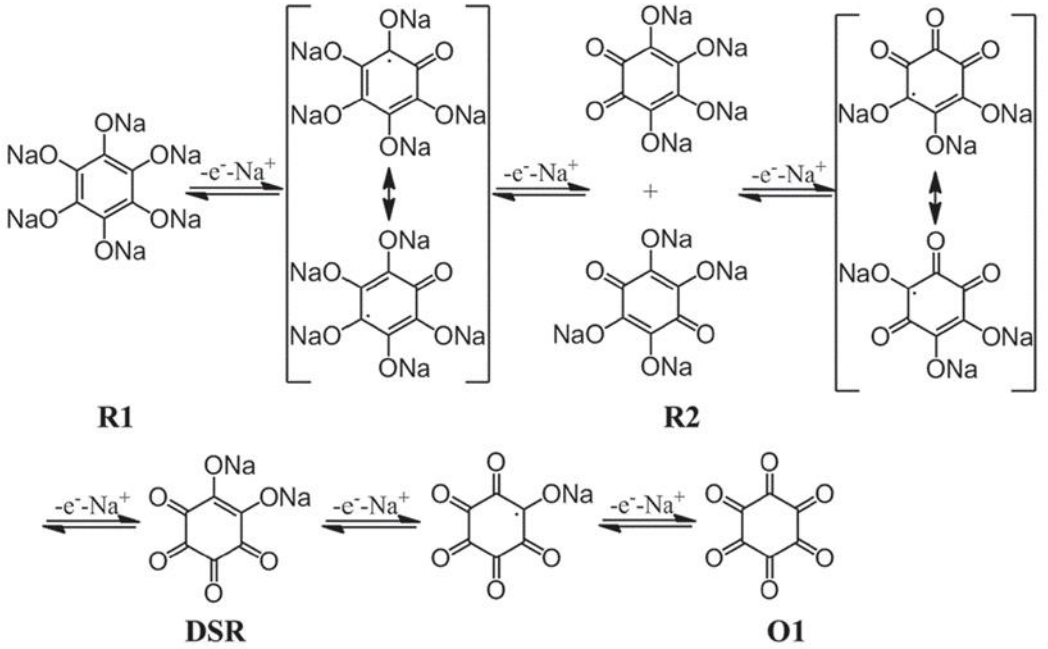

Figure 4.1: Schematic diagram of sidoum rhodizonate and its discharged states (R1 and R2) and potential charged state (O1) (Dinnebier et al., 2005)

Figure 4.1 above shows the versatility of the sodium rhodizonate; with its abilities to vary the number of sodium ions through redox reactions. Initially there are 2 Na ions bonded however this can increase up to a maximum of 6, with the potential to remove the sodium ions. Potentially allowing a significant amount of sodium ions to intercalate and de-intercalate. This impressive versatility of sodium rhodizonate as a potential cathodic material justifies why there is considerable research into its use for sodium-ion batteries.

In this chapter, there will be three main variants of sodium rhodizonate synthesised and electrochemically tested; the three types, named based on processing and ultimate particle size, which are explored were as follows:

1. Macro Rhodizonate (MR) – this variant is synthesised directly and has no chemical manipulation

2. Nano Rhodizonate (NR) – this variant goes through a recrystallisation process to directly influence the particle size of the rhodizonate

3. Nano Rhodizonate + rGO (NRR) – this variant follows a similar synthesis to the NR however there is also the inclusion of reduced graphene oxide.

The concept to add the rGO was chosen to improve the recrystallization technique potentially further, allowing optimised preferential recrystallization on the rGO flakes; the nano particles could recrystallise onto the rGO flakes and offering a site to recrystallise onto, rather than recrystallising uncontrolled in the solution. Hopefully, the rGO flakes will then improve the cycling performance of the batteries by allowing this to happen.

The resultant materials after synthesis will be characterised through XRD, XPS and SEM for comparison between each variant. Electrochemical characterisation will use GC (galvanostatic cycling) supplemented by CV (cyclic voltammetry).

4.2 Synthesis of sodium rhodizonate

Multiple synthesis methods were used throughout, the final synthesis method for each type of sodium rhodizonate is shown below. The MR required no synthesis techniques, as was used directly from the source bottle as discussed in the methods section.

The nano variant NR involved dissolving the Sodium Rhodizonate precursor Sodium rhodizonate dibasic into a deionised water solution above room temperature then with the addition of ethanol at the chosen elevated temperature the dissolved rhodizonate quickly recrystallises into ‘nano’ crystals within the solution. After allowing to cool to RT the solution is then filtered to remove and discard deionized water/ethanol mixture. Details of temperature, time length, reagents are presented later.

Whilst the NRR involves the recrystallisation technique like the NR, but with the inclusion of High Porosity Reduced Graphene Oxide as an additional precursor to the Sodium rhodizonate. However, there were slight differences between the NR and NRR synthesis methods. The NRR required vacuum filtering, whilst the NR was filtered using a centrifuge. This being due to the relatively fragile rGO flakes. The inclusion of rGO required an additional step beforehand during the synthesis. This included dispersing the rGO throughout the deionized water in the recrystallization step; an ultrasonicator probe was used for dispersion of the rGO flakes.

4.2.1 Macro rhodizonate

As there was no recrystallisation stage required to change the particle size of the Sodium Rhodizonate, no synthesis was undertaken. It was used directly from the source bottle; this source is discussed in the previous methods chapter.

As discussed in the introduction section of this chapter, a recrystallization process had to be undertaken to influence the particle size. Two concentrations were chosen following the research paper (Lee et al., 2017), , these involved changing the Rhodizonate/water ratio, being either 2mg/ml and 4mg/ml.

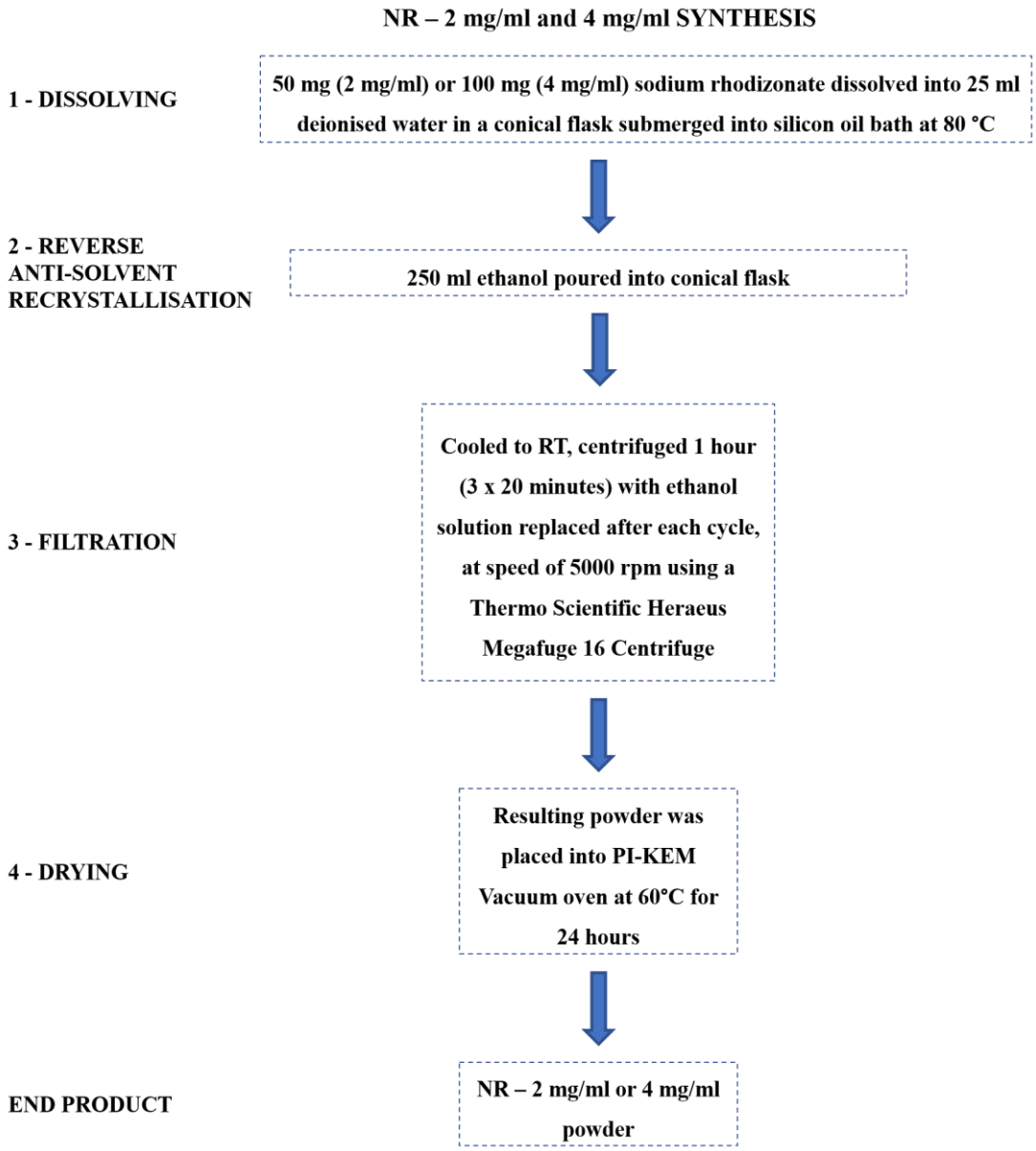

Figure 4.2: Flowchart showing the synthesis of nano rhodizonate with a concentration of 2 mg/ml and 4 mg/ml

Figure 4.2 above shows the synthesis method for nano rhodizonate, showing both the 2 mg/ml and 4 mg/ml concentrations. Once the sodium rhodizonate has been added to the water, ethanol is poured into the solution which through a reverse anti-solvent recrystallisation reaction decreases the particle size into the nano rhodizonate form.

The solution is then filtered to remove the water, a centrifuge is used to separate the solid from the liquid. The solution is centrifuged for 1 hour overall in 3 x 20 minute cycles, after each cycle the liquid is removed, and fresh ethanol is added. Once the final cycle has been completed the remaining powder is removed and dried in a vacuum oven for 24 hours to remove all excess moisture.

4.2.2 Nano rhodizonate w/ rGO

Figure 4.3 below shows the synthesis method for the nano rhodizonate with the inclusion of rGO. Prior to dissolving the sodium rhodizonate into the deionised water, the rGO flakes are dispersed using an ultrasonic probe beforehand. The other key difference is the choice of filtration method, the NR separation method used a centrifuge, whilst the resultant NRR solution was passed through MF-Millipore™ Membrane Filter, 8 µm pore size using a vacuum filtration technique. The change in filtration method was chosen as a precautionary alternative to hopefully prevent damage to the rGO flakes. Once filtered, the powder was dried in a vacuum oven overnight as with the NR synthesis. Two concentrations were chosen for the NRR synthesis were the same as the NR which were 2 mg/ml and 4 mg/ml.

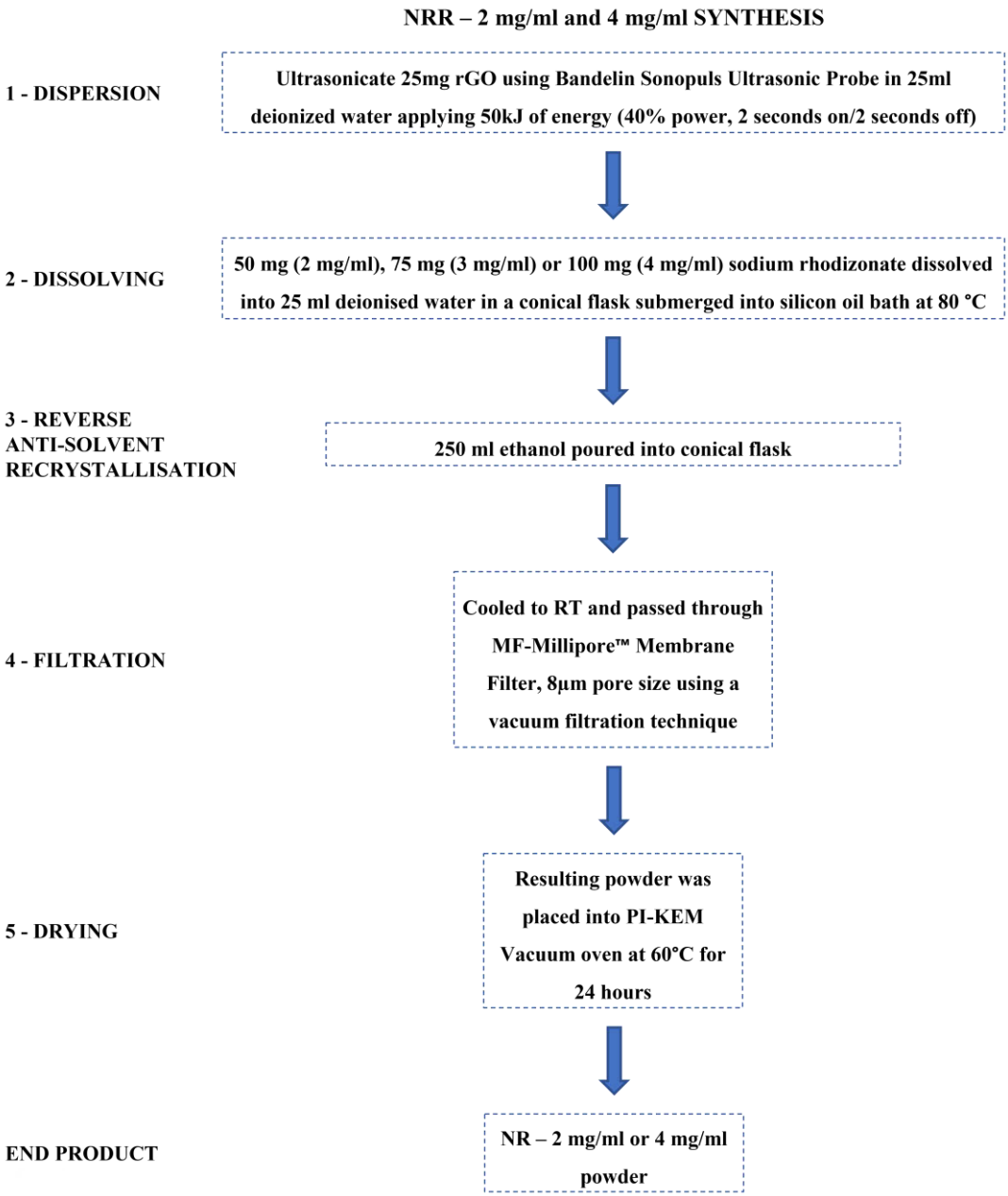

Figure 4.3: Flowchart showing the synthesis of nano rhodizonate with rGO using concentrations of 2 mg/ml and 4 mg/ml

4.2.4 Synthesis development and optimisation

Each stage of the synthesis for NR and NRR had to be developed and optimised to ensure that the syntheses were successful in decreasing the particle size as required in a consistent and repeatable manner. The first problem was how to ensure a constant 80 °C temperature for the conical flask, and for this a silicon oil bath was as seen below in figure 4.4.

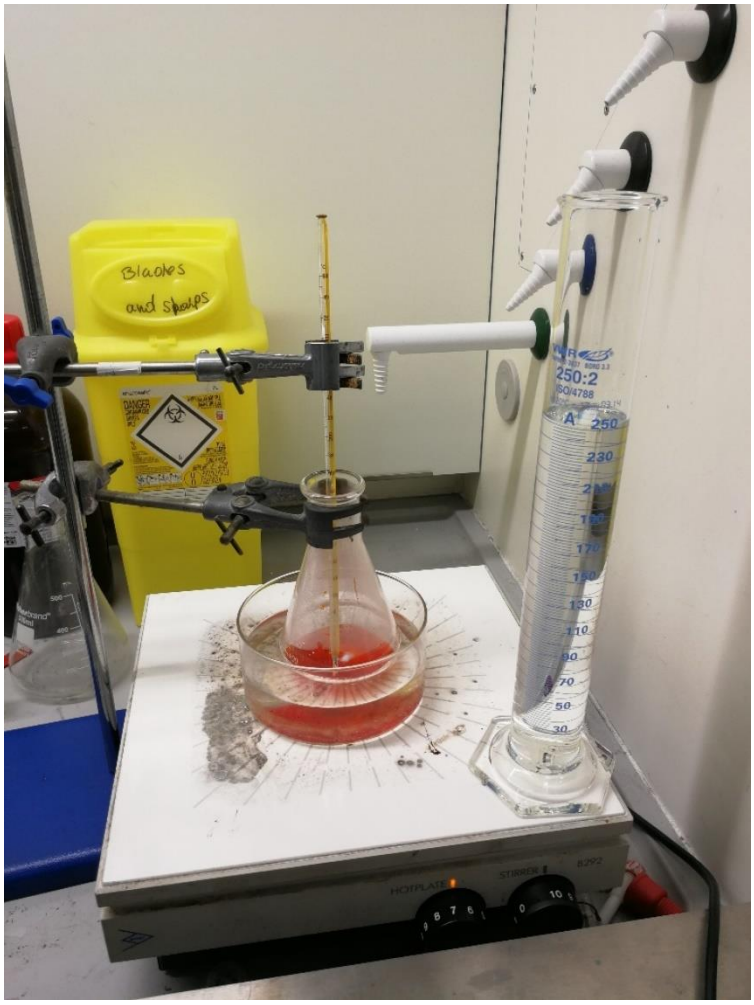

Figure 4.4: Image showing dissolved rhodizonate at 80 °C

The conical flask was placed into a silicon oil bath, the deionised water within the conical flask was uniformly enclosed within the oil bath. This then allowed the temperature of the deionised water throughout to be monitored. A thermometer was used throughout to verify this. Once the deionised water had reached 80 °C, the rhodizonate was added, followed by the ethanol. Once both had been added to the water, the flask was removed to cool down. Silicon oil was selected as it offers good

heat transfer medium not subject to evaporation at the temperatures required. Heating the solution up very slowly was a slow process, however this ensured that minimal/if any at all water evaporation, which would then cause unwanted changes to the ratio of water/ethanol required for a successful synthesis.

Another key step which required optimising was the recrystallisation process when adding in the ethanol. A consistent and repeatable flow rate was needed for reproducibility and to ensure the synthesis was repeatable. To ensure the consistent flow rate, multiple test pouring's undertaken to ensure repeatability. Unfortunately, the recrystallisation process was not always successful, it was not clear why this occurred. Figure 4.5 below shows examples of successful and unsuccessful recrystallisation.

Figure 4.5: After recrystallisation, left image successful, right image unsuccessful

The last key stage that needed refining was the filtration, as previously discussed the NR used a centrifuge filtration technique, whilst the NRR used a vacuum pump filtration technique.

Figure 4.6: Example of centrifuge setup on left, example of a successful centrifuge on right where the powder can be seen at the tip of the tube

It is worth noting that this filtration technique uses a considerable amount of ethanol due to the requirement of replacing the ethanol/water solution after each 20 minute cycle; to continually remove the excess water. Like that of the previous stage, the centrifuge filtration was not always successful. Figure 4.7 below shows an example. Furthermore, similarly to the recrystallisation stage, unexpected errors in the filtration stage occurred, including water contamination. At this final stage of the synthesis before drying, it is worth noting that for a synthesis that has multiple key stages; it was important to ensure that this final step was reliable. If errors were to occur, then the synthesis must be restarted from the beginning, which requires considerable time and consumables.

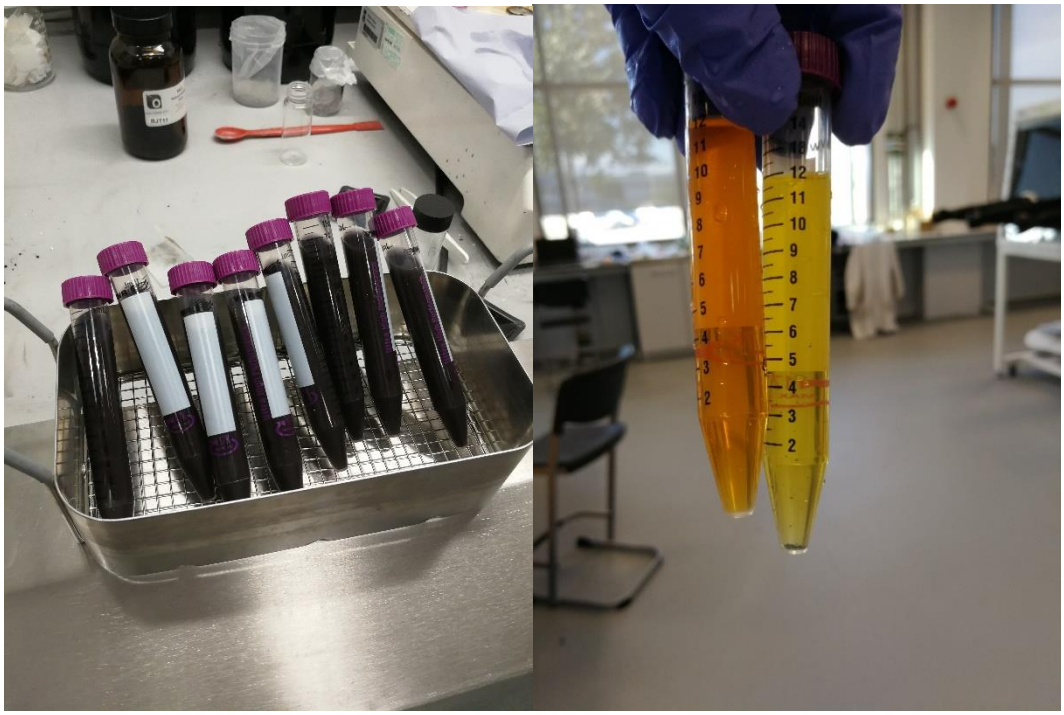

Figure 4.7: Centrifuge after first 20 minute cycle with new ethanol added, left image shows successful recrystallisation and filtration, right shows unsuccessful this can be clearly identified due to the colour of the solutions

The colour differences shown above in figure 4.7 shows a variation in the synthesis. The orange and yellow colouring shows an error has occurred during the recrystallisation process. As there is no/minimal colour change (orange/yellow) after the recrystallisation step, this stage has failed to recrystallise the rhodizonate into NR as wanted; meaning that batch had to be scrapped.

The other filtration method that was used for the NRR specifically, was using a vacuum filtration technique. Using a Büchner funnel and flask, connected to a vacuum line the NRR was able to be sucked through the 8 µm membrane filter, enabling the entrapment of the powder whilst removing the waste ethanol/water solution. Once successful, the powder along with the membrane was dried for 24 hours in a vacuum oven to remove the residual moisture. An example of the setup can be seen below in figure 4.8.

Figure 4.8: Vacuum filtration using Büchner funnel and flask

Figure 4.8 above, shows the setup for the vacuum filtration process. Some of the ethanol/water solution has already been filtered in the bottom of the Büchner flask, with a large quantity currently being filtered through the Büchner funnel which inside has the 8 µm membrane filter and the remaining NRR in the conical flask.

It is worth noting that due to the use of specialised glassware/equipment throughout the synthesise consistency was crucial. By ensuring that each synthesis was completed in one sitting using a consistent and constant timeline each for each synthesis, the chance of contamination was minimalised.

4.3 Characterisation of sodium rhodizonates

All variants of the rhodizonate powders underwent two characterisation methods, XRD and SEM.

XRD was chosen to see if there were any differences in the crystal structures of the because of the various synthesis methods used. SEM was chosen to see the morphology and surface differences between the various powders and evaluatethe inclusion of the rGO flakes.

4.3.1 XRD analysis

XRD analysis was undertaken on all variants of the sodium rhodizonates, these included MR, NR and NRR. This will then allow analysis of the crystal structures for comparison between all variants. Figure 4.9 below shows the plot for MR, figure 4.10 shows both NR powders, figure 4.11 shows both NRR powders and figure 4.12 shows MR, NR(2:1) and NRR (2:1) overlay.

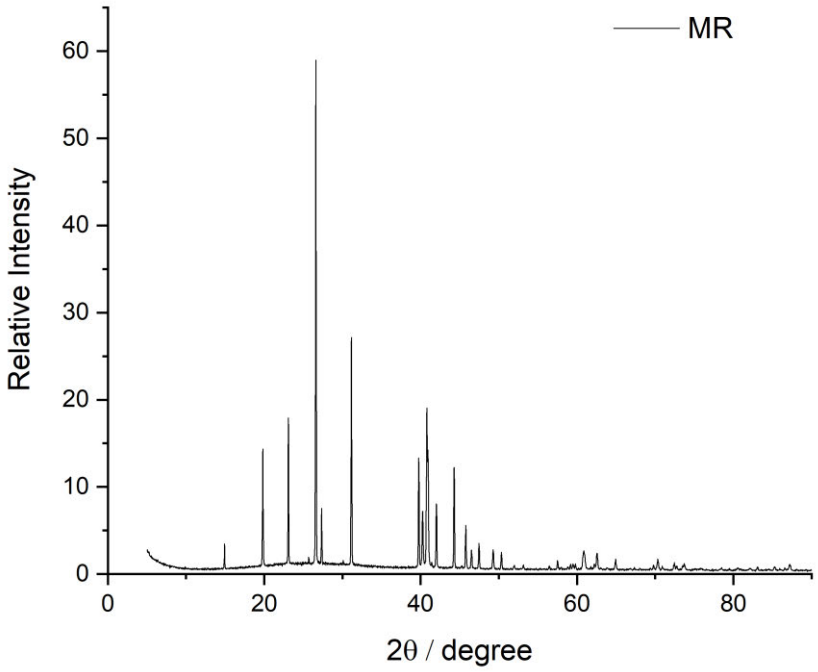

Figure 4.9: XRD plot of MR (macro rhodizonate)

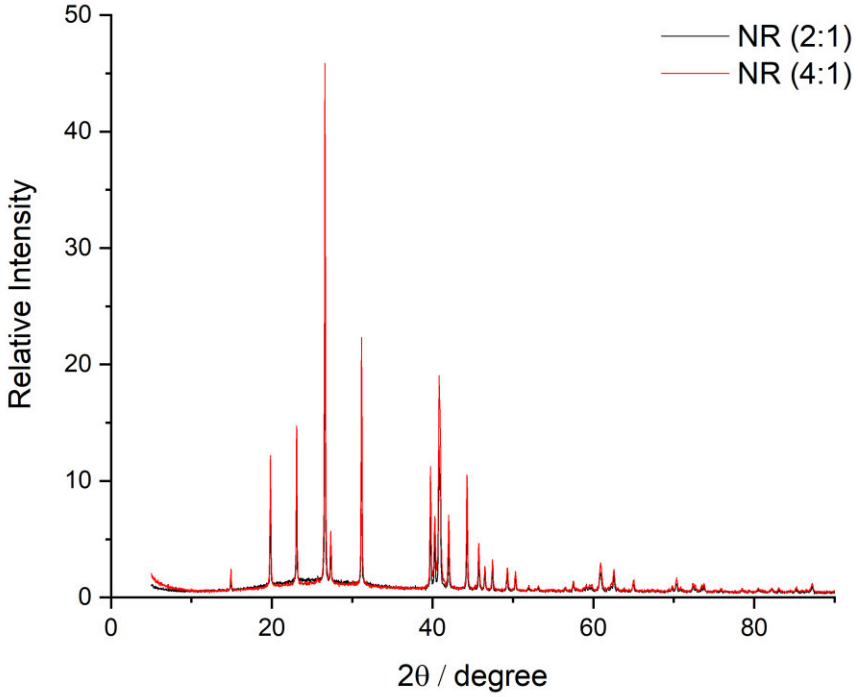

Figure 4.10: XRD plot of NRs (nano rhodizonate 2:1 and 4:1)

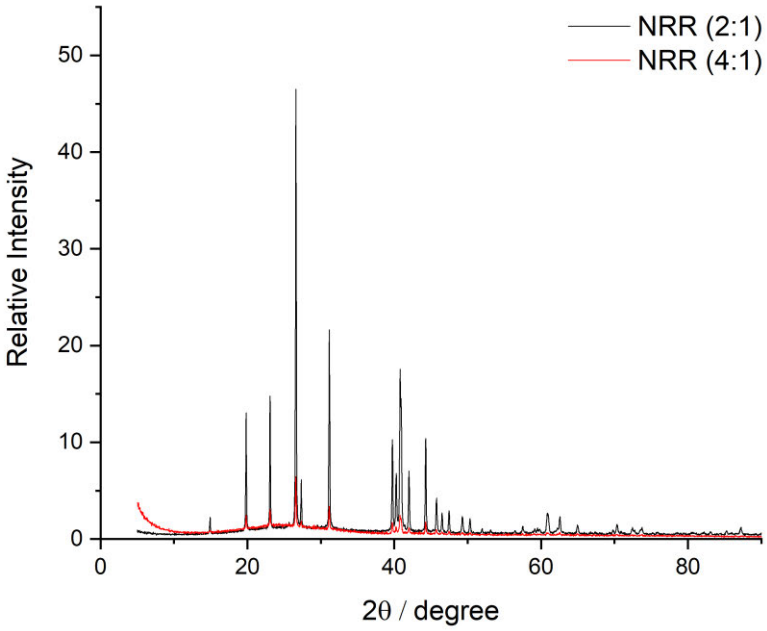

Figure 4.11: XRD plot of NRRs (nano rhodizonates w/ rGO 2:1 and 4:1)

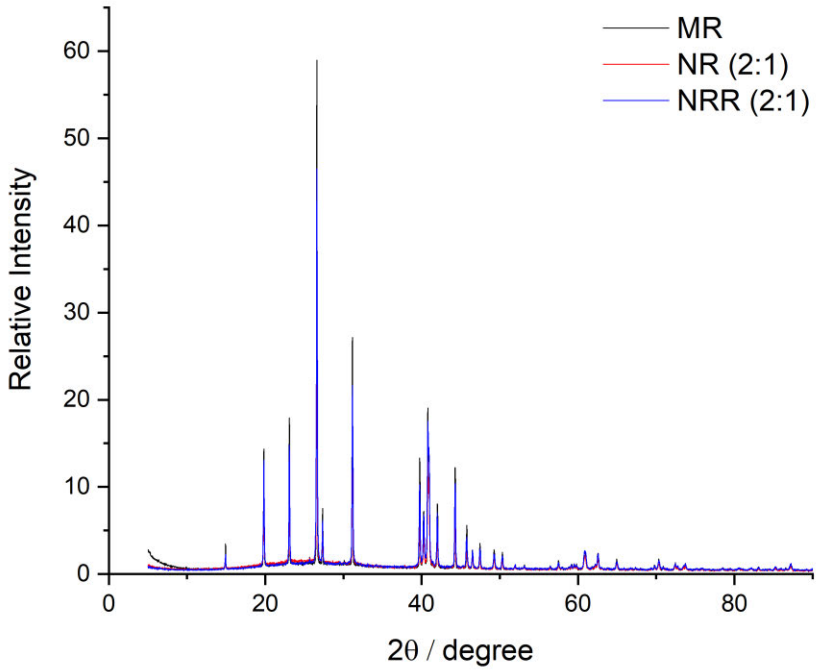

Figure 4.12: XRD overlay MR, NR (nano rhodizonate 2:1) and NRR (nano rhodizonate w/rGO 2:1)

As shown in figures 4.9-12, XRD plots are shown for all variants of sodium rhodizonate. MR can be used as a reference due to it being unmodified in any way and directly from the source bottle, there are no visible and significant differences between any of the NRs and NRR to the MR. Thus, the crystal structure remains mainly unchanged as the main peaks for each are all visible at the same degrees. It is worth noting that the main difference between the variants is the NRRs and the inclusion of the rGO; yet it is not visible compared to the others. This is likely to be due to the very small quantity used and the SEM analysis below confirms that rGO is present in the powders.

4.3.2 SEM analysis

The rhodizonate powders were analysed using SEM, the MR directly from the container and NR and NRR after successful syntheses. As previously mentioned in the experimental methods chapter, two SEM machines were used, an EVO for the lower magnifications and a JEOL for the higher magnifications.

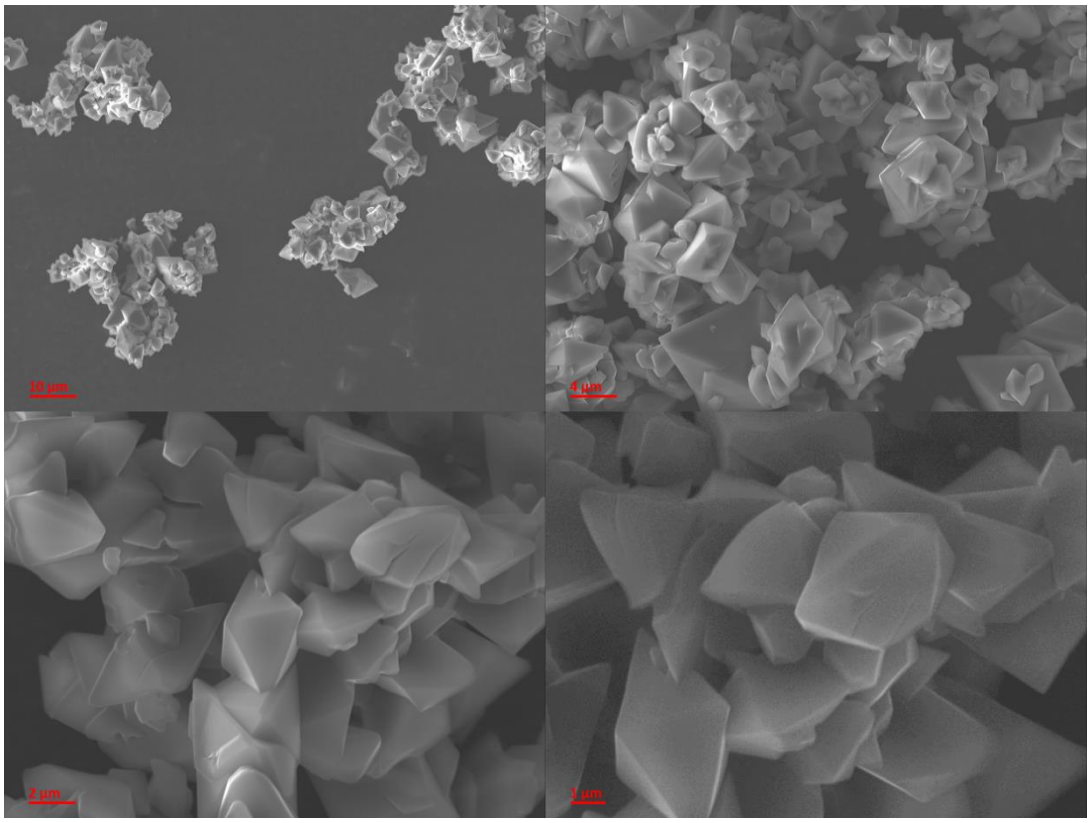

Figure 4.13: SEM analysis of MR (macro rhodizonate) at a range of magnifications

The MR was taken directly from the bottle and can be seen above using the EVO SEM. The morphology is very uniform with most of the structures being quite 'octahedral like' and having a uniform particle size of 4µm by 2µm. The topography of each crystal is very smooth with some having a few cracks on the surface. These crystals did not undergo any particle size modifications and are then considered the final particle shape before the casting process.

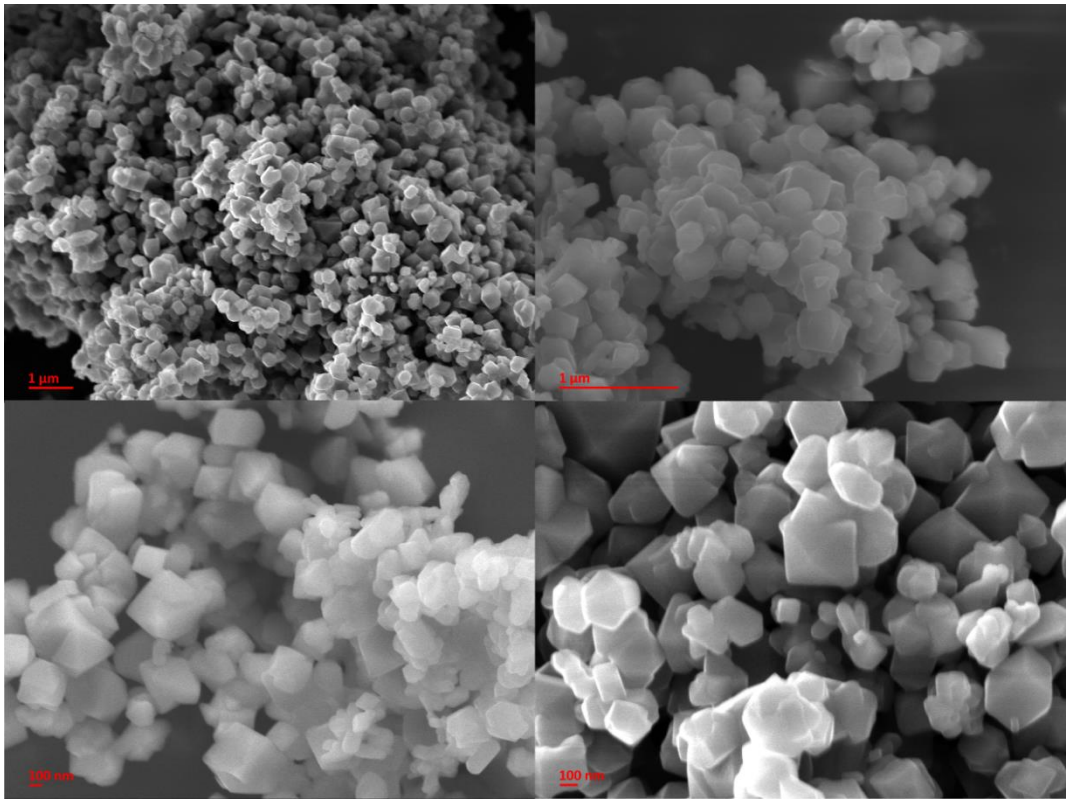

Figure 4.14: SEM characterisation of NR (nano rhodizonate)

Figure 4.14 above shows the nano rhodizonate. After the rhodizonate underwent the re-crystallisation process the particle size has dropped significantly. With nearly all the particles having a diameter of 200 micron or smaller. Compared to the MR rhodizonate as seen in figure 4.13, the morphology of the particles has changed quite significantly from 'octahedral-like' to a more cube/cuboid shaped particle. The smooth surface is maintained from the raw rhodizonate. All the particles are similar in shape, size and texture which shows that the re-crystallisation process was successful, effective, and controlled ensuring homogeneity throughout.

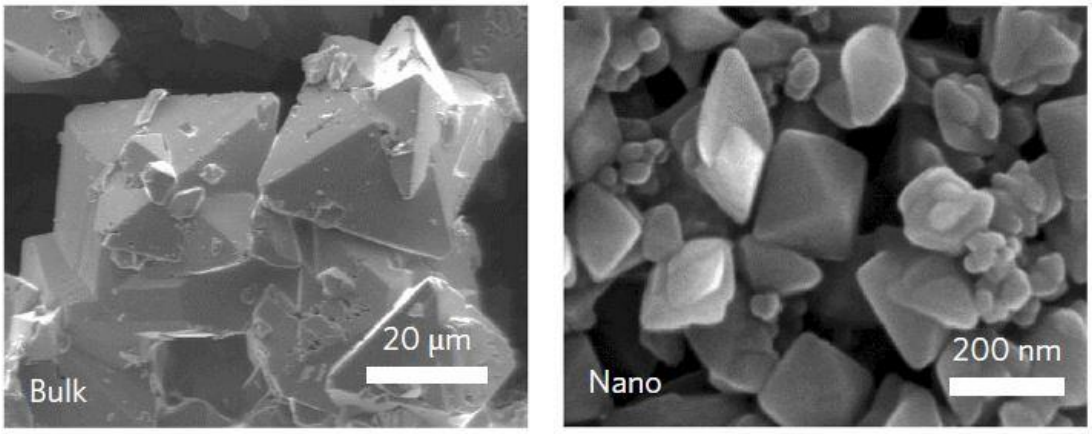

Figure 4.15: SEM images of rhodizonate (bulk left, nano right) (Lee et al.)

Figure 4.15 above shows rhodizonate SEM images taken from literature *(Lee et al.).* By comparison differences in particle size between the bulk rhodizonate images can be seen; *Lee et al.* bulk rhodizonate is significantly larger. *Lee et al*. have a diameter larger than 20 µm compared to 2 µm. However, the differences between the nano SEM images are negligible, the diameters of both are nearly identical, both being ~200 nm. This shows that the synthesis into nanoparticles has been successful.

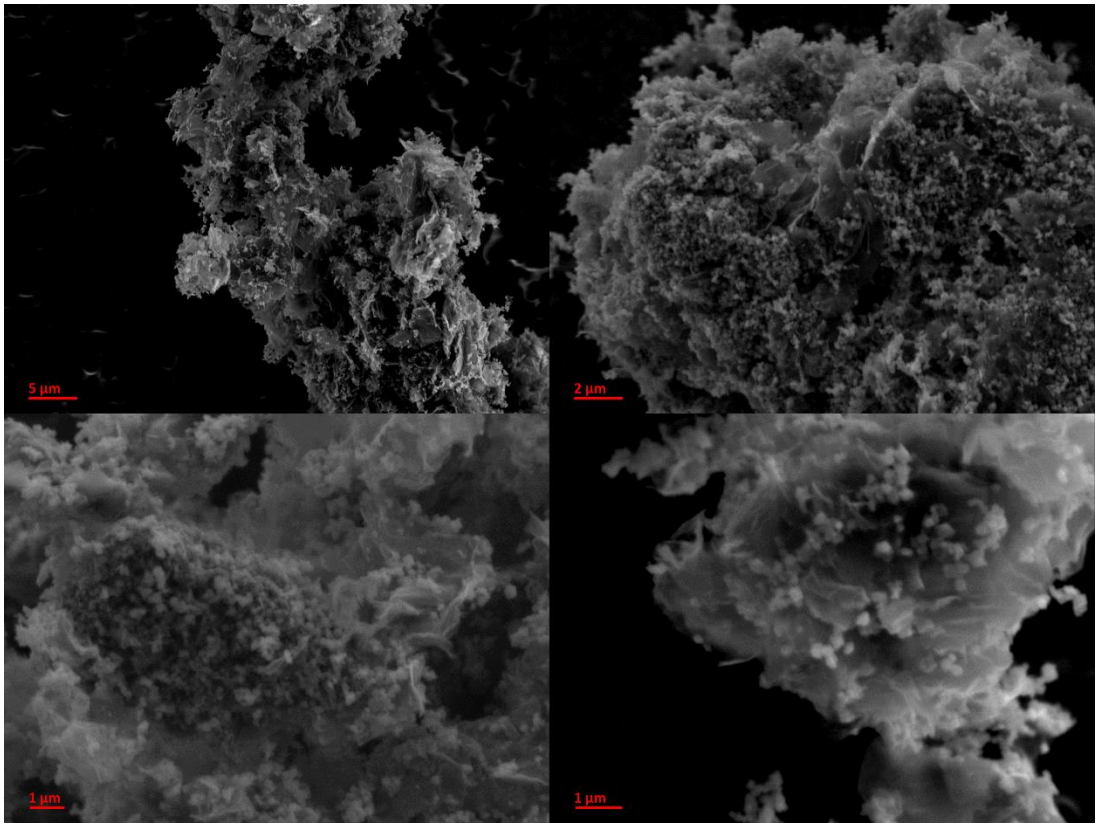

Figure 4.16: SEM characterisation of NRR (nano/rGO rhodizonate)

Above, in figure 4.16 there are the SEM images for NRR particles. Both rGO flakes and nano rhodizonate particles are present; showing that the NRR synthesis was successful. The rhodizonate particles are very similar to that of the NR particles in figure 4.14, by having a particle size of ~200nm and the same morphology. The rGO flakes can also be seen and are likely undamaged and can be seen in the SEM analysis through the disordered particles which have the small rhodizonate particles on the surfaces. The use of vacuum filtering as an alternative to the centrifuge, which the NR used to remove the excess water from the synthesis.

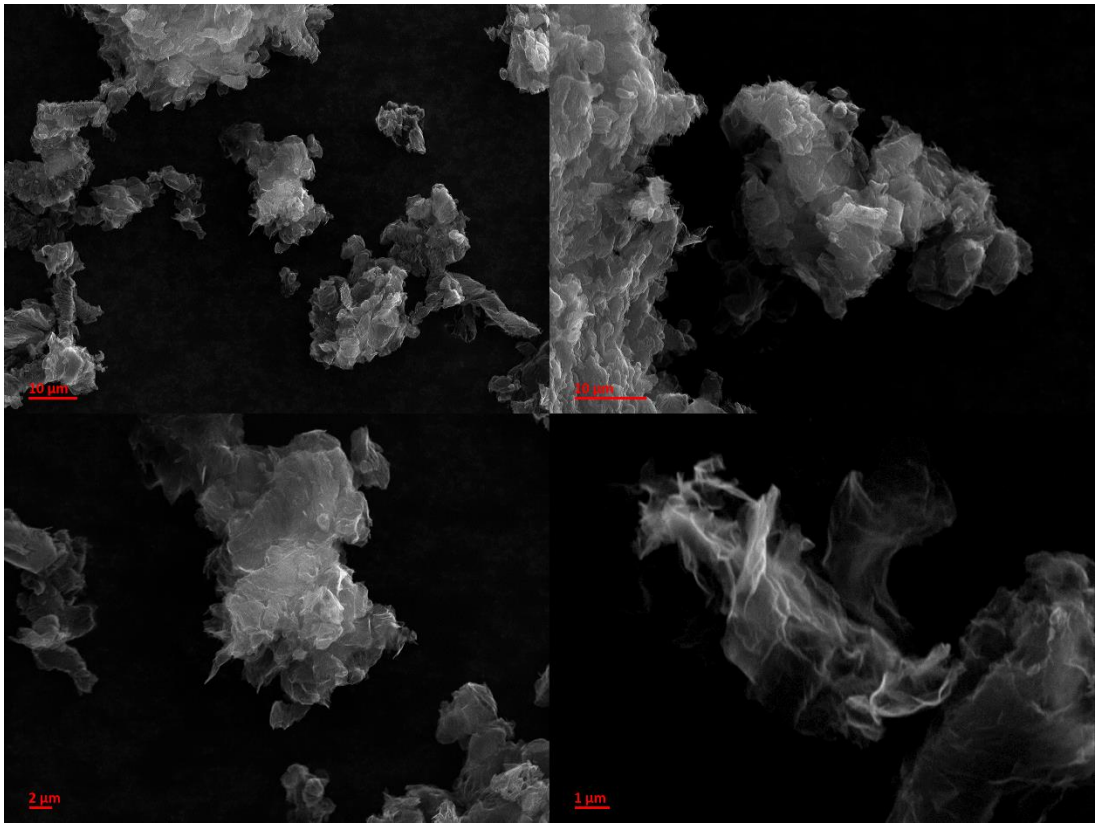

Figure 4.17: SEM characterisation of the rGO flakes

Above in figure 4.17 are separate SEM images for the rGO flakes used in the synthesis of the NRR; they have been included to show the morphology of the flakes beforehand. Thus, offering a direct comparison between the flakes before and after being used.

To conclude, SEM analysis shows that there are differences as seen through the recrystallisation which resulted in a particle size reduction from 200 micron to 20 micron, when rGO was incorporated into the synthesis it did not appear to interfere with the recrystallisation of the rhodizonate particles. Each synthesised variant has differences in particle shape, size and surface features compared to the MR which did not undergo any changes. The NR shows a successful crystallisation synthesis offering

nanometre-sized cubic orientated structures; with a small discrepancy in sizes between all the synthesised cubes which is to be expected from such synthesis. Regarding the NRR, the idea behind the synthesis was to recrystallise the sodium rhodizonate into 'nano' cubes onto the rGO flakes; figure 4.16 above successfully shows this was achieved. There also appears to be minimal if any damage to the rGO flakes which helps verify that the rGO flakes were undamaged during the filtration stage of the synthesis which was initially a cause for concern.

4.4 Electrode Development and Binder/Electrolyte Optimisation

A similar approach of electrode manufacture and sodium half-cell assembly and testing to that of Chapter 3 was carried out, the crucial difference being that rhodizonate half-cells were cathodes rather than anodes. Electrochemical analysis was also undertaken on all variants of the rhodizonate using sodium metal half-cells. For this, the variants were made into slurries and cast onto aluminium foil. The slurries were then cut to size to all half-cells to be made; then allowing the electrochemical characterisation to start. The details for the steps involved, including the chemicals and equipment used as shown in detail in Chapter 2. The data presented in this chapter used a common binder, solvents, and electrolytes for all half-cells, however there were multiple preliminary tests that were conducted to finalize the best system, which included a variety of binders/solvents/electrolyte combinations and then cycled.

The binders and solvents were the first key component to be explored as these are used during the fabrication of the slurries. There were two binders that were explored, the first being PTFE, the second 'Kynar' PVDF which was also used for the hard carbons in the previous chapter. Multiple solvents were tested with these two binders, which included NMP, THF and ethanol. Ultimately, the PTFE/NMP binder/solvent combination was chosen as the casting of the slurries was easiest. As previously discussed in chapter 2, NMP is a widely used solvent with many beneficial properties and an effective solvent for plastic binders. However unlike with the hard carbons, a

more environmentally and non-toxic binder including CMC was not explored due to the solubility of the rhodizonate

The choice of electrolyte/solvent was not explored for the rhodizonate and ultimately with the successful cycling of the hard carbons PF6:G2 was chosen due to its good previous results with the hard carbons and as explored later in this chapter a common electrolyte would be needed to make full cells.

4.5 Electrode Overview

This section reports the half-cells used in the study. As previously discussed, half-cells were assembled for each rhodizonate variant. All half-cells used the same electrolyte and binders (PF6:G2 salt/solvent and PTFE/NMP binder/solvent), this then allows a systematic comparison between all half-cells. Overall, 10 half-cells were assembled, 2 of each variant as shown below in table 4.1 below. It is also worth stating that the current density for the galvanostatic cycling of all the half-cells was fixed at 100 mA g^{-1}; this was chosen to allow more cycles to be completed and to determine the stability and performance of the cells at a high cycling rate.

Cell Name	MR/NR/NRR	Synthesis conditions	Electrolyte	Binder	Solvent	Current Density (mA g^{-1})
LJR101	MR	N/A	PF6:G2	PTFE	NMP	100
LJR102	MR	N/A	PF6:G2	PTFE	NMP	100
LJR103	NR	4:1	PF6:G2	PTFE	NMP	100
LJR104	NR	4:1	PF6:G2	PTFE	NMP	100
LJR105	NRR	2:1	PF6:G2	PTFE	NMP	100
LJR106	NRR	2:1	PF6:G2	PTFE	NMP	100
LJR107	NRR	4:1	PF6:G2	PTFE	NMP	100
LJR108	NRR	4:1	PF6:G2	PTFE	NMP	100
LJR109	NR	2:1	PF6:G2	PTFE	NMP	100
LJR110	NR	2:1	PF6:G2	PTFE	NMP	100

Table 4.1: An overview of the rhodizonate electrodes

After the assembly of the half-cells they underwent electrochemical analysis, the two methods used and the data from each are shown below. The two methods were galvanostatic cycling (GC) and cyclic voltammetry (CV); the details of how these techniques operate are discussed in the methods chapter.

4.6 Galvanostatic Cycling analysis (GC)

Once assembled, the half-cells underwent galvanostatic cycling (GC). There are two graphs for each half-cell. First a specific capacity vs. cycle number graph. This shows the sodiation and de-sodiation capacities for each cycle with the coulombic efficiency throughout the 100 cycles. The second graph is a voltage vs. specific capacity graph which focuses on the sodiation and de-sodiation profiles as the voltage changes. As previously discussed in the hard carbon chapter the first cycle is important as this is the first sodiation into the matrix structure. Furthermore, it allows the comparison of the voltage cycles throughout the cycling of the half-cells and the natural degradation of the half-cells throughout the cycling. Similarly, to that of the previous hard carbon chapter, the half-cells are expected to slowly decrease in capacity as the cycling progresses however it is crucial to see how the coulombic efficiency changes also. The decrease in capacity may not necessarily lead to a decrease in the coulombic efficiency. All the half-cells follow the same qualitative behaviour, all are electrochemically similar and vary predominantly or only in the magnitude of capacity. All graphs show up to 100 cycles only, this is to allow visual comparison to be drawn, however many of the half-cells cycled for substantially longer and the half-cells that have passed 100 cycles.

4.6.1 Macro Rhodizonate (MR)

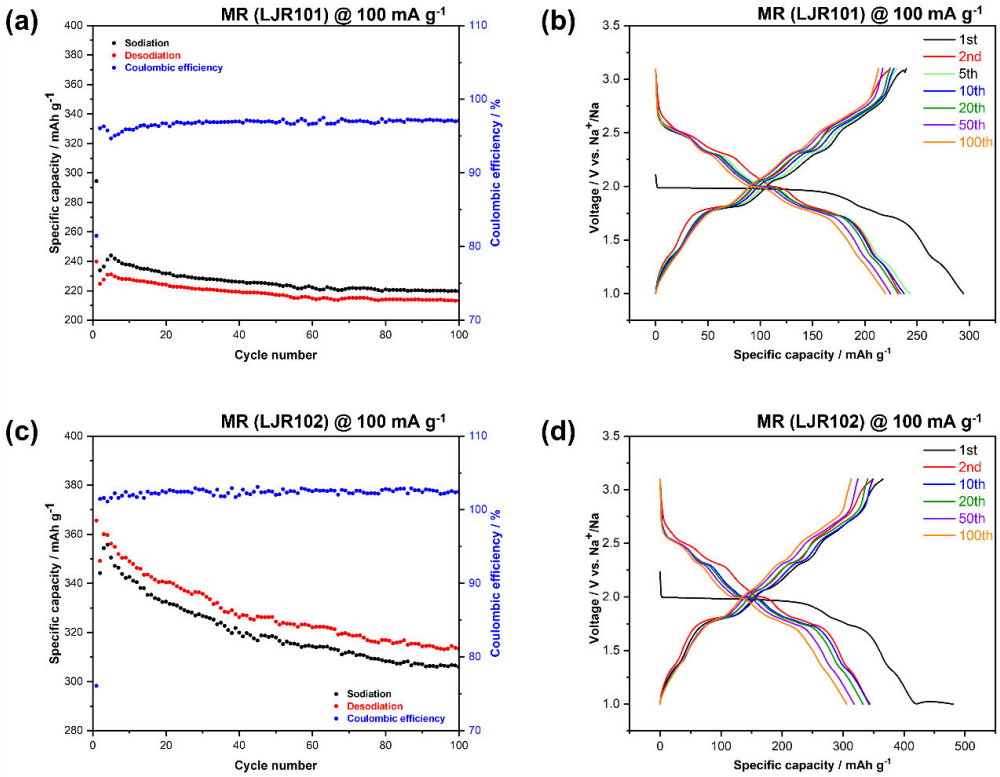

Figure 4.18: MR cycling data (LJR101 a+b, LJR102 c+d)

Figure 4.18 above shows the two macro rhodizonate (MR) half-cells. As shown the half-cells have a first cycle capacity of 294 and 408 mAh g^{-1} respectively. A first cycle capacity loss of 29 and 34% is also seen in graphs b and d. Both have a 100^{th} cycle capacity of 213 mAh g^{-1} and 313 mAh g^{-1}, both complete 191 and 132 cycles and have a capacity retention of 895 and 86% respectively.

4.6.2 Nano Rhodizonate (NR) (2:1 and 4:1)

The following graphs show the cycling data for both NRs, this includes the 2:1 and 4:1 ratios used during the syntheses. There are 4 half-cells in total, each having a capacity/cycle number graph and a voltage/capacity graph.

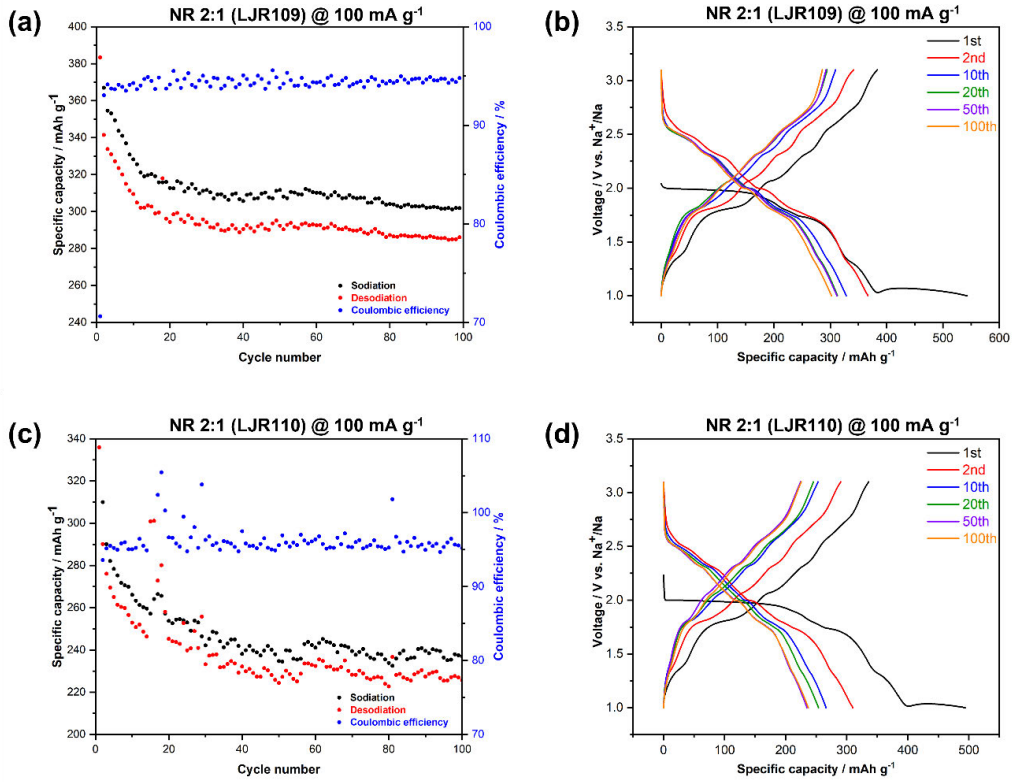

Figure 4.19: NR 2:1 cycling data (LJR109 a + b, LJR110 c + d)

Figure 4.19 above shows the cycling data for NR 2:1. As shown both cells have high first cycle capacities of 543 mAh g^{-1} and 495 mAh g^{-1} for LJR109 and LJR110 respectively, with 1st cycle capacities losses of 29% and 32% also. At 100 cycles, LJR109 achieved a capacity of 301 mAh g^{-1} with a capacity retention of 75% and 237 mAh g^{-1} and a capacity retention of 67% for LJR110.

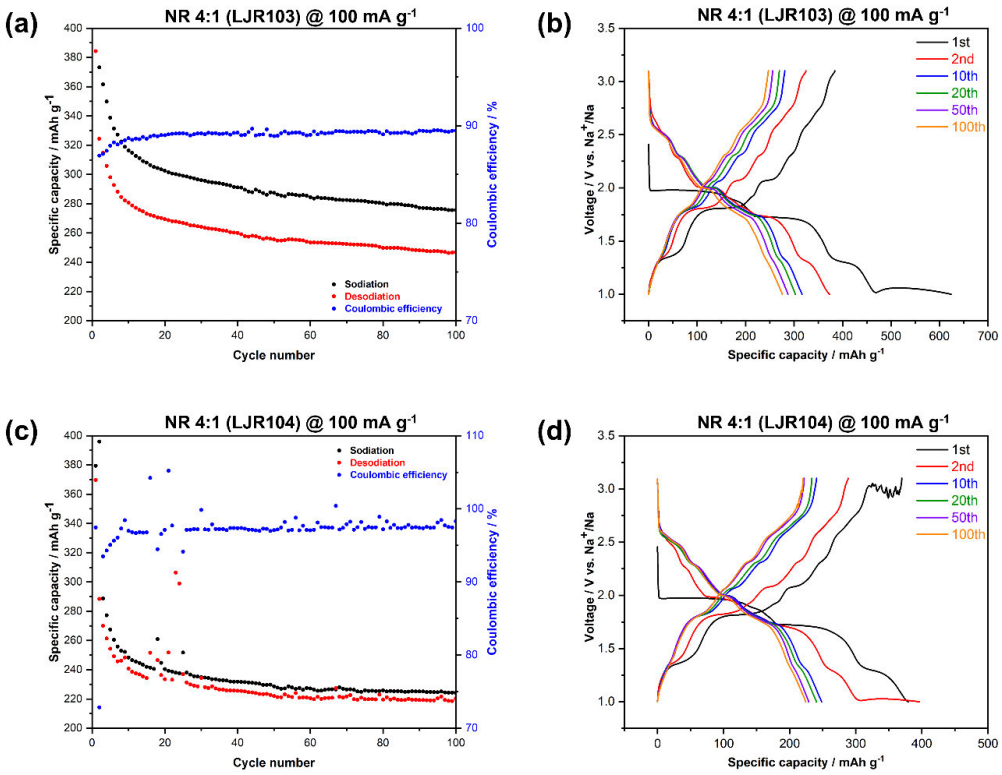

Figure 4.20: NR 4:1 cycling data (LJR103 a+b, LJR104 c+d)

Figure 4.20 above shows the cycling data for NR 4:1. As shown both cells have high first cycle capacities of 624 mAh g^{-1} and 379 mAh g^{-1}, although LJR103 has a significantly higher first cycle of 624 mAh g^{-1}, it is not known why this occurred however it is likely to be due to the formation of the SEI layer during the first cycle. LJR103 then has a first cycle capacity loss of 38%, with LJR104 having a very low 3% first cycle capacity loss. Even though LJR103 had a very high first cycle capacity of 624 mAh g^{-1} compared to LJR104, after 100 cycles both capacities become significantly closer together with capacities of 247 mAh g^{-1} and 220 mAh g^{-1} respectively. Furthermore, the capacity retentions are again closer being 64% and 59% respectively. Finally, both cells cycled 158 and 181 both showing good long term cyclability

Both figures 4.19 and 4.20 show the data for the NR half-cells, using both the 2:1 and 4:1 ratios. When comparing the two sets, both show similar data. All have high first cycle capacities between 379 mAh g^{-1} and 624 mAh g^{-1}. However, whe looking at the 100^{th} cycle capacities LJR109 the NR 2:1 has the highest capacity followed by LJR103 NR 4:1, both NR 2:1s have slightly higher capacities retentions. Although, there are significant differences between the sodiation/desodiation values for each cycle in both

NR 2:1 half-cells. The capacities in both NR 2:1s fluctuate more significantly than either NR 4:1. For long term cycling stability the NR 4:1s have less variation and greater stability so are better for long term cycling.

4.6.3 Nano rhodizonate w/ rGO (NRR) (2:1 and 4:1)

Figures 4.21 and 4.22 below show the cycling data for both NRR half-cells. There are 4 half-cells in total, 8 graphs overall.

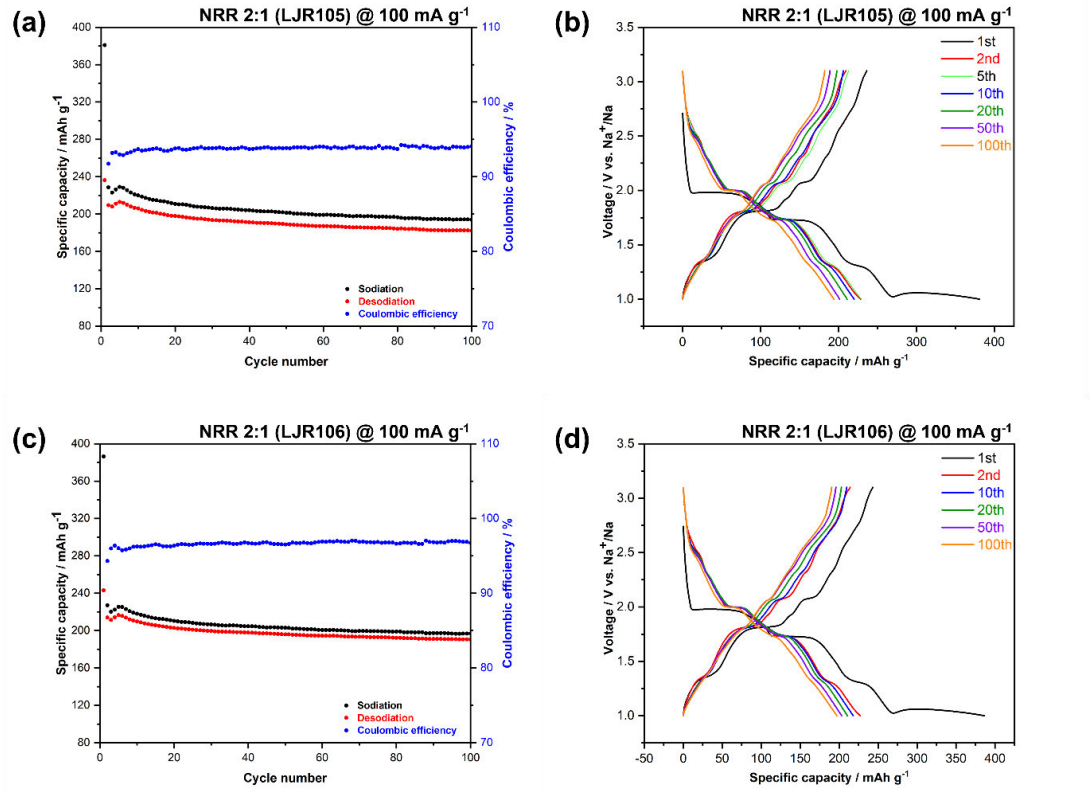

Figure 4.21: Cycling data for NRR 2:1 (LJR105 a + b, LJR106 c + d)

Figure 4.21 above shows the cycling data for both NRR 2:1 half-cells. Both half-cells have a similar first cycle capacity of 381 and 386 mAh g^{-1} with a first cycle capacity loss of 38% and 37% respectively. 100^{th} cycle capacities of 182 and 190 mAh g^{-1} and

a capacity retention of 77 and 78% respectively. Furthermore, both half-cells completed 303 and 299 cycles.

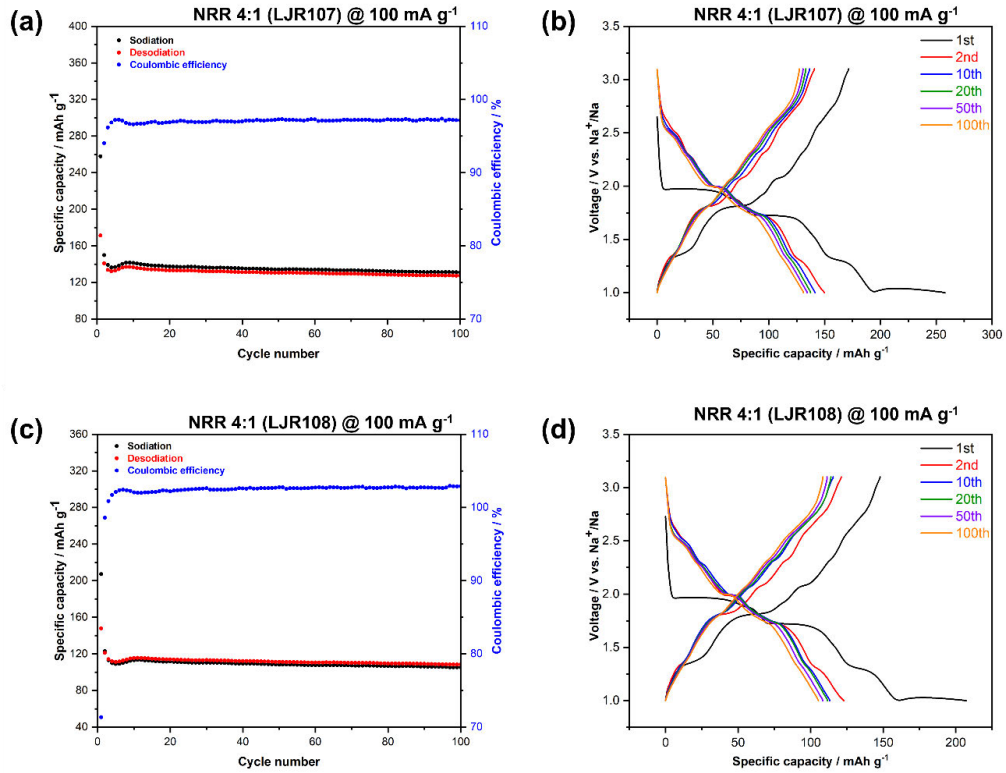

Figure 4.22: NRR 4:1 cycling data (LJR107 a+b, LJR108 c+d)

Figure 4.22 above shows the cycling data for NRR 4:1. Both half-cells have first cycle capacities of 258 mAh g^{-1} and 207 mAh g^{-1} and first cycle capacity losses of 33% and 29% respectively. 100th cycle capacities and 127 mAh g^{-1} 108 mAh g^{-1} with a capacity retention of 74% and 73% respectively. Furthermore, both half-cells cycled over 473 cycles with LJR108 completing 500 cycles; both show very good long term cycling ability.

Both figures 4.21 and 4.22 show NRR syntheses with a difference in the ratios used during each synthesis. When comparing the data, both show very similar results to the other repeat of each half-cell at the same ratio. Both NRR 2:1s have higher first cycle capactities than the NRR 4:1s with higher 100th cycle capacities and higher capacity retention. However, they also have a higher first cycle capacity loss than the NRR 4:1s. Furthermore, all the NRR half-cells show very promising repeatability

throughout the cycle ranges with the differences in sodiation/de-sodiation capacities being very close throughout; there is minimal loss in de-sodiation in every cycle after sodiation. As expected as the cycling continues the capacities gradually decrease over time, with the coulombic efficiencies remaining consistent throughout verifying the stability of all NRR cells. Overall, the NRR 2:1 cells are superior with a higher first cycle capacities and 100th cycle capacities also.

4.6.4 Galvanostatic cycling discussion

Table 4.2 below shows the cycling results of all the half-cells.

Cell Name	MR/NR/ NRR	Synthesis conditions	1st cycle capacity (mAh g^{-1})	1st cycle capacity loss (%)	100th cycle capacity (mAh g^{-1})	Capacity retention at 100th cycle (%)	Number of Cycles
LJR101	MR	N/A	294	29	213	89	191
LJR102	MR	N/A	480	34	313	86	132
LJR109	NR	2:1	543	29	301	75	100
LJR110	NR	2:1	495	32	237	67	102
LJR103	NR	4:1	624	38	247	64	158
LJR104	NR	4:1	379	3	220	59	181
LJR105	NRR	2:1	381	38	182	77	303
LJR106	NRR	2:1	386	37	190	78	299
LJR107	NRR	4:1	258	33	127	74	474
LJR108	NRR	4:1	207	29	108	73	500

Table 4.2: Overview of rhodizonate cycling results

To allow a better overall comparison, cells were compared in terms of the mean capacity between 50 and 100 cycles, this includes standard deviation. The standard deviation can be used to evaluate the degree of cycle to cycle variability.

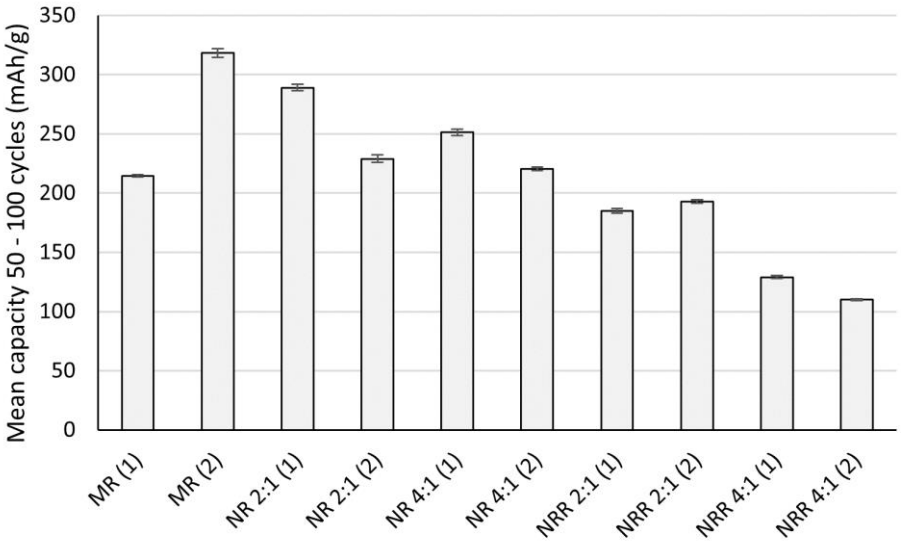

Figure 4.23: Standard deviation of cycles 50-100

Figure 4.23 above, shows the standard deviation of all the rhodizonate half-cells. The range of capacities observed is between 110-316 mAh g^{-1}. For any given cell, there is minimal variation from cycle to cycle as evidenced by the flat sodiation capacities, and low standard deviation in Figure 4.23.

All the half-cells have minimal variation in capacity between each repeat, this shows that all the of the half-cells have good long term cyclability, apart from the MR half-cells which have a large variation in the average capacities between the two MR half-cells.. Across the half-cells the average capacities were between 119-266 mAh g^{-1}, these include 266 mAh g^{-1} for MR, 259 mAh g^{-1} for NR 2:1, 236 mAh g^{-1} for NR 4:1, 189 mAh g^{-1} for NRR 2:1 and 119 mAh g^{-1} for NRR 4:1. This suggests that there is a 10% higher capacity when 2:1 ratio is used compared to the 4:1 ratio for the NR cells. For the NRR cells, a 50% higher capacity when a 2:1 ratio is used compared to the 4:1. Finally, when comparing the better of both NR and NRR, there is a 37% higher capacity using the NR 2:1 compared to NRR 2:1

The recrystallisation techniques were chosen to see if there were any improvements to the cycling performances could be achieved with the reduction in particle size. The inclusion of rGO was also explored to see if the cycling performance could be enhanced further through influencing the recrystallisation process using the rGO

flakes. For cells using the NR syntheses, the higher 4:1 ratio did not offer any benefits compared to the lower 2:1 synthesis ratio. This is the same for the NRR half-cells, again the 2:1 ratio offered higher capacities than the 4:1 counterpart. The inclusion of the rGO had a negative impact overall as the lower capacity NR 4:1 half-cells had a higher capacity compared to the better NRR 2:1 half-cells, 236 mAh g^{-1} vs. 189 mAh g^{-1} for NR 4:1 and NRR 2:1 respectively. From a manufacturing perspective, even though the NR 2:1 offers a 10% higher capacity compared to NR 4:1, the inherent variability must be factored in. Using a lower 2:1 ratio may offer higher capacities but using the higher 4:1 ratio would save resources during the synthesis with a higher concentration and offset the 10% higher capacity from the 2:1 ratio.

Direct comparison to literature is difficult given by the range of cathode compositions, electrolytes and the cycling regimes used. However, work by *Lee et al.* does show long term cycling of a nano rhodizonate half-cell.

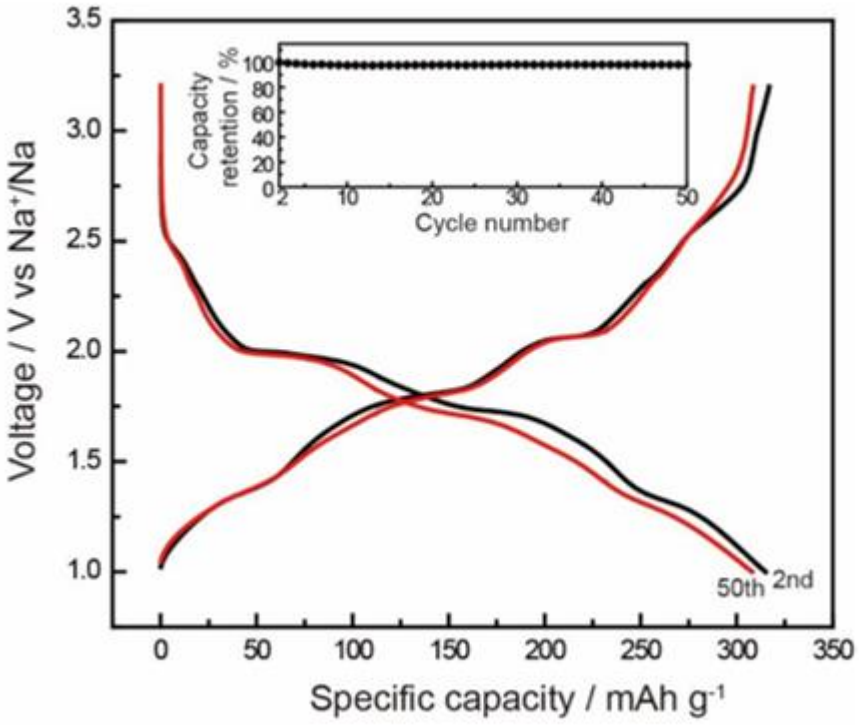

Figure 4.24: Nano rhodizonate cycling data by (Lee et al., 2017). *at 100 mA g^{-1}*

Figure 4.24 above shows cycling data of a nano rhodizonate by *Lee et al.* it is unspecified which concentration ratio is used. However, the current rate applied of

100 mA g^{-1} is the same as the current rate applied to the rhodizonate half-cells in this chapter. When comparing the 2nd and 50th cycles data in figure 4.24 to the 2nd and 50th cycles in this chapter, from the voltage vs. specific capacity graphs above, *Lee et al.* achieved capacities over 300 mAh g^{-1} in both cycles. Most of the half-cells in this chapter do not retain capacities over 300 mAh g^{-1} in either/both the 2nd and 50th cycles. However, a few of the half-cells do offer similar capacities. LJR102, an MR half-cell achieves very similar results as shown in figure 4.18 (d) in both the 2nd and 50th cycles with capacities of 344 mAh g^{-1} and 318 mAh g^{-1} respectively. LJR109 as shown in figure 4.19b, a NR 2:1 cell has 2nd and 50th cycle capacities of 366 mAh g^{-1} and 312 mAh g^{-1} respectfully. LJR103, an NR 4:1 half-cell as shown in figure 4.20 (b) has a 2nd cycle capacity of 373 mAh g^{-1}, however the 50th cycle capacity is below with a capacity of 287 mAh g^{-1}. Finally, none of the NRR half-cells achieved 2nd and 50th cycle capacities above 300 mAh g^{-1}. Regarding capacity retention, LJR102 maintains a capacity retention of 92% between the 2nd and 50th cycles, and LJR109 having a capacity retention of 85%. Overall, these results do seem approximately in line with with *Lee et al.* above in figure 4.24, so this could potentially/cautiously offer beneficial results from this study; however again caution should be taken considering the variability between the half-cells, especially regarding the MR half-cells which have the biggest variation between one another.

So, in conclusion the galvanostatic cycling shows promising results with the macro rhodizonate and both nano rhodizonate syntheses, in line with *Lee et al.* however the inclusion of rGO did not offer any promising results, with the lowest capacities within this study. However, with all cells achieving a minimum 100 cycles there are promising conclusions for the long term cyclability.

4.7 Cyclic Voltammetry

This subchapter focuses on the CV analysis of the multiple types of rhodizonate. CV data will be shown for the MR, NR and NRR There will be 2 graphs for each: one showing all the cycles and then another focusing on three specific cycles. Both NR and NRR are using the 4:1 ratios.

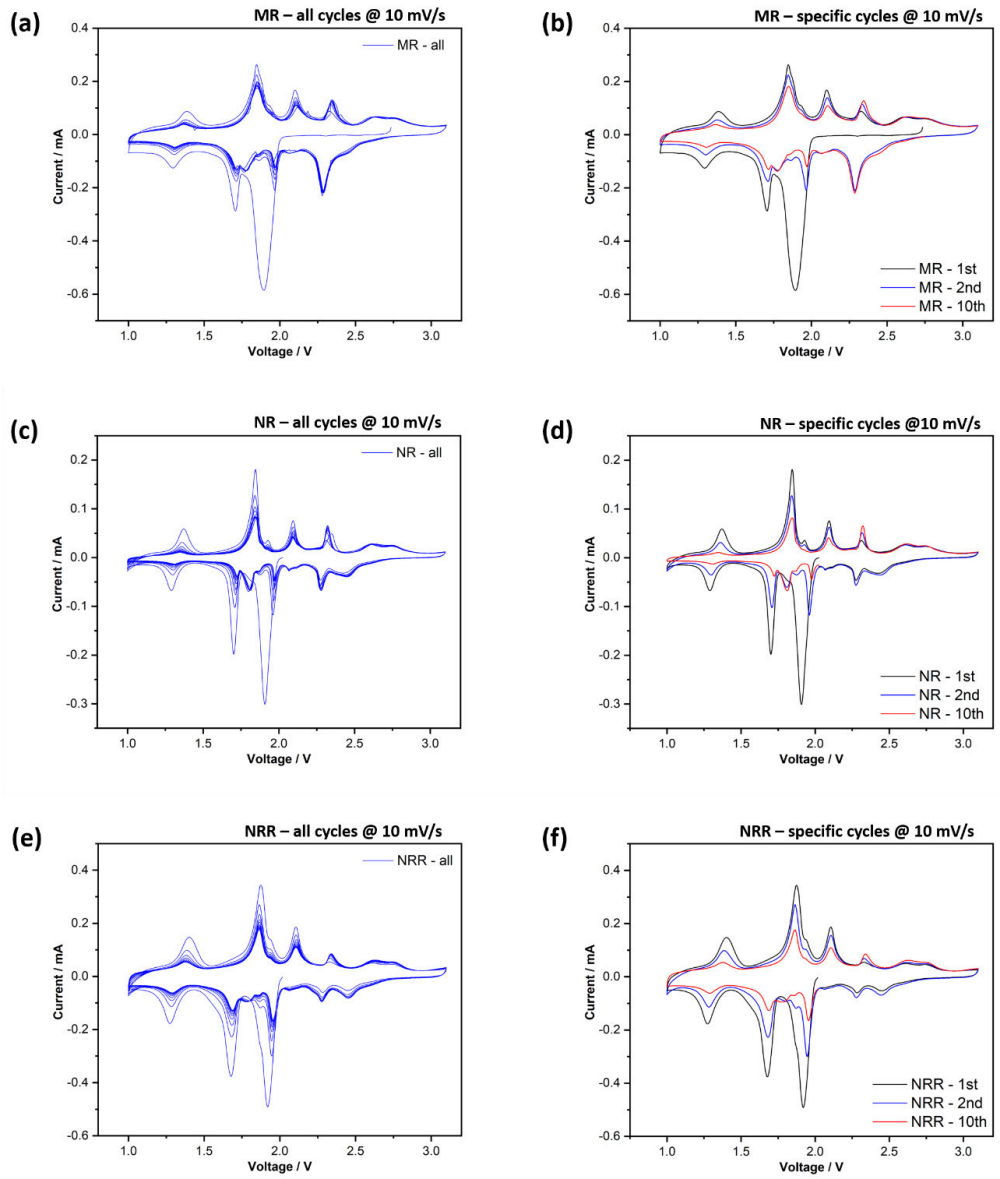

Figure 4.25: CV analysis with all cycles and specific cycles graphs; MR (a + b), NR (c + d) and NRR (in e + f)

The CV data for MR is shown above in figure 4.25 a and b, graph a shows an overlay of all 10 cycles; many of the cycles are very similar having similar voltages to allow for intercalation/de-intercalation with a similar current required. However as seen in figure 4.23b, the 1st cycle requires considerably more current than the 2nd and 10th cycles; this is due to the physical structural resistance which occurs during the first intercalation/de-intercalation. After the 1st cycle the required current drops significantly as the lattice structure has adapted to accommodate the movement of Na^+

ions in and out of the structure. For the MR cells 4 peaks can be seen during both intercalation/de-intercalation for all 10 cycles.

The NR CV data is plotted above in figure 4.25 c and d. The data shows similar results to the MR; both stabilise after the first initial cycle and require less current to allow the inter/de-intercalation to occur. The first cycle requires significantly more current as this is the initial movement of Na+ ions into the lattice structure. From the first cycle, which starts at OCV and decreases in voltage; the sodiation voltages required are always lower that the retrospective de-intercalation voltage for those ions. During de-intercalation the voltage required is higher that the intercalation voltage needed for Na+ ions to be removed from the rhodizonate structure.

Graphs e and f in figure 4.25 above show the the CV data for the NRR rhodizonate. After an initial first cycle which requires a significantly higher current; this reduces throughout the 10 cycles and stabilises. As with MR and NRR, inter/de-intercalation successfully occurs throughout with the intercalation voltage always being slightly lower than the respective voltage for de-intercalation.

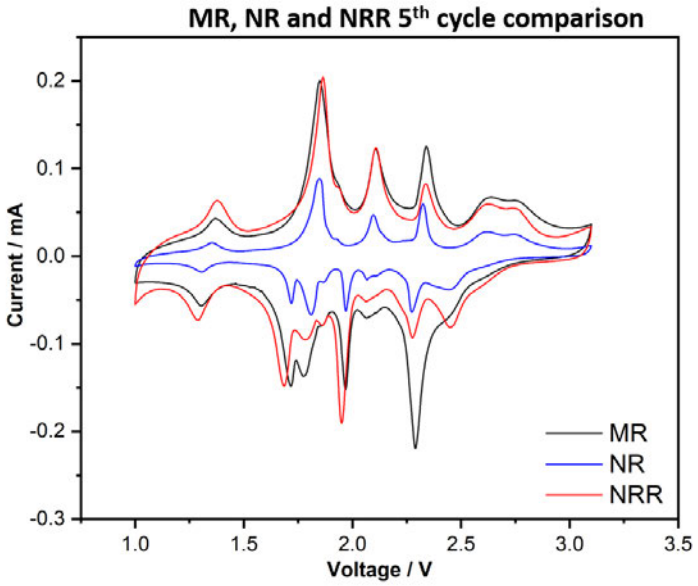

Figure 4.26: CV comparison of MR, NR (4:1) and NRR (4:1) during 5th cycles

Figure 4.26 above shows the 5th cycle CV data for MR, NR and NRR. The three cells show similar intercalation/de-intercalation voltages which shows that Na+ ions are entering the rhodizonate matrix independent of the type of synthesized rhodizonate. There are however differences that can be observed; the most significant of which is

the amount of current required at the voltages to allow the movement of the Na+ ions. The MR and NRR cells require similar amounts of current for the most part; although there are instances where they do vary; the most significant of these occurs at the 2.25 V/2.4 V where the current required is significant larger for the MR. Whilst the NR requires a significantly lower current throughout the whole voltage range.

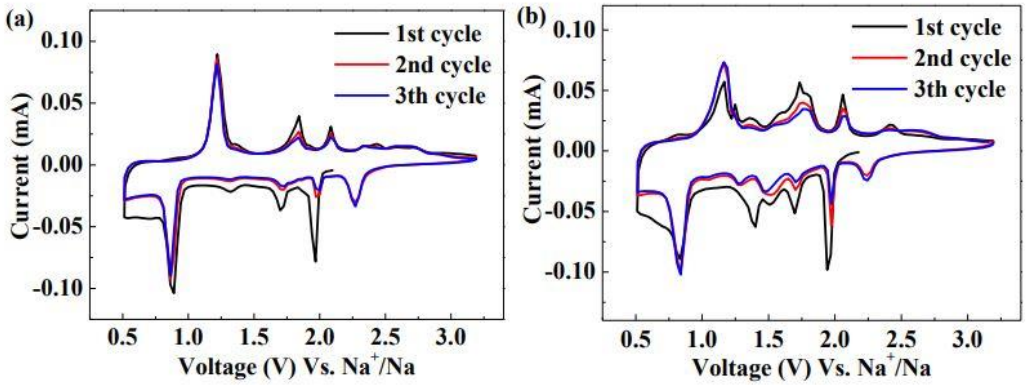

Figure 4.27: CV of NR (left) and NRR (right) at 0.1 mV/s (Tang et al.)

Figure 4.27 above shows CV data from Tang et al. These results are like those above in figure 4.25 c, d, e, f. The left graph in Figure 4.27 is comparable with figure 4.25 c and d both NR, and the right graph in figure 4.27 is comparable to figure 4.25 e and f both NRR. For the NR graphs, the one-electron oxidation processes during the discharging can be seen in both at 1.7, 2.0 and 2.3 V. However, the lowest oxidation voltage is different, *Tang el al.* has it at 0.8 V, whilst figure 4.19 c and d show 1.3 V. The difference in voltage can be associated to the kinetic barriers that occur during the phase transformations when the oxidation process occurs. These kinetic barriers are caused by a slight variation in size and conductivity between the two rhodizonates. When comparing both NRR CV graphs in figure 4.13 e and f, and figure 4.27 right, there are many similarities, notably at the 1.5 V oxidation point, a strain occurs on the rhodizonate due to the formation of hydrogen bonds during the Na^+ intercalation which in turn causes a lag in potential *(Tang et al.)* However, one difference can be observed at the the top voltage end at 2.4/2.6 V discharge/charge where an additional peak can be observed. This could potentially indicate that there is another phase transformation occurring, however more work would need to be carried out to verify this.

To conclude, the CV analysis showed that the 3 cells cycled all successfully throughout the 10 cycles. All showing similar voltage sodiation/de-sodiation voltages; however, the current required varied quite significantly. This could be related to the internal resistance of the framework structure as over time the 3 cells require less current for the 10^{th} cycles than the 1^{st} cycles. The initial current required will potentially be larger due to the first sodiation/de-sodiation from entering the framework. Furthermore, verification of the additional peak observed in the NRR could also be scrutinised.

4.8 Closure

This chapter set out to explore the manipulation of the particle size of sodium rhodizonate. The focus was on reducing the particle size by a reverse crystallisation reaction. The inclusion of rGO during the recrystallisation was also included to see if any potential further benefits could be achieved. Multiple ratios for the nano rhodizonates were explored. The addition of rGO proved to be unfavourable; no capacity benefits were achieved. However, with the inclusion of rGO, the rGO becomes part of the measured mass of the electrode, there could potentially be less rhodizonate in the NRR cells as rGO is included in the overall mass.

Overall, 2 ratios were chosen for the nano syntheses, these being 2:1 and 4:1, with further nano rhodizonates with rGO also included all of which were compared to an un-synthesised macro variant. The resultant powders were characterised through XRD and SEM analysis. No differences were seen with the XRD, and the inclusion of rGO was not seen, this may be due to the amount of rGO used in the syntheses. SEM analysis on the other hand, showed clear differences in particle sizes between the macro and nano variants, with the rGO being seen in the rGO variants. Electrochemical characterisation was undertaken through half-cells to analyse the cycling performances of the powders through galvanostatic cycling and cyclic voltammetry. The GC showed that overall, the MR variant offered the highest capacities, however caution must be taken as the average capacities of the two MR

cells were significant from one another. However, with regards to the NRR half-cells, both 2:1 NR and NRR outperformed the 4:1 ratio equivalent. Furthermore, the NR 4:1 outperformed the NRR 2:1 also. CV analysis showed similar voltages for the sodiation/desodiation, however the currents required with the NR variant requiring the least throughout all sodiation/desodiation voltages compared to the MR and NRR.

From a manufacturing perspective, the required steps to synthesise the NR and NRR compared to minimal changes to MR raise questions to the cost/capacity cycling results with the MR offering the highest cycling performances. However, as previously stated the large difference in capacities between the 2 MR half-cells does need to be considered. Furthermore, does the benefit of using the 2:1 ratio in NR justify the increase in manufacturing costs as it is the lower of the 2 ratios with only a 10% increase in capacity observed. The additional costs of including rGO in NRR ratios is not viable as there are no capacity gains achieved.

To close, the manipulation of the particle size through a recrystallisation does have an impact on the cycling performances of rhodizonate, although the evidence is mixed. The inclusion of rGO shows no benefits with regards to capacity. The NR 2:1 half-cells showed the largest differences compared to the other NR and NRR half-cells.

The next chapter will explore the the assembly of full-cells, taking hard carbon anodes from the previous chapter and combining them to nano rhodizonates from this chapter and analysing the cycling performances through galvanostatic cycling.

Part 5

Hard Carbon – Sodium Rhodizonate Full Cell

5.1 Introduction

The last two previous chapters have shown the development of successful hard carbon anodes and sodium rhodizonate. This chapter investigates developing a full-cell, combining both hard carbon anodes and rhodizonate cathodes. It should be noted that this was novel and exploratory work that has not been attempted previously in literature.

Half-cells are assembled with the electrode being tested on one side against a source of sodium to allow the electrode to be tested without capacity limitations. Full-cells have both an anode and a cathode without a specific source of sodium, thus one of the electrodes needs to be pre-sodiated before the full-cell is assembled. Initially, a half-cell is assembled with the chosen electrode, pre-cycled to form the SEI layer and then ending the cycling at the required voltage for the electrode to be sodiated. Once the chosen electrode is in a sodiated state, it is then disassembled to allow the other electrode to be placed as the counter electrode to form the full-cell.

In the work below two hard carbon anodes were chosen with two rhodizonate cathodes. HC-C2 and HCGO-C2 following the second pyrolysis conditions were used. Regarding the rhodizonate cathodes, NR (4:1) and NRR (4:1) were chosen, both using the 4:1 synthesis method. To enable a full-cell to be successfully assembled a common electrolyte/solvent is required, for this $NaPF_6$/G2 which has been proven to work with both sets of electrodes was chosen. The hard carbon anodes were chosen to be pre-sodiated as a longer period had been spent developing the hard carbon anodes compared to the rhodizonate cathodes at the time of the full-cell development.

Galvanostatic cycling was the chosen technique to test the full-cells through cycling the full-cell between a set voltage window. During the presodiation the current density was chosen to be 30 mA g^{-1} this was the commonly used current density during the preliminary refinement of the hard carbon anodes. For the final full-cell cycling the current density was raised to 40 mA g^{-1} as this was the commonly used current density for the rhodizonate cells.

5.2 Full-cell assembly

Two full-cells were assembled as shown below in figure 5.1.

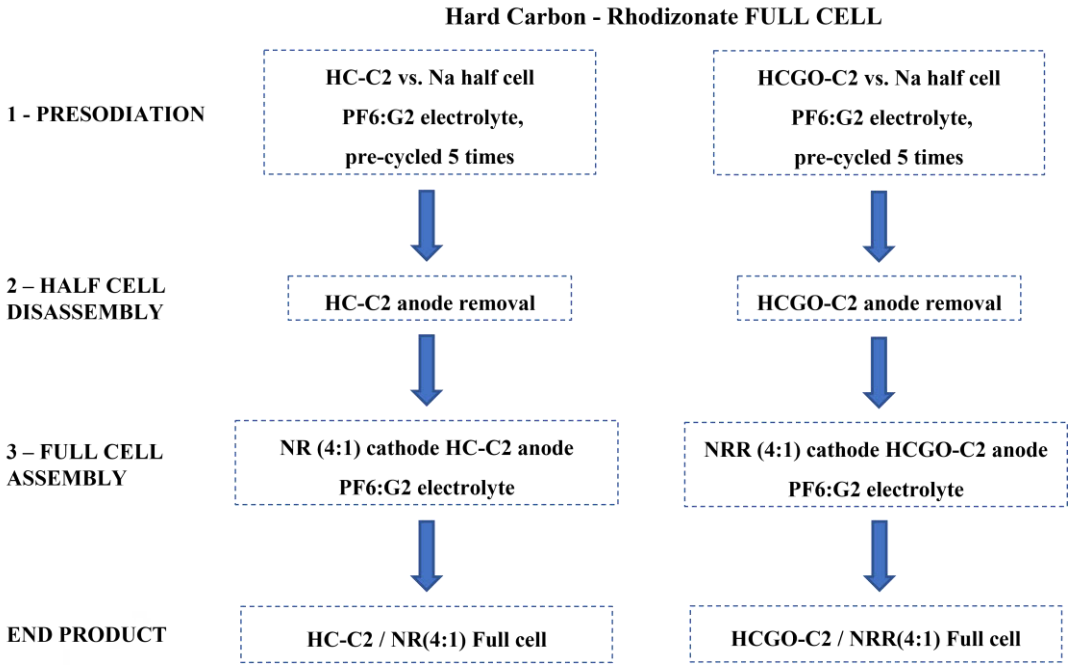

Figure 5.1: Flowchart showing the assembly of a hard carbon – rhodizonate full cell

Figure 5.1 above shows the assembly process of the two full-cells, as shown each hard carbon anode was pre-cycled 5 times before full-cell assembly. The chosen current density was 30 mA g^{-1}, The electrolyte/solvent remained the same throughout the presodiation and full-cell assembly which was $NaPF_6$/G2.

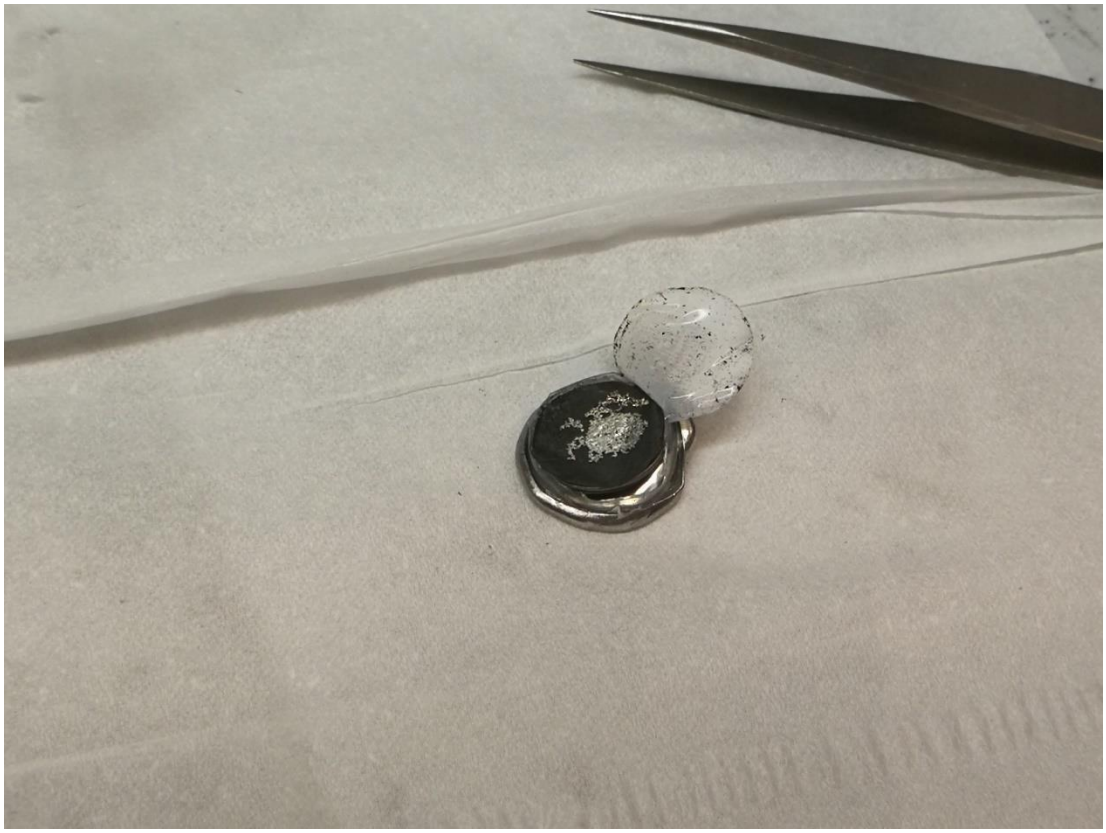

Figure 5.2: Example of a presodiated hard carbon anode after half-cell disassembly

Figure 5.2 above shows presodiated hard carbon anode which has been pre-cycled. As discussed in the introduction, to enable successful presodiation, the half-cell needs to be stopped at a sodiated voltage. This is shown above as Sodium metal can be seen on the surface of the hard carbon anode. The sodiated anode is then placed into another coin-cell with the rhodizonate cathode to create the full-cell.

5.3 Galvanostatic cycling

The two full-cells once assembled underwent galvanostatic cycling. For each full-cell two graphs are given. The first is a specific capacity vs. cycle number. This graph shows the sodiation/desodiation of the anodes and cathodes during the cycling in the attempt to reach 100 cycles and the coulombic efficiencies of each. The second graph shows voltage vs. specific capacity, this focuses on the sodiation profiles during each cycle as the sodium-ions flow between both electrodes. As per the previous 2 chapters, over time, it is expected to see the capacity of each half-cell slowly decrease in capacity however it is important to see how the coulombic efficiency changes also. The decrease in capacity over time may not cause a decrease in the coulombic efficiency.

5.3.1 Full-cell cycling results

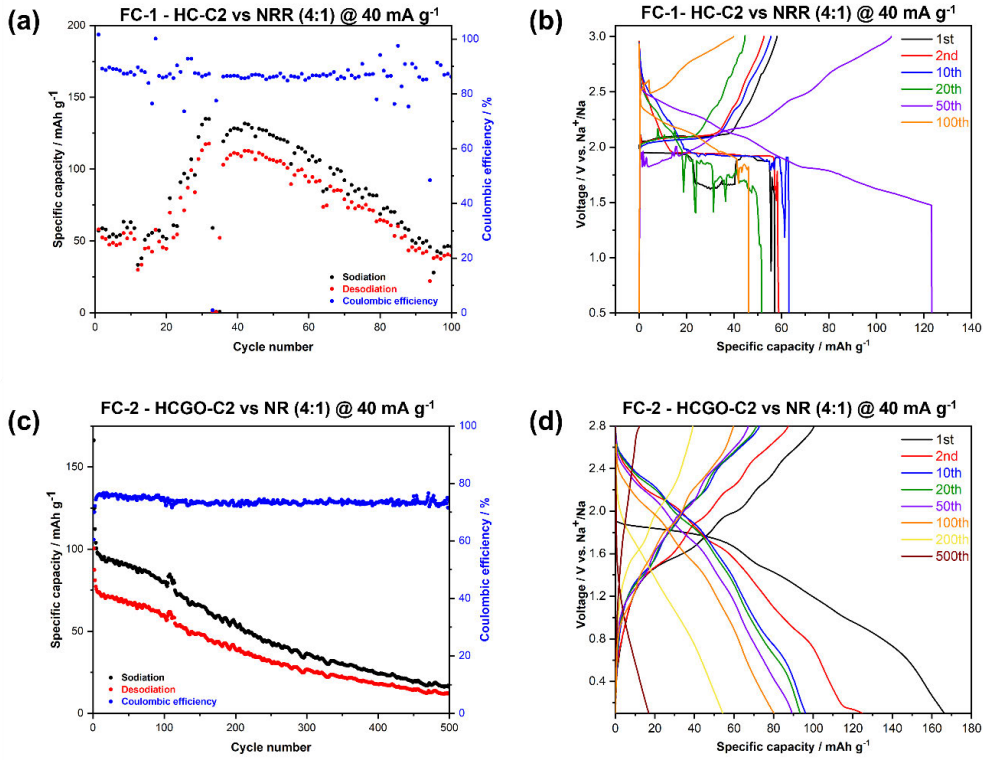

Figure 5.3: Cycling data for FC-1 (a + b) and FC-2 (c + d)

Cell Name	Anode	Cathode	Electrolyte	Binders (Anode/Cathode)	Solvents (Anode/cathode)	Current Density (mA g^{-1})
FC-1	HC-C2	NRR (4:1)	PF6:G2	CMC/PTFE	water/NMP	40
FC-2	HCGO-C2	NR (4:1)	PF6:G2	CMC/PTFE	water/NMP	40

Cell Name	Anode	Cathode	First cycle capacity (mAh g^{-1})	Final cycle capacity (mAh g^{-1})	First cycle capacity loss (%)	Capacity retention (%)	Coulombic Efficiency (%)	Number of cycles
FC-1	HC-C2	NRR (4:1)	57	46	-2	81	86	100
FC-2	HCGO-C2	NR (4:1)	166	17	40	10	74	500

Table 5.1: Overview of cell conditions and galvanostatic cycling data

5.3.2 Galvanostatic cycling discussion

FC-1 cycling data is shown in figure 5.3 a and b, the cell achieves 100 cycles however there is clearly something detrimental occurring. The cycling data shows there is instability within the cell as the capacity varies significantly throughout. However, the coulombic efficiency remains stable throughout at ~86%. The significant capacity variation could potentially be occurring due to contact issues within the cell, between the two electrodes. The voltage vs. specific capacity graph in 5.3 b emphasises the issues due to the unstable voltage profiles, there are sudden drops occurring below 1.5 V. At the top end of the voltage range similar voltage profiles are with the rhodizonate half cells as plateaus can be seen, these occur during sodiation/desodiation into the rhodizonate. Overall, the full cell does cycle however the final capacity of 46 mAh g^{-1} is not realistically viable, the final capacity is low compared to the capacities offered independently by the anodes and cathodes.

FC-2 conversely is very stable in comparison. There is a slow but continuous decline in capacity throughout the cycling which is to be expected when cycling a cell; expected structural damage of both electrodes caused through repeated intercalation/de-intercalation over time. The coulombic efficiency remains stable throughout at 74% with the cell successfully completing 500 cycles. The voltage vs specific capacity graph in figure 5.3 d, shows successful cycling throughout the voltage range. Similar plateaus can be seen for both electrodes, unlike in FC-1 where the lower voltage range had sudden drops. However, there is a large first cycle capacity loss of 40%, potentially due to SEI formation and the intercalation of the rhodizonate

cathode for the first time (the hard carbon SEI layer had already formed during the pre-sodiating process). The following cycles do then stabilise with repeatable voltage profiles with a continued loss of capacity. This shows that the cycling of the cell is stable; unlike what was seen with FC-1. Although having a capacity retention of only 10% after 500 cycles indicates that for long term cycling this full cell, is not viable. This low capacity could partially be attributed to the multiple stages in the assembly of the full-cell, potential issues including the disassembly and removal of the pre-sodiated anode, including delamination during the removal of the half-cell separator.

5.4 Closure

This chapter set out to explore if full-cells could successfully be assembled and cycled using anodes and cathodes from the previous two chapters.

Overall, two full cells were successfully created and cycled, with two hard carbon variants HC-C2, HCGO-C2 and two rhodizonate variants NR 4:1 and NRR 4:1. The electrochemical cycling results were poor compared to the separate half-cells for each variant individually as previously cycled in both chapters. Nevertheless, the proof of concept and one of the main aims of the research was successfully achieved, both anodes and cathodes were synthesised independently of one another and then when combined both electrodes were compatible with one another.

It is also worth raising that from a manufacturing perspective, the process of creating the full-cells is complicated as multiple stages are required to be successful before the final assembly of the full-cell can be completed. Many potential difficulties may occur compared to half-cells; these can include the alignment of both electrodes to one another, damage from tweezers when assembling. Furthermore, half-cells have an excess of sodium which in turn can mask any side reactions that may use up the sodium. Interactions between the anode and cathode which cannot be identified at the half-cell stage. The capacities of the electrodes may not be balanced either making the full-cell less efficient capacity wise. Industrial routes however for these processes may remove some of the issues that are observed in laboratory processing. This includes initial preconditioning of one of the electrodes through presodiation cycling and

disassembly of the half-cell. Also, a compatible electrolyte/solvent for both needs to be chosen. FC-1 was unsuccessful during cycling, this may be down to chance and requires more cells to validate. However, FC-2 shows the potential to assemble a full-cell through the synthesis methods above does show promise for the future.

To close, it is very promising to see that both hard carbon and sodium rhodizonate can successfully combine to create a full-cell. Both hard carbon anodes chosen used different synthesis methods, similarly with the rhodizonate cathodes too. Even though the final capacities were not realistically viable for real world conditions; this novel, never seen in literature has been successful and shows promise to the future of not just hard carbon anodes or rhodizonate cathodes individually. They are compatible with one another when combined to assemble a full-cell. More work is needed to improve the performance and capacity matching so that the cells can reach their full potential.

Part 6

Conclusions and Future Recommendations

The work in this thesis has shown that sodium-ion electrodes can be synthesised and successfully cycled using both raw carbohydrates and sodium rhodizonate without the requirement of rare metals. Both electrodes were also used effectively together in a full-cell.

The first research chapter set out to explore the synthesis of hard carbon; looking into the manipulation of the ramp rates during the pyrolysis stage of the synthesis. A key temperature range was focused on in which a rapid change in mass occurs to determine if slowing the ramp rate through this temperature range had any impacts on the outcomes. Graphene oxide was an additive included in the synthesis as it has been studied in literature with promising results.

Three ramp rates were chosen, an undefined and two controlled ramp rates, both with and without graphene oxide. Characterisation of the powders showed minimal differences through XRD and XPS analysis. SEM showed slight differences between the HC and HCGO, specifically the topography of the powders where slight differences were observed. Electrochemical characterisation was then undertaken through half-cell to analyse the cycling performances of the synthesised materials. Both galvanostatic cycling and cyclic voltammetry were used. GC analysis showed that the inclusion of GO during the synthesis showed a greater capacity than those without. An increase of 25% was observed that was in line with literature. Although due to great variability of the cells caution must be taken. CV analysis showed differences between the HC and HCGO regarding the amount of current needing to be applied, it is not clear why this was however it could be hypothesised that the differences in structure may be the reason behind this. Thus, influencing the ramp rate does have an impact on the cycling performances of hard carbons. The inclusion of GO had positive benefits increasing capacities. Ultimately, -C1 showed the largest differences between the hard carbons.

The second research chapter set out to explore the sodium rhodizonate as a cathode material for sodium-ion batteries. The focus was on the manipulation of the sodium rhodizonate particle size and then the inclusion of rGO during the recrystallisation. Unfortunately, the inclusion of rGO during the recrystallisation synthesis proved to be unfavourable as no cycling benefits were seen. XRD characterisation saw no differences between the variants, and the inclusion of rGO was not seen; this may

likely be due to the amount of rGO used in the synthesis. SEM analysis showed that there were differences in particle sizes after the syntheses and the inclusion of rGO was seen. The GC showed that overall, the MR variant offered the highest capacities, however caution should be taken as the capacities of the two MR cells were significant from one another. However, with regards to the NRR half-cells, both 2:1 NR and NRR outperformed the 4:1 ratio equivalent. Furthermore, the NR 4:1 outperformed the NRR 2:1 also. Thus, influencing the particle size of sodium rhodizonate does affect the cycling performances of sodium rhodizonate, however the inclusion of rGO shows no benefits.

The final research chapter focused on seeing if full-cells could successfully be assembled and cycled using the hard carbon anodes and sodium rhodizonate cathodes from the previous chapters. Two full-cells were successfully assembled and cycled. The galvanostatic cycling results were poor compared to the individual half-cells of each electrode. It was also raised that there could potentially be many difficulties in the fabrication of the full-cells due to the multiple complex stages involved. Although, it is shows potential that both hard carbon anodes and sodium rhodizonate cathodes can be combined to assemble a full-cell. The cycling capacities seen in this work are unviable; the novel concept of combining these hard carbons and rhodizonates together shows promise for the future.

Looking forward, both electrodes show they offer the ability to be used on a larger scale; and that continued research and development of both hard carbon and sodium rhodizonate electrodes is valuable. Potential improvements with the hard carbon anodes could investigate the concentration of GO used and continue researching various ramp rates to see if the benefits of both a controlled ramp rate and the inclusion of GO can be combined to achieve increased cycling benefits, as shown electrolytes binders can play a significant role within the cell. There are a wide variety of alternate binders and electrolytes that can be tested with hard carbon, this can also be said for the sodium rhodizonate cathodes. Regarding the sodium rhodizonate, there is the potential for other concentration ratios to be explored and compared to the ones used in this thesis; and as previously said the influence of rGO can be further explored. As two full-cells were successfully assembled, there is the potential for significant upscaling to be undertaken creating larger cells and even the opportunity to test the full-cells as supercapacitors also. The future for both to contribute to sodium-ion

batteries looks extremely promising and hopefully this thesis has shown the significant potential available through both hard carbons and sodium rhodizonate.

Hard carbon anodes are still being studied today as they have a large variety of precursors, continued work is still researching waste biomasses and pyrolysis techniques and temperatures are still be explored. Specifically work by (Jin et al., 2023) that shows the pyrolysis temperature ranges between 1200-1400 °C are still being explored and are achieving capacities of over 300 mAh g^{-1}. Sodium rhodizonate is also still being explored through the development of free-standing electrodes focusing on binder-free electrodes to see improvements at high capacities of 231 mAh g^{-1} at 1,000 mA g^{-1} which offers the potential to be commercially viable in the future. (Jin et al., 2023)

Chapter 7

References

ABRAHAM, K. (1982). Intercalation positive electrodes for rechargeable sodium cells. *Solid State Ionics*, *7*(3). https://doi.org/10.1016/0167-2738(82)90051-0

Adelhelm, P., Hartmann, P., Bender, C. L., Busche, M., Eufinger, C., & Janek, J. (2015). From lithium to sodium: cell chemistry of room temperature sodium–air and sodium–sulfur batteries. *Beilstein Journal of Nanotechnology*, *6*. https://doi.org/10.3762/bjnano.6.105

Alcántara, R., Jiménez-Mateos, J. M., Lavela, P., & Tirado, J. L. (2001). Carbon black: a promising electrode material for sodium-ion batteries. *Electrochemistry Communications*, *3*(11). https://doi.org/10.1016/S1388-2481(01)00244-2

Ali, G., Lee, J., Oh, S. H., Cho, B. W., Nam, K.-W., & Chung, K. Y. (2016). Investigation of the Na Intercalation Mechanism into Nanosized V_2O_5/C Composite Cathode Material for Na-Ion Batteries. *ACS Applied Materials & Interfaces*, *8*(9). https://doi.org/10.1021/acsami.5b11954

Aurbach, D., Markovsky, B., Shechter, A., Ein-Eli, Y., & Cohen, H. (1996). A Comparative Study of Synthetic Graphite and Li Electrodes in Electrolyte Solutions Based on Ethylene Carbonate-Dimethyl Carbonate Mixtures. *Journal of The Electrochemical Society*, *143*(12). https://doi.org/10.1149/1.1837300

Ban, L. L., Crawford, D., & Marsh, H. (1975). Lattice-resolution electron microscopy in structural studies of non-graphitizing carbons from polyvinylidene chloride (PVDC). *Journal of Applied Crystallography*, *8*(4). https://doi.org/10.1107/S0021889875010904

Bianco, A., Cheng, H.-M., Enoki, T., Gogotsi, Y., Hurt, R. H., Koratkar, N., Kyotani, T., Monthioux, M., Park, C. R., Tascon, J. M. D., & Zhang, J. (2013). All in the graphene family – A recommended nomenclature for two-dimensional carbon materials. *Carbon*, *65*. https://doi.org/10.1016/j.carbon.2013.08.038

Blomgren, G. E. (2017). The Development and Future of Lithium Ion Batteries. *Journal of The Electrochemical Society*, *164*(1). https://doi.org/10.1149/2.0251701jes

Bommier, C., & Ji, X. (2018). Electrolytes, SEI Formation, and Binders: A Review of Nonelectrode Factors for Sodium-Ion Battery Anodes. *Small*, *14*(16). https://doi.org/10.1002/smll.201703576

Bommier, C., Surta, T. W., Dolgos, M., & Ji, X. (2015). New Mechanistic Insights on Na-Ion Storage in Nongraphitizable Carbon. *Nano Letters*, *15*(9). https://doi.org/10.1021/acs.nanolett.5b01969

Buiel, E., & Dahn, J. R. (1999). Li-insertion in hard carbon anode materials for Li-ion batteries. *Electrochimica Acta*, *45*(1), 121–130. https://doi.org/10.1016/S0013-4686(99)00198-X

Cai, Z. P., Liang, Y., Li, W. S., Xing, L. D., & Liao, Y. H. (2009). Preparation and performances of LiFePO4 cathode in aqueous solvent with polyacrylic acid as a binder. *Journal of Power Sources*, *189*(1). https://doi.org/10.1016/j.jpowsour.2008.10.040

Carneiro, P., Morais, S., & Pereira, M. C. (2019). Nanomaterials towards Biosensing of Alzheimer's Disease Biomarkers. *Nanomaterials*, *9*(12). https://doi.org/10.3390/nano9121663

Chagas, L. G., Jeong, S., Hasa, I., & Passerini, S. (2019). Ionic Liquid-Based Electrolytes for Sodium-Ion Batteries: Tuning Properties To Enhance the Electrochemical Performance of Manganese-Based Layered Oxide Cathode. *ACS Applied Materials & Interfaces*, *11*(25). https://doi.org/10.1021/acsami.9b03813

Chihara, K., Chujo, N., Kitajou, A., & Okada, S. (2013). Cathode properties of Na2C6O6 for sodium-ion batteries. *Electrochimica Acta*, *110*. https://doi.org/10.1016/j.electacta.2013.04.100

Crystallite growth in graphitizing and non-graphitizing carbons. (1951). *Proceedings of the Royal Society of London. Series A. Mathematical and Physical Sciences*, *209*(1097). https://doi.org/10.1098/rspa.1951.0197

Dahbi, M., Yabuuchi, N., Kubota, K., Tokiwa, K., & Komaba, S. (2014). Negative electrodes for Na-ion batteries. *Physical Chemistry Chemical Physics*, *16*(29). https://doi.org/10.1039/c4cp00826j

Dahn, J. R., Xing, W., & Gao, Y. (1997a). The “falling cards model” for the structure of microporous carbons. *Carbon*, *35*(6). https://doi.org/10.1016/S0008-6223(97)00037-7

Dahn, J. R., Xing, W., & Gao, Y. (1997b). The “falling cards model” for the structure of microporous carbons. *Carbon*, *35*(6). https://doi.org/10.1016/S0008-6223(97)00037-7

Dahn, J. R., Zheng, T., Liu, Y., & Xue, J. S. (1995). Mechanisms for Lithium Insertion in Carbonaceous Materials. *Science*, *270*(5236). https://doi.org/10.1126/science.270.5236.590

Dai, Z., Mani, U., Tan, H. T., & Yan, Q. (2017). Advanced Cathode Materials for Sodium-Ion Batteries: What Determines Our Choices? *Small Methods*, *1*(5). https://doi.org/10.1002/smtd.201700098

De La Llave, E., Borgel, V., Park, K. J., Hwang, J. Y., Sun, Y. K., Hartmann, P., Chesneau, F. F., & Aurbach, D. (2016). Comparison between Na-Ion and Li-Ion Cells: Understanding the Critical Role of the Cathodes Stability and the Anodes Pretreatment on the Cells Behavior. *ACS Applied Materials and Interfaces*, *8*(3), 1867–1875. https://doi.org/10.1021/acsami.5b09835

Ding, J., Wang, H., Li, Z., Kohandehghan, A., Cui, K., Xu, Z., Zahiri, B., Tan, X., Lotfabad, E. M., Olsen, B. C., & Mitlin, D. (2013). Carbon Nanosheet Frameworks Derived from Peat Moss as High Performance Sodium Ion Battery Anodes. *ACS Nano*, *7*(12). https://doi.org/10.1021/nn404640c

Dinnebier, R. E., Nuss, H., & Jansen, M. (2005). Disodium rhodizonate: a powder diffraction study. *Acta Crystallographica Section E Structure Reports Online*, *61*(10). https://doi.org/10.1107/S1600536805030552

El Moctar, I., Ni, Q., Bai, Y., Wu, F., & Wu, C. (2018). Hard carbon anode materials for sodium-ion batteries. *Functional Materials Letters*, *11*(06). https://doi.org/10.1142/S1793604718300037

Fergus, J. W. (2010). Recent developments in cathode materials for lithium ion batteries. *Journal of Power Sources*, *195*(4). https://doi.org/10.1016/j.jpowsour.2009.08.089

Franklin, R. E. (1951). The structure of graphitic carbons. *Acta Crystallographica*, *4*(3). https://doi.org/10.1107/S0365110X51000842

GE, P. (1988). Electrochemical intercalation of sodium in graphite. *Solid State Ionics*, *28–30*. https://doi.org/10.1016/0167-2738(88)90351-7

Gil-Alana, L. A., & Monge, M. (2019). Lithium: Production and estimated consumption. Evidence of persistence. *Resources Policy*, *60*. https://doi.org/10.1016/j.resourpol.2019.01.006

Grey, C. P., & Tarascon, J. M. (2017). Sustainability and in situ monitoring in battery development. *Nature Materials*, *16*(1). https://doi.org/10.1038/nmat4777

Harris, P. J. F. (2005). New Perspectives on the Structure of Graphitic Carbons. *Critical Reviews in Solid State and Materials Sciences*, *30*(4). https://doi.org/10.1080/10408430500406265

Harris, P. J. F. (2013). Fullerene-like models for microporous carbon. *Journal of Materials Science*, *48*(2). https://doi.org/10.1007/s10853-012-6788-1

Helfferich, F. G. (1985). Principles of adsorption & adsorption processes, by D. M. Ruthven, John Wiley & Sons, 1984, xxiv + 433 pp. *AIChE Journal*, *31*(3). https://doi.org/10.1002/aic.690310335

Hong, K., Qie, L., Zeng, R., Yi, Z., Zhang, W., Wang, D., Yin, W., Wu, C., Fan, Q., Zhang, W., & Huang, Y. (2014). Biomass derived hard carbon used as a high performance anode material for sodium ion batteries. *Journal of Materials Chemistry A*, *2*(32). https://doi.org/10.1039/C4TA02068E

Hou, H., Qiu, X., Wei, W., Zhang, Y., & Ji, X. (2017). Carbon Anode Materials for Advanced Sodium-Ion Batteries. *Advanced Energy Materials*, *7*(24). https://doi.org/10.1002/aenm.201602898

Hwang, J. Y., Myung, S. T., & Sun, Y. K. (2017). Sodium-ion batteries: Present and future. *Chemical Society Reviews*, *46*(12), 3529–3614. https://doi.org/10.1039/c6cs00776g

Hwang, J.-Y., Myung, S.-T., & Sun, Y.-K. (2017). Sodium-ion batteries: present and future. *Chemical Society Reviews*, *46*(12). https://doi.org/10.1039/C6CS00776G

Ji, L., Gu, M., Shao, Y., Li, X., Engelhard, M. H., Arey, B. W., Wang, W., Nie, Z., Xiao, J., Wang, C., Zhang, J.-G., & Liu, J. (2014). Controlling SEI Formation on SnSb-Porous Carbon Nanofibers for Improved Na Ion Storage. *Advanced Materials*, *26*(18). https://doi.org/10.1002/adma.201304962

Jin, Y., Shi, Z., Han, T., Yang, H., Asfaw, H. D., Gond, R., Younesi, R., Jönsson, P. G., & Yang, W. (2023). From Waste Biomass to Hard Carbon Anodes: Predicting the Relationship between Biomass Processing Parameters and Performance of Hard Carbons in Sodium-Ion Batteries. *Processes*, *11*(3), 764. https://doi.org/10.3390/pr11030764

Karthikprabhu, S., Karuppasamy, K., Vikraman, D., Prasanna, K., Maiyalagan, T., Nichelson, A., Kathalingam, A., & Kim, H.-S. (2018). Electrochemical performances of LiNi1−xMnxPO4 (x = 0.05–0.2) olivine cathode materials for high voltage rechargeable lithium ion batteries. *Applied Surface Science*, *449*. https://doi.org/10.1016/j.apsusc.2017.12.060

Karuppasamy, K., Kim, H.-S., Kim, D., Vikraman, D., Prasanna, K., Kathalingam, A., Sharma, R., & Rhee, H. W. (2017). An enhanced electrochemical and cycling properties of novel boronic Ionic liquid based ternary gel polymer electrolytes for rechargeable Li/LiCoO2 cells. *Scientific Reports*, *7*(1). https://doi.org/10.1038/s41598-017-11614-1

Karuppasamy, K., Reddy, P. A., Srinivas, G., Sharma, R., Tewari, A., Kumar, G. H., & Gupta, D. (2017). An efficient way to achieve high ionic conductivity and electrochemical stability of safer nonaflate anion-based ionic liquid gel polymer electrolytes (ILGPEs) for rechargeable lithium ion batteries. *Journal of Solid State Electrochemistry*, *21*(4). https://doi.org/10.1007/s10008-016-3466-2

Karuppasamy, K., Reddy, P. A., Srinivas, G., Tewari, A., Sharma, R., Shajan, X. S., & Gupta, D. (2016). Electrochemical and cycling performances of novel nonafluorobutanesulfonate (nonaflate) ionic liquid based ternary gel polymer electrolyte membranes for rechargeable lithium ion batteries. *Journal of Membrane Science*, *514*. https://doi.org/10.1016/j.memsci.2016.05.010

Kim, H., Hong, J., Park, K. Y., Kim, H., Kim, S. W., & Kang, K. (2014). Aqueous rechargeable Li and Na ion batteries. *Chemical Reviews*, *114*(23), 11788–11827. https://doi.org/10.1021/cr500232y

Kim, J. G., Son, B., Mukherjee, S., Schuppert, N., Bates, A., Kwon, O., Choi, M. J., Chung, H. Y., & Park, S. (2015). A review of lithium and non-lithium based solid state batteries. *Journal of Power Sources*, *282*. https://doi.org/10.1016/j.jpowsour.2015.02.054

Komaba, S., Murata, W., Ishikawa, T., Yabuuchi, N., Ozeki, T., Nakayama, T., Ogata, A., Gotoh, K., & Fujiwara, K. (2011). Electrochemical Na Insertion and Solid Electrolyte Interphase for Hard-Carbon Electrodes and Application to Na-Ion Batteries. *Advanced Functional Materials*, *21*(20). https://doi.org/10.1002/adfm.201100854

Kundu, D., Talaie, E., Duffort, V., & Nazar, L. F. (2015). The Emerging Chemistry of Sodium Ion Batteries for Electrochemical Energy Storage. *Angewandte Chemie International Edition*, *54*(11). https://doi.org/10.1002/anie.201410376

Lee, M., Hong, J., Lopez, J., Sun, Y., Feng, D., Lim, K., Chueh, W. C., Toney, M. F., Cui, Y., & Bao, Z. (2017). High-performance sodium–organic battery by realizing four-sodium storage in disodium rhodizonate. *Nature Energy*, *2*(11). https://doi.org/10.1038/s41560-017-0014-y

Leong, C. C., Pan, H., & Ho, S. K. (2016). Two-dimensional transition-metal oxide monolayers as cathode materials for Li and Na ion batteries. *Physical Chemistry Chemical Physics*, *18*(10). https://doi.org/10.1039/C5CP07357J

Li, W., Zhang, F., Xiang, X., & Zhang, X. (2017). High-Efficiency Na-Storage Performance of a Nickel-Based Ferricyanide Cathode in High-Concentration Electrolytes for Aqueous Sodium-Ion Batteries. *ChemElectroChem*, *4*(11). https://doi.org/10.1002/celc.201700776

Li, Y., Paranthaman, M. P., Akato, K., Naskar, A. K., Levine, A. M., Lee, R. J., Kim, S.-O., Zhang, J., Dai, S., & Manthiram, A. (2016). Tire-derived carbon composite anodes for sodium-ion batteries. *Journal of Power Sources*, *316*. https://doi.org/10.1016/j.jpowsour.2016.03.071

Li, Y., Xu, S., Wu, X., Yu, J., Wang, Y., Hu, Y.-S., Li, H., Chen, L., & Huang, X. (2015). Amorphous monodispersed hard carbon micro-spherules derived from biomass as a high performance negative electrode material for sodium-ion batteries. *Journal of Materials Chemistry A*, *3*(1). https://doi.org/10.1039/C4TA05451B

Li, Z., Bommier, C., Chong, Z. Sen, Jian, Z., Surta, T. W., Wang, X., Xing, Z., Neuefeind, J. C., Stickle, W. F., Dolgos, M., Greaney, P. A., & Ji, X. (2017). Mechanism of Na-Ion Storage in Hard Carbon Anodes Revealed by Heteroatom Doping. *Advanced Energy Materials*, *7*(18), 1–10. https://doi.org/10.1002/aenm.201602894

Lin, Z., Xia, Q., Wang, W., Li, W., & Chou, S. (2019). Recent research progresses in ether- and ester-based electrolytes for sodium-ion batteries. *InfoMat*, *1*(3). https://doi.org/10.1002/inf2.12023

Liu, Y., Xue, J. S., Zheng, T., & Dahn, J. R. (1996). Mechanism of lithium insertion in hard carbons prepared by pyrolysis of epoxy resins. *Carbon*, *34*(2). https://doi.org/10.1016/0008-6223(96)00177-7

Luo, C., Huang, R., Kevorkyants, R., Pavanello, M., He, H., & Wang, C. (2014). Self-Assembled Organic Nanowires for High Power Density Lithium Ion Batteries. *Nano Letters*, *14*(3). https://doi.org/10.1021/nl500026j

Luo, W., Allen, M., Raju, V., & Ji, X. (2014). An Organic Pigment as a High-Performance Cathode for Sodium-Ion Batteries. *Advanced Energy Materials*, *4*(15). https://doi.org/10.1002/aenm.201400554

Luo, W., Bommier, C., Jian, Z., Li, X., Carter, R., Vail, S., Lu, Y., Lee, J. J., & Ji, X. (2015a). Low-surface-area hard carbon anode for Na-ion batteries via graphene oxide as a dehydration agent. *ACS Applied Materials and Interfaces*, *7*(4), 2626–2631. https://doi.org/10.1021/am507679x

Luo, W., Bommier, C., Jian, Z., Li, X., Carter, R., Vail, S., Lu, Y., Lee, J. J., & Ji, X. (2015b). Low-surface-area hard carbon anode for Na-ion batteries via graphene oxide as a dehydration agent. *ACS Applied Materials and Interfaces*, *7*(4), 2626–2631. https://doi.org/10.1021/am507679x

Luo, W., Bommier, C., Jian, Z., Li, X., Carter, R., Vail, S., Lu, Y., Lee, J.-J., & Ji, X. (2015c). Low-Surface-Area Hard Carbon Anode for Na-Ion Batteries via Graphene Oxide as a Dehydration Agent. *ACS Applied Materials & Interfaces*, *7*(4). https://doi.org/10.1021/am507679x

Lux, S. F., Schappacher, F., Balducci, A., Passerini, S., & Winter, M. (2010). Low Cost, Environmentally Benign Binders for Lithium-Ion Batteries. *Journal of The Electrochemical Society*, *157*(3). https://doi.org/10.1149/1.3291976

Markevich, E., Salitra, G., & Aurbach, D. (2017). Fluoroethylene Carbonate as an Important Component for the Formation of an Effective Solid Electrolyte Interphase on Anodes and Cathodes for Advanced Li-Ion Batteries. *ACS Energy Letters*, *2*(6). https://doi.org/10.1021/acsenergylett.7b00163

Martinez de la Hoz, J. M., Soto, F. A., & Balbuena, P. B. (2015). Effect of the Electrolyte Composition on SEI Reactions at Si Anodes of Li-Ion Batteries. *The Journal of Physical Chemistry C*, *119*(13). https://doi.org/10.1021/acs.jpcc.5b01228

Matts, I. L., Dacek, S., Pietrzak, T. K., Malik, R., & Ceder, G. (2015). Explaining Performance-Limiting Mechanisms in Fluorophosphate Na-Ion Battery Cathodes through Inactive Transition-Metal Mixing and First-Principles Mobility Calculations. *Chemistry of Materials*, *27*(17). https://doi.org/10.1021/acs.chemmater.5b02299

Metrot, A., Guerard, D., Billaud, D., & Herold, A. (1980). New results about the sodium-graphite system. *Synthetic Metals*, *1*(4). https://doi.org/10.1016/0379-6779(80)90071-5

Ming, J., Ming, H., Yang, W., Kwak, W.-J., Park, J.-B., Zheng, J., & Sun, Y.-K. (2015). A sustainable iron-based sodium ion battery of porous carbon–Fe_3O_4/$Na_2FeP_2O_7$ with high performance. *RSC Advances*, *5*(12). https://doi.org/10.1039/C4RA14733B

Mogensen, R., Brandell, D., & Younesi, R. (2016). Solubility of the Solid Electrolyte Interphase (SEI) in Sodium Ion Batteries. *ACS Energy Letters*, *1*(6). https://doi.org/10.1021/acsenergylett.6b00491

Morita, R., Gotoh, K., Fukunishi, M., Kubota, K., Komaba, S., Nishimura, N., Yumura, T., Deguchi, K., Ohki, S., Shimizu, T., & Ishida, H. (2016). Combination of solid state NMR and DFT calculation to elucidate the state of sodium in hard carbon electrodes. *Journal of Materials Chemistry A*, *4*(34). https://doi.org/10.1039/C6TA04273B

Palomares, V., Serras, P., Villaluenga, I., Hueso, K. B., Carretero-González, J., & Rojo, T. (2012). Na-ion batteries, recent advances and present challenges to become low cost energy storage systems. *Energy & Environmental Science*, *5*(3), 5884–5901. https://doi.org/10.1039/c2ee02781j

Peled, E., & Menkin, S. (2017). Review—SEI: Past, Present and Future. *Journal of The Electrochemical Society*, *164*(7). https://doi.org/10.1149/2.1441707jes

Ponrouch, A., Marchante, E., Courty, M., Tarascon, J. M., & Palac??n, M. R. (2012). In search of an optimized electrolyte for Na-ion batteries. *Energy and Environmental Science*, *5*(9), 8572–8583. https://doi.org/10.1039/c2ee22258b

Qiu, S., Xiao, L., Sushko, M. L., Han, K. S., Shao, Y., Yan, M., Liang, X., Mai, L., Feng, J., Cao, Y., Ai, X., Yang, H., & Liu, J. (2017). Manipulating Adsorption–Insertion Mechanisms in Nanostructured Carbon Materials for High-Efficiency Sodium Ion Storage. *Advanced Energy Materials*, *7*(17). https://doi.org/10.1002/aenm.201700403

Robinson, J. T., Zalalutdinov, M. K., Cress, C. D., Culbertson, J. C., Friedman, A. L., Merrill, A., & Landi, B. J. (2017). Graphene Strained by Defects. *ACS Nano*, *11*(5). https://doi.org/10.1021/acsnano.7b00923

Saravanan, K., Mason, C. W., Rudola, A., Wong, K. H., & Balaya, P. (2013). The First Report on Excellent Cycling Stability and Superior Rate Capability of $Na_3V_2(PO_4)_3$ for Sodium Ion Batteries. *Advanced Energy Materials*, *3*(4). https://doi.org/10.1002/aenm.201200803

Saurel, D., Orayech, B., Xiao, B., Carriazo, D., Li, X., & Rojo, T. (2018). From Charge Storage Mechanism to Performance: A Roadmap toward High Specific Energy Sodium-Ion Batteries through Carbon Anode Optimization. *Advanced Energy Materials*, *8*(17). https://doi.org/10.1002/aenm.201703268

Slater, M. D., Kim, D., Lee, E., & Johnson, C. S. (2013). Sodium-ion batteries. *Advanced Functional Materials*, *23*(8), 947–958. https://doi.org/10.1002/adfm.201200691

Stevens, D. A., & Dahn, J. R. (2000). High Capacity Anode Materials for Rechargeable Sodium-Ion Batteries. *Journal of The Electrochemical Society*, *147*(4). https://doi.org/10.1149/1.1393348

Stevens, D. A., & Dahn, J. R. (2001). The Mechanisms of Lithium and Sodium Insertion in Carbon Materials. *Journal of The Electrochemical Society*, *148*(8). https://doi.org/10.1149/1.1379565

Stratford, J. M., Allan, P. K., Pecher, O., Chater, P. A., & Grey, C. P. (2016). Mechanistic insights into sodium storage in hard carbon anodes using local structure probes. *Chemical Communications*, *52*(84). https://doi.org/10.1039/C6CC06990H

Sun, N., Liu, H., & Xu, B. (2015). Facile synthesis of high performance hard carbon anode materials for sodium ion batteries. *Journal of Materials Chemistry A*, *3*(41). https://doi.org/10.1039/C5TA05118E

Sutherland, B. R. (2019). Charging up Stationary Energy Storage. *Joule*, *3*(1). https://doi.org/10.1016/j.joule.2018.12.022

Tang, J., Dysart, A. D., & Pol, V. G. (2015). Advancement in sodium-ion rechargeable batteries. *Current Opinion in Chemical Engineering*, *9*. https://doi.org/10.1016/j.coche.2015.08.007

Terzyk, A. P., Furmaniak, S., Harris, P. J. F., Gauden, P. A., Włoch, J., Kowalczyk, P., & Rychlicki, G. (2007). How realistic is the pore size distribution calculated from adsorption isotherms if activated carbon is composed of fullerene-like fragments? *Physical Chemistry Chemical Physics*, *9*(44). https://doi.org/10.1039/b710552e

Townsend, S. J., Lenosky, T. J., Muller, D. A., Nichols, C. S., & Elser, V. (1992). Negatively curved graphitic sheet model of amorphous carbon. *Physical Review Letters*, *69*(6). https://doi.org/10.1103/PhysRevLett.69.921

Wahid, M., Gawli, Y., Puthusseri, D., Kumar, A., Shelke, M. V., & Ogale, S. (2017). Nutty Carbon: Morphology Replicating Hard Carbon from Walnut Shell for Na Ion Battery Anode. *ACS Omega*, *2*(7). https://doi.org/10.1021/acsomega.7b00633

Wahid, M., Puthusseri, D., Gawli, Y., Sharma, N., & Ogale, S. (2018). Hard Carbons for Sodium-Ion Battery Anodes: Synthetic Strategies, Material Properties, and Storage Mechanisms. *ChemSusChem*, *11*(3). https://doi.org/10.1002/cssc.201701664

Wang, C., Fang, Y., Xu, Y., Liang, L., Zhou, M., Zhao, H., & Lei, Y. (2016). Manipulation of Disodium Rhodizonate: Factors for Fast-Charge and Fast-Discharge Sodium-Ion Batteries with Long-Term Cyclability. *Advanced Functional Materials*, *26*(11). https://doi.org/10.1002/adfm.201504537

Wang, C., Zhou, Y., Sun, L., Wan, P., Zhang, X., & Qiu, J. (2013). Sustainable synthesis of phosphorus- and nitrogen-co-doped porous carbons with tunable surface properties for supercapacitors. *Journal of Power Sources*, *239*, 81–88. https://doi.org/10.1016/j.jpowsour.2013.03.126

Wang, J., Yamada, Y., Sodeyama, K., Watanabe, E., Takada, K., Tateyama, Y., & Yamada, A. (2018). Fire-extinguishing organic electrolytes for safe batteries. *Nature Energy*, *3*(1). https://doi.org/10.1038/s41560-017-0033-8

Wang, X., Sun, G., Routh, P., Kim, D.-H., Huang, W., & Chen, P. (2014). Heteroatom-doped graphene materials: syntheses, properties and applications. *Chem. Soc. Rev.*, *43*(20). https://doi.org/10.1039/C4CS00141A

Wang, Z., Selbach, S. M., & Grande, T. (2014). Van der Waals density functional study of the energetics of alkali metal intercalation in graphite. *RSC Adv.*, *4*(8). https://doi.org/10.1039/C3RA47187J

Wen, Y., He, K., Zhu, Y., Han, F., Xu, Y., Matsuda, I., Ishii, Y., Cumings, J., & Wang, C. (2014). Expanded graphite as superior anode for sodium-ion batteries. *Nature Communications*, *5*(May), 1–10. https://doi.org/10.1038/ncomms5033

Xia, X., & Dahn, J. R. (2012). Study of the Reactivity of Na/Hard Carbon with Different Solvents and Electrolytes. *Journal of The Electrochemical Society*, *159*(5). https://doi.org/10.1149/2.jes111637

Xiao, B., Rojo, T., & Li, X. (2019). Hard Carbon as Sodium-Ion Battery Anodes: Progress and Challenges. *ChemSusChem*, *12*(1). https://doi.org/10.1002/cssc.201801879

Xing, W., Xue, J. S., & Dahn, J. R. (1996a). Optimizing pyrolysis of sugar carbons for use as anode materials in lithium-ion batteries. *Journal of the Electrochemical Society*, *143*(10), 3046–3052. https://doi.org/10.1149/1.1837162

Xing, W., Xue, J. S., & Dahn, J. R. (1996b). Optimizing Pyrolysis of Sugar Carbons for Use as Anode Materials in Lithium-Ion Batteries. *Journal of The Electrochemical Society*, *143*(10). https://doi.org/10.1149/1.1837162

Xiong, D., Li, X., Bai, Z., Shan, H., Fan, L., Wu, C., Li, D., & Lu, S. (2017). Superior Cathode Performance of Nitrogen-Doped Graphene Frameworks for Lithium Ion Batteries. *ACS Applied Materials & Interfaces*, *9*(12). https://doi.org/10.1021/acsami.6b15872

Xu, D., Chen, C., Xie, J., Zhang, B., Miao, L., Cai, J., Huang, Y., & Zhang, L. (2016). A Hierarchical N/S-Codoped Carbon Anode Fabricated Facilely from Cellulose/Polyaniline Microspheres for High-Performance Sodium-Ion Batteries. *Advanced Energy Materials*, *6*(6). https://doi.org/10.1002/aenm.201501929

Xu, Z.-L., Yoon, G., Park, K.-Y., Park, H., Tamwattana, O., Joo Kim, S., Seong, W. M., & Kang, K. (2019). Tailoring sodium intercalation in graphite for high energy and power sodium ion batteries. *Nature Communications*, *10*(1). https://doi.org/10.1038/s41467-019-10551-z

Yabuuchi, N., Kubota, K., Dahbi, M., & Komaba, S. (2014a). Research Development on Sodium-Ion Batteries. *Chemical Reviews*, *114*(23). https://doi.org/10.1021/cr500192f

Yabuuchi, N., Kubota, K., Dahbi, M., & Komaba, S. (2014b). Research Development on Sodium-Ion Batteries. *Chemical Reviews*, *114*(23). https://doi.org/10.1021/cr500192f

Yang, J., Zhou, X., Wu, D., Zhao, X., & Zhou, Z. (2017). S-Doped N-Rich Carbon Nanosheets with Expanded Interlayer Distance as Anode Materials for Sodium-Ion Batteries. *Advanced Materials*, *29*(6). https://doi.org/10.1002/adma.201604108

Zhang, W., Dahbi, M., & Komaba, S. (2016). Polymer binder: a key component in negative electrodes for high-energy Na-ion batteries. *Current Opinion in Chemical Engineering*, *13*. https://doi.org/10.1016/j.coche.2016.08.001

Zhao, C., Liu, L., Qi, X., Lu, Y., Wu, F., Zhao, J., Yu, Y., Hu, Y.-S., & Chen, L. (2018). Solid-State Sodium Batteries. *Advanced Energy Materials*, *8*(17). https://doi.org/10.1002/aenm.201703012

Zhao, F., Xue, P., Ge, H., Li, L., & Wang, B. (2016). Na-Doped Li $_4$ Ti $_5$ O $_{12}$ as an Anode Material for Sodium-Ion Battery with Superior Rate and Cycling Performance. *Journal of The Electrochemical Society*, *163*(5). https://doi.org/10.1149/2.0781605jes

Zheng, T., Xue, J. S., & Dahn, J. R. (1996). Lithium insertion in hydrogen-containing carbonaceous materials. *Chemistry of Materials*, *8*(2), 389–393. https://doi.org/10.1021/cm950304y

Zhu, Y., Murali, S., Cai, W., Li, X., Suk, J. W., Potts, J. R., & Ruoff, R. S. (2010). Graphene and Graphene Oxide: Synthesis, Properties, and Applications. *Advanced Materials*, *22*(35). https://doi.org/10.1002/adma.201001068